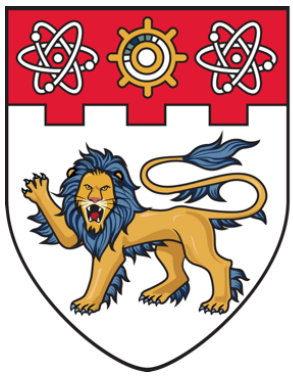

NANYANG TECHNOLOGICAL UNIVERSITY
SINGAPORE

ELECTRODE MODIFICATION AND IN-SITU STUDIES TO ENHANCE THE PERFORMANCE OF VANADIUM REDOX FLOW BATTERIES

PURNA CHANDRA GHIMIRE

INTERDISCIPLINARY GRADUATE SCHOOL
ENERGY RESEARCH INSTITUTE @ NTU (ERI@N)

2019

ELECTRODE MODIFICATION AND IN-SITU STUDIES TO ENHANCE THE PERFORMANCE OF VANADIUM REDOX FLOW BATTERIES

PURNA CHANDRA GHIMIRE

Interdisciplinary Graduate School

Energy Research Institute @ NTU (ERI@N)

A thesis submitted to the Nanyang Technological University in partial fulfilment of the requirement for the degree of

Doctor of Philosophy

2019

Statement of Originality

I hereby certify that the work embodied in this thesis is the result of original research, is free of plagiarised materials, and has not been submitted for a higher degree to any other University or Institution.

[02/08/2019]   [   ]

. . . .

Date   [Purna Chandra Ghimire]

Supervisor Declaration Statement

I have reviewed the content and presentation style of this thesis and declare it is free of plagiarism and of sufficient grammatical clarity to be examined. To the best of my knowledge, the research and writing are those of the candidate except as acknowledged in the Author Attribution Statement. I confirm that the investigations were conducted in accord with the ethics policies and integrity standards of Nanyang Technological University and that the research data are presented honestly and without prejudice.

[02/08/2019] [Qingyu Yan.]

. . . . . .
Date

. . . . . .
[Professor Alex Yan Qingyu]

Authorship Attribution Statement

This thesis contains material from three papers published in the following peer-reviewed journals where I was the first author.

Part of Chapter 4 is published as Purna C. Ghimire, Rüdiger Schweiss, Günther G. Scherer, Nyunt Wai, Tuti M. Lim, Arjun Bhattarai, Tam D. Nguyen, and Qingyu Yan "Titanium carbide-decorated graphite felt as high performance negative electrode in vanadium redox flow batteries" *Journal of Materials Chemistry A* 6, no. 15, 6625-6632 (2018). DOI: 10.1039/C8TA00464A.

The contributions of the co-authors are as follows:

- Prof Qingyu Yan suggested the material and edited the manuscript drafts.
- I prepared the manuscript drafts. The manuscript was revised by Prof. Günther G. Scherer and Dr Rüdiger Schweiss.
- I co-designed the study with Mr Nyunt Wai and Dr Arjun Bhattarai.
- I performed all the laboratory work and analyzed the data.
- Dr Tuti M. Lim assisted in analyzing the XPS data.
- Dr Tam D. Nguyen assisted in analyzing the STEM and XRD data.

Part of Chapter 5 is published as Purna C. Ghimire, Arjun Bhattarai, Rüdiger Schweiss, Günther G. Scherer, Nyunt Wai, and Qingyu Yan "A comprehensive study of electrode compression effects in all vanadium redox flow batteries including locally resolved measurements", Applied energy 230, 974-982, (2018).

The contributions of the co-authors are as follows:

- Prof Qingyu Yan provided the initial direction and edited the manuscript drafts.
- I wrote the drafts of the manuscript. The manuscript was revised together with Prof Günther G. Scherer and Dr. Rüdiger Schweiss.
- Dr Bhattarai and I co-designed the study and prepared the experimental setup.

- Mr. Nyunt Wai analyzed the initial experiment and provided the direction for the further experiment.
- I performed all the laboratory work and analyzed the data.

Part of Chapter 5 is published as Purna C. Ghimire, Arjun Bhattarai, Rüdiger Schweiss, Günther Scherer, Nyunt Wai, Tuti Lim, and Qingyu Yan. "Investigation of Reactant Conversion in the Vanadium Redox Flow Battery Using Spatially Resolved State of Charge Mapping." Batteries 5, no. 1, 2, (2019)

The contributions of the co-authors are as follows:

- Prof Qingyu Yan provided the initial direction and edited the manuscript drafts.
- I wrote the drafts of the manuscript. The manuscript was revised together with Prof Günther G. Scherer and Dr. Rüdiger Schweiss.
- Dr Bhattarai and I co-designed the study and prepared the experimental setup.
- Dr Tuti M. Lim and Mr. Nyunt Wai analyzed the initial experiment and provided the direction for the experiment.
- I performed all the laboratory work and analyzed the data.

[02/08/2019] [ ]

. . . .

Date [Purna Chandra Ghimire]

List of Publications

1. **P.C. Ghimire**, R. Schweiss, G.G. Scherer, N. Wai, T.M. Lim, A. Bhattarai, T.D. Nguyen, Q. Yan, Titanium carbide-decorated graphite felt as high-performance negative electrode in vanadium redox flow batteries, ***Journal of Materials Chemistry A***, 6, 2018, 6625-6632.

2. **P. C. Ghimire**, A. Bhattarai, R. Schweiss, G.G. Scherer, N. Wai, Q. Yan, A comprehensive study of electrode compression effects in all vanadium redox flow batteries including locally resolved measurements, ***Applied Energy***, 230, 2018, 974-982.

3. **P.C. Ghimire**, A. Bhattarai, R. Schweiss, G.G. Scherer, N. Wai, T.M. Lim, Q. Yan, Investigation of Reactant Conversion in the Vanadium Redox Flow Battery Using Spatially Resolved State of Charge Mapping, ***Batteries***, 5, 2019, 2.

4. **P.C. Ghimire**, A. Bhattarai, R. Schweiss, G.G. Scherer, N. Wai, T.M. Lim, Q. Yan, A comprehensive study of the thermal oxidation of PAN-based carbon felts and its optimization for the negative half-cell of the all-vanadium redox flow battery, *Carbon* [under review]

5. A. Bhattarai, A. Whitehead, R. Schweiss, G. G. Scherer, M. Skyllas-Kazacos, N. Wai, T.D. Nguyen, **P. C. Ghimire**, M O. Oo, and H. H. Hng. "Anomalous Behavior of Anion Exchange Membrane during Operation of a Vanadium Redox Flow Battery." ***ACS Applied Energy Materials,*** 2, 2019, 1712-1719.

6. A. Bhattarai, N. Wai, R. Schweiss, A. Whitehead, G.G. Scherer, **P.C. Ghimire**, T.M. Lim, H.H. Hng, Vanadium redox flow battery with slotted porous electrodes and automatic rebalancing demonstrated on a 1 kW system level, ***Applied Energy***, 236, 2019, 437-443.

7. A. Bhattarai, **P. C. Ghimire**, A. Whitehead, R. Schweiss, G. G. Scherer, N. Wai, H. H. Hng, Novel approaches for solving the capacity fade problem during operation of a vanadium redox flow battery, ***Batteries***, 4, 2018, 48.

8. A. Bhattarai, N. Wai, R. Schweiss, A. Whitehead, G.G. Scherer, **P.C. Ghimire**, T.D. Nguyen, H.H. Hng, Study of flow behavior in all-vanadium redox flow battery using spatially resolved voltage distribution, ***Journal of Power Sources***, 360, 2017, 443-452

9. T. D. Nguyen, A. Whitehead, G. G. Scherer, N. Wai, M. O. Oo, A. Bhattarai, **P. C. Ghimire**, Z. J. Xu (2016) The oxidation of organic additives in the positive electrolyte and its effect on the performance of vanadium redox flow battery, ***Journal of Power Sources***, 334, 2016, 94-103.

Abstract

The demand for renewable energy has increased in the recent decades due to the environmental benefits and their better availability. However, electricity generated from renewable energy sources is inherently intermittent and hence fluctuating. Suitable energy storage systems are required to stabilize the intermittency and to fill the deficit between demand and supply. Redox flow batteries (RFB) hold the capacity to meet these demands, as it offers unlimited capacity. Among different redox flow batteries, the vanadium redox flow battery (VRFB) is considered as one of the promising technologies for large-scale energy storage. The benefits of the VRFB are associated with its flexible power rating and storage time, low-maintenance cost, excellent load levelling capacity and long lifetime. The unique feature of the VRFB is the separation of the battery stack and electrolyte, which allows the decoupling of power output and energy capacity. Unlike other redox couples, due to the use of same redox species, undesirable performance fading and ion crossover can be mitigated during operation in VRFB. Simple remixing of the electrolytes in two half-cell periodically can reverse the capacity fade.

Despite the ongoing commercial deployment of VRFB, there are research needs with respect to the improvement of battery performance and reducing the cost of VRFB. The research work in VRFB are mainly on membrane, electrode, electrolyte and the design of the stack, as role of these components determines the overall performance. The electrode is one of the major components of VRFB, which largely determines the efficiency and durability of the battery. In particular, as key component, electrode provides the site for redox reaction in each half-cell, which determines the cell performance. PAN-based graphite felts are widely used as electrodes in VRFB, however, pristine graphite felts from the manufacturer are inherently hydrophobic and have poor electrocatalytic properties towards vanadium species. Therefore, various modification methods are proposed to activate the surface of the graphite felt. Among these, thermal oxidation in the air is the most widely used technique owing to its simplicity and cost-effectiveness. Despite being widely used, there is a lack of scientific investigation on electrode treatment at various temperature and duration range. Most importantly, the correlation between the change in electrode physicochemical and electrochemical properties need to be investigated for

achieving the optimum modification conditions. The alternative electrode modification method, which prevents the performance loss due to degradation of the electrode, also needs to be investigated. There are also no suitable methods to precisely estimate the electrolyte utilization across the porous media after the modification of the electrode by various techniques. Thus, this PhD research aimed to investigate the correlation between the physiochemical and electrochemical properties of PAN-based graphite felt electrodes. The study will use such correlation to prepare the optimized electrode with best VRFB performance and demonstrate in a single VRFB cell.

With respect to the battery performance, catalyst decoration and surface modification were explored to fulfil the major objective of this study. A novel synthesis method has been carried out to dope binder-free titanium carbide (TiC) particles onto the surface of carbon fibres using titanium tetrafluoride (TiF_4) as the titanium source. The method of preparation was inexpensive and yielded uniformly distributed TiC particles on the carbon fibre surface, which enhance the charge transfer kinetics of the sluggish negative redox couple (V^{2+}/ V^{3+}). Additionally, a systematic investigation of the effect on thermal oxidation of PAN-based graphite felts on its performance at the negative electrode of the VRFB was performed. The results from ex-situ characterization techniques were employed to identify crucial material properties, such as surface composition, specific surface area, defects and electrochemical parameters including wetting properties, mass loss, surface morphology etc. and relate with the cell performance of the cell at the specific condition.

Locally resolved segmented cell study was performed to investigate the in-situ behaviour of a flow cell. A single cell with an electrode area of 100 cm^2 was divided into sixteen segments to investigate the local voltage and open circuit voltage (OCV). The spatially resolved OCV was then converted to the corresponding state of charge (SOC) of the electrolyte, which was used to predict the flow behaviour and electrolyte utilization across the electrode. For the first time, a rationale to estimate the degree of electrolyte utilization is proposed based on the differences between experimental and theoretical changes in SOC. The concept was then verified with the experiment from the optimized electrode compression study of the single non-segmented cell. In addition, the study also concluded that 25% of electrode compression with respect to its initial thickness gave optimum

conversion efficiency. The investigation was further extended to study the electrolyte utilization at various operating conditions, such as differently modified electrodes, various flow rates, various current densities etc. Furthermore, overpotential at each half-cell at various operating conditions was studied using the half-cell potential measurement method by inserting reference electrodes at the outlet tube of the VRFB single cell.

In summary, this PhD study has successfully demonstrated the use of a low-cost novel catalyst to enhance the negative half-cell of VRFB. The study has also successfully investigated the correlation between the physiochemical and electrochemical properties of PAN-based graphite felt electrode by studying the effect of thermal oxidation on the electrode physical and electrochemical properties under various treatment temperatures and durations. By doing so, it can gain an in-depth understanding with respect to treatment temperature and duration on VRFB performance. The research has also successfully carried out first ever in-situ study based on OCV mapping to estimate the degree of electrolyte utilization.

Acknowledgements

It gives me great pleasure to appreciate and acknowledge all the people who have been an integral part of my PhD journey. I would like to express my deepest gratitude to Professor Alex Yan Qingyu for his precious supervision and support throughout my PhD journey. Thank you very much for the encouragement to do better in each stage of my research. I express my appreciation to the co-supervisor Dr Tuti Mariana Lim for the valuable support and preparation of the final draft.

My special acknowledgement to our project PI and mentor, Mr. Nyunt Wai from Energy Research Institute @ NTU for his support for creating a good working environment and organizing regular progress meeting. Thanks a lot for actively helping in research and laboratory works.

My special acknowledgement to Dr. Rüdiger Schweiss and Professor Günther G. Scherer for the continuous guidance throughout my PhD journey. Thank you Prof. Günther and Dr. Rüdiger for all the valuable feedback for the manuscript and final draft. Many thanks to Dr. Rüdiger for instant response of my queries and delivering the electrode material. I am also thankful to Dr. Adam Whitehead for providing the support during my PhD journey.

I would like to thank Ms. Moe Ohnar Oo for the support to create the friendly environment in laboratory, supporting in research matter and managing the inventory. Special thanks to my friend and research colleague Dr. Arjun Bhattarai for his assist and feedback. Likewise, I would like to thank my research colleagues Mr. Nguyen Duy Tam and Ms. Sukriti Gupta for creating the good working environment. I would like to thank Anil and Milan for technical suggestion for the thesis preparation.

I would like to acknowledge SGL Carbon and NTU for their support on finance and facilities of my PhD project. I am grateful to Energy research institute@NTU for providing the lab space for redox flow research.

This journey would have never been possible without the wishes and support of my parents who always provided encouragement, love and support in my life.

Table of Contents

Table Captions

Figure Captions

Figure 5.3 (a) OCV vs time curve after terminating the discharge at 80 mA cm^{-2} and (b) the corresponding contour diagram at 5 s in OCV after termination. The flow rate was 42 mL min-1

Figure 5.4 SOC with corresponding OCV on the legend contours. All the contours were measured 5s after the termination of discharge at 150 mA cm^{-2}

Figure 5.5 Comparision of: (a) coulombic efficiency, (b) energy efficiency, (c) voltage efficiency and (d) discharge capacity for different electrode compression levels.

Figure 5.6 (a) Energy efficiency and (b) discharge energy during 50 cycles at 40 mA cm^{-2}

Figure 5.7 Internal resistance for various compressed electrodes (a) at different current densities and (b) at 40 mA cm^{-2} for 50 cycles

Figure 5.8 Pressure drop in (a) positive half- cell and (b) negative half-cell

Figure 5.9 Pumping power consumption and pressure drop at different electrode compressions

Figure 5.10 Energy efficiency (a: Net EE excluding pump power consumption and b: EE including pump power consumption) of VRFB cells at different current densities and compression levels

Figure 5.11 OCV contours at 5 s after termination of discharge at 80 mA cm^{-2} for (a) pristine, (b) chemically modified and (c) thermally modified electrodes. The flow of electrolyte was 42 mL min^{-1}

Figure 5.12 OCV/SOC contours at 5 s after termination of discharge at 80 mA cm^{-2}. The flow rate of electrolyte was (a) 16 mL min-1, λ= 1.3 (b) 32 mL min^{-1}, λ= 2.6 and (c) 42 mL min-1, λ= 3.4

Abbreviations

RBF	Redox flow batteries
NTU	Nanyang Technological University
VRFB	Vanadium Flow Battery
PAN	Polyacrylonitrile
TiC	Titanium Carbide
OCV	Open Circuit Voltage
SOC	State Of Charge
PEM	Polymer Electrolyte Membrane
CV	Cyclic Voltammetry
EIS	Electrochemical Impedance Spectroscopy
AC	Alternating current
DC	Direct Current
RFB	Redox flow battery
NASA	National Aeronautics and Space Administration
UNSW	University of New South Wales
PVC	Poly Vinyl Chloride
FF	Flow Frame
ASR	Area Specific Resistance
EDTA	Ethylenediaminetetraacetic acid
CEM	Cation Exchange Membrane
AEM	Anion Exchange Membrane
PEEK	Polyether ether ketone
XPS	X-ray photoelectron spectroscopy
NHE	Normal hydrogen electrode
ECSA	Electrochemically active surface area
PCB	Printed Circuit Board
CC	Current Collector
DHE	Dynamic hydrogen electrode
FESEM	Field emission scanning electron microscopy

HRTEM	High-resolution transmission electron microscopy
XRD	X-ray diffraction
BET	Brunauer, Emmett and Teller
TGA	Thermogravimetric analysis
SMSE	Standard mercury sulphate electrode
DLC	Double layer capacitance
SEM	Scanning electron microscopy
HER	Hydrogen evolution reaction
BP	Bipolar plate
FWHM	Full width half maximum
EE	Energy Efficiency
CE	Coulombic Efficiency
VE	Voltage Efficiency
PP	Polypropylene
kWh	Kilo Watt Hour
ΔP	Pressure Dr

Chapter 1

Introduction

This chapter summarises the scientific and technical issues related to the vanadium redox flow battery (VRFB), and the relevance for conducting this project. Enhancing cell performance by optimizing the electrode modification in each half-cell, electrode long-term stability and real-time data acquisition to optimize the various parameters during the operation of a cell are among the major research and development areas of VRFB. The chapter progresses to discuss the aforementioned limitations, and thus, introduces the objectives and approaches to address the limitations. An overview of each chapter is discussed, which is followed by the main findings and outcomes of the study.

1.1 Problem Statement

Renewable energy sources have gained much attention in recent decades due to their low environmental impact. However, renewable energy sources are inherently intermittent and fluctuating [1]. These issues can be resolved only with appropriate energy storage systems. Among the various energy storage technologies, vanadium redox flow battery (VRFB) is one of the promising candidates due to its independent power and capacity rating, safety and design flexibility [2-4]. A VRFB system consists of two-reaction compartments separated by an ion exchange membrane. The single vanadium sulfate solution with four different valance states of vanadium as electrolyte is utilized in the system, thus avoiding the cross-contamination of the electrolytes [3-5].

The energy efficiency of VRFB significantly depends on the electrodes, as the redox reaction of vanadium ions occurs on the surface of the electrode. Thus, to develop a high-performance VRFB, electrochemical activity of the electrode needs to be enhanced. Carbonaceous materials have been extensively used as the electrode due to their high surface area. In particular, graphite felt provides ample of redox reaction sites due to their high surface area, good stability and good electronic conductivity. However, sluggish electrochemical reactions and poor wettability in electrolyte results in low VRFB performance. As a result, modification/activation must be performed to improve the electrode performance.

Thermal oxidation of the electrodes is by far the most widely used technique for the activation of the electrodes. It leads to performance improvement by altering the various properties of the graphite felt. The thermal pretreatment strategies are widely adopted in practice. However, the exact understanding on the role of different parameters under varying temperature and duration remains unclear. Most of the studies attribute the increase in performance to increase in surface functional groups [6-8] or increase in graphitic edge sites [7-9] or increase in wettability [9] and specific surface area. In addition, there are two separate reactions with different mechanisms in each half-cell. These have not been fully yet clarified. Several possible mechanisms have been proposed in the literature, which will be explained in detail in chapter 2. Thus, finding an optimized thermal oxidation

temperature with investigating the change in electrode properties due to thermal oxidation with varying temperature and duration is applicable in both lab and commercial scale. Similarly, the surface modification of the electrode by the acid such as H_2SO_4, HNO_3, mixture of both and H_3PO_4 has been widely studied. The effect of the wet modification led to dramatic improvement in the cell performance. The electrochemical activity of the graphite felt increased significantly. However, the increase of performance depends on the time of exposure and the type of the used. The possible reaction mechanism due to the wet chemical method will be explained in chapter 2.5.5.

Beside thermal and chemical modification, an alternative method for enhancing cell performance by improving the charge transfer kinetics is to deposit a catalyst on the surface of the electrode. This approach is suitable only if catalyst decorated electrode fulfils certain criteria, such as non-susceptibility toward hydrogen evolution in the negative half-cell, stability of the catalyst in the highly acidic environment and the uniform distribution of the catalyst throughout the electrode volume. Furthermore, the method used for the deposition of the catalyst plays an essential role, since the catalysts need to bind effectively to the surface of the carbon fibre to warrant electronic contact. The catalyst should show sufficient stability against dissolution or electrochemically induced ageing. Finally, the cost and availability of the catalyst are the basic requirements for practical application. The noble metals, such has gold, palladium, platinum and iridium have been incorporated in the electrode to enhance the performance. The high cost of noble metal limits their use in practical application in VRFB. Non- metals usually do not perform well in acidic ambience. Therefore, transition metal carbides or nitrides could be of great importance due to their stability, electronic conductivity, comparable catalytic activity with metal, as well as ease of synthesis and cost.

Usually, for the performance evaluation of VRFB, ex-situ characterization is usually carried out to evaluate the overall cell performance. This black box approach, however, is unable to provide in-depth understanding of the local changes within the cell. By contrast, localized real-time measurements using segmented cells might shed more light on the different mechanisms limiting the cell performance as the resistance, current and voltage can be monitored independently in each segment. This approach has been extensively used

in PEM fuel cells [10-13] to measure the current distribution. Segmented cell studies of flow battery are scarce. The locally resolved study conducted via segmented cell could be of great importance to predict the optimized flow distribution, flow rate, electrode compression, electrode activation method, flow configuration etc. An approach of segmentation is introduced for local voltage mapping. The use of OCV contours instead of voltage contours under current flow allowed for a precise prediction of the flow streamlines through the porous electrode. A new strategy for mapping and quantification of the conversion efficiency (or reactant utilization) in redox flow batteries using segmented cells is presented. The systematic introduction of the whole experimental setup and working scheme is introduced in chapter 3.6 and 5, respectively.

The kinetics of the two half-cell reactions in VRFB is dissimilar. Popular techniques such as cyclic voltammetry (CV), electrochemical impedance spectroscopy (EIS), rotating disc electrode voltammetry etc. have been used for the ex-situ analysis of the reaction kinetics. EIS can be employed to characterize the cell in-situ condition; however, they are not well established in flow batteries yet due to complex kinetics, use of thick porous electrode and existence of multiple ions and complexes. Polarization measurement has been used to quickly screen the performance of flow cell in-situ, however, these methods are rather qualitative and provide limited information. Segmented cell studies constitute an elegant method to study the interplay between electrochemistry and mass transport. This method is very useful but needs a complex cell design and handling of a large number of data points. The insertion of a reference electrode in a cell provides the kinetics of negative and positive half separately. The same technique can be implemented to study the kinetics of different types of electrodes at various operating conditions.

1.2 Objectives and Scope

The general objective of this PhD research is to investigate the electrode material properties and its modification to improve the performance of VRFB, to develop and implement a diagnostic tool to realize the importance of locally resolved study for prediction of the electrolyte utilization and optimized flow distribution.

Specific objectives:

- Investigating the correlation between physicochemical and electrochemical properties of carbon felts and their influences on VRFB.
- Optimization of thermal oxidation duration and temperature for the activation of the electrodes
- Deposition of the catalyst onto the carbon fibre to enhance the overall cell performance by enhancing the electron transfer rate.
- Investigating the electrode properties and its reproducibility.
- Developing the diagnostic technique for the study of the local behaviour to acquire a better understanding of electrolyte utilization across the electrode.
- Implementing the developed diagnostic tool to study cell performance by varying various operational parameters.
- Developing the technique to determine the overpotential at different operating conditions in each half-cell.

To test for reproducibility of the electrodes produced at the different batches, three different electrodes produced in different batches were selected. The physical, electrochemical, spectroscopic characterization along with cell cycling was examined. The results from these characterizations were analyzed to understand the variations on the electrode produced at different batches. The study was also conducted to acquire the variation in electrochemical properties at each half-cell.

Depending on the outcome of the half-cell studies, the necessary modification/activation of the electrode was performed. The chosen activation methods are simple, economical and applicable in both lab and commercial scale. For activation of electrodes, thermal oxidation in the air was chosen as one of the methods, due to its simplicity and effectiveness. The thermal oxidation of electrodes was performed in a systematic way by selecting the different temperatures and time duration. It provided the correlation between the treatment conditions, and the physical and electrochemical properties together with cell performance.

The other method to enhance the performance of the VRFB is to deposit catalyst onto the surface of the electrode. The catalyst should be abundant, cheap and the process of deposition should be simple. The catalyst should inhibit or at least should not promote the

hydrogen production in the negative half of the cell and must be stable at low pH. For the aforementioned reasons, transition metal carbide was taken into consideration.

For the in-situ study, a spatially resolved voltage distribution method with the aid of a segmented cell was performed. A cell with an area of 100 cm^2 was divided into 16 segments. The voltage distribution across the 16 segments was analyzed to predict the exact flow behaviour and electrolyte utilization across the electrode. This technique was later extended to investigate the electrode compression, flow rate, flow configuration etc.

Similarly, an approach to determine the overpotential under various operating conditions was also investigated for each half-cell. For this, reference electrodes were placed at the outlet of the cell and the measurement of the full cell voltage along with half-cell potential was performed concurrently. The idea was applied to acquire information about the overpotential in each half-cell with the use of the different type of electrodes, various flow rates of electrolyte and concentration of electrolytes etc.

1.3 Dissertation Overview

The thesis reports the progress and achievement of VRFB performance through thermal oxidation treatment optimization of electrodes and deposition of novel catalyst on the surface of the electrodes. In addition, it also describes the in-situ performance investigation by using a novel cell segmentation approach. The thesis includes the five chapters:

Chapter 1 provides the rationale for research to contextualize the thesis and outline the objectives, scope and the novelty of the work.

Chapter 2 provides a review of the literature concerning its development and current research interest. The chapter covers the advantage and disadvantage of redox flow battery, R & D progress in VRFB including electrode and electrochemistry of the system. Various approaches for the in-situ study of the VRFB are also described in the chapter.

Chapter 3 discusses the methodology employed to achieve the objective of the work. This includes the sequence of experiments conducted, the selection criteria for thermal oxidation study, the synthesis method of catalyst decorated electrodes, the development of the

segmented cell, and development of the half-cell overpotential measurement cell. The chapter also includes all experimental set-ups, measurement procedures, characterization and analysis carried out during the study.

Chapter 4 provides the results of experiments conducted via various approaches as described in chapter 3. The initial section presents the properties and reproducibility of the electrodes used during the experiment and its electrochemical performance in the negative and positive half cycle. This is then followed by the systematic study of thermal oxidation of the electrode. Finally, the chapter explains about the decoration of electrode with the novel catalyst and its role in performance enhancement of the VRFB.

Chapter 5 presents the result of the two in-situ approaches to study the performance of VRFB. The first approach explains about the segmented method by acquiring the information from the locally resolved voltage to predict the exact behaviour of the cell. For the first time, a hypothesis is presented which is then validated with the results from the segmented cell experiment in VRFB. The second approach presents the overpotential study at various operating parameter at each half of the cell.

Chapter 6 presents the conclusions and recommendation of the study. A summary of the results is presented in this chapter together with the recommendation on opportunity and strategy for future work.

1.4 Findings and Outcomes/Originality

On the course of completing the objectives of the study, several fundamental research, novel ideas and engineering aspects were involved. The findings and novelties obtained in this PhD research are listed below:

- Synthesis of novel catalyst onto the surface of carbon fiber to enhance the performance of a negative half-cell of VRFB.

  Deposition of abundant and inexpensive catalyst onto the surface of the electrodes increases the performance of VRFB. It not only increases the performance but also reduces the chance of performance loss due to degradation of an electrode in negative half-cell [14]. A novel synthesis method for the preparation of titanium carbide

nanoparticles supported on graphite felts for use in VRFB is presented. The method of preparation is inexpensive and yields uniformly distributed TiC particles on the carbon fiber surface, which boost the charge transfer kinetics of the sluggish negative redox couple (V^{2+}/ V^{3+}). The TiC-decorated electrode, when used in the negative half-cell of a VRFB, enabled high electrolyte utilization resulting in increased energy efficiency. It exhibited a 13.3 % increase in energy efficiency at a current density of 100 mA cm^{-2}, compared to the pristine electrode. Moreover, it showed excellent stability with high capacity retention over repetitive cycling.

- A systematic study of thermal oxidation of PAN-based electrodes to optimize the treatment temperature and time.

  In this study, a systematic investigation of thermal oxidation on PAN-based graphite felts at the negative electrode of VRFB has been performed. In most of the previous studies, either the activation method or type of electrodes is investigated. The lack of scientific investigation on electrode treatment at higher, medium and lower temperature at different duration has limited the understanding of the change in electrode properties, such as electrochemical, microscopic, physical, spectroscopic etc. and their contribution to overall improvement in the performance of the electrode. In this study, the temperature and duration of the oxidation step were selected from the three different regions along the thermogravimetric curve. The results from ex-situ and in-situ characterization techniques along with cell cycling test were employed to obtain an optimal treatment temperature and time for graphite felt electrodes. A correlation between the double layer capacitance, which measured the density of highly reactive edge planes or defects, and the cell performance could be verified. Out of various samples examined, the sample treated at 750°C for 5 minutes showed the most favourable effect.

- Development of the segmented cell to study flow behaviour and electrolyte utilization across the electrode

  For the first time, a completely new method of segmentation and the technique to predict the flow behaviour and electrolyte utilization in conventional flow cell is presented. The method of segmentation is easily scalable to any size. Instead of

analyzing charging/discharging current or voltage among the segments, the local mapping of OCV is performed to minimize the effect of the lateral flow of current. The local OCV was converted to the corresponding SOC, and a relationship was established by taking the differences between experimental and theoretical SOC. This relationship is then used to predict how much the electrolyte has been utilized across the electrode under various operating conditions.

- Investigation of electrode compression using both segmented and non-segmented studies

  For optimal performance of cell/stack, electrode compression should be optimized. Excessive compression of the electrode, however, leads to non-uniform flow distribution and potential occurrence of zones with the retarded flow of electrolyte. Too low compression results in very high contact resistance as well as potential leakage of the electrolyte. The previous studies are mainly focused on electronic resistance and efficiency. However, less attention is paid to the effect of compression on the flow distribution and electrolyte utilization. In this study, in addition to conventional figures of merit, such as efficiencies and resistances, the effects of compression on the pressure drop, flow distribution, electrolyte utilization were investigated. From the single cell results, it is clear that the electrode compressed at 25% (with respect to its original thickness) constitute the optimum level, ensuring the low contact resistance, moderate pressure drops, and highest efficiency. The spatially resolved study also shows the uniform flow distribution of electrolyte across the electrode at 25% electrode compression with the highest percentage of the reactant conversion.

- Development of experimental setup with an insertion of the reference electrode in outlet tubing to calculate the overpotential of each half cell

  Half-cell potential measurements by inserting the reference electrode in VRFB allow an independent study of both half-cells. The results from the individual study of half-cells can be used to improve the battery components and optimize the operation. Previous studies attempted at inserting the reference electrodes within the active area, proved to be very complicated and difficult to design. In this study, a detailed investigation of an alternative method of inserting a reference electrode at the outlet

tube to measuring individual half-cell potential is presented. The performance of as-received graphite felt and thermally treated graphite felt were studied in detail at various electrolyte flow rates, concentration and state of charge of the electrolyte. The method is simple and scalable to any size of the cell for the determination of the individual potential of each half-cell.

References

[1] R.M. Darling, K.G. Gallagher, J.A. Kowalski, S. Ha, F.R. Brushett, *Energy & Environmental Science*, **2014**,7, 3459-3477.

[2] P. Leung, X. Li, C.P. De León, L. Berlouis, C.J. Low, F.C. Walsh, , *Rsc Advances*, **2012**, 2, 10125-10156.

[3] M. Skyllas-Kazacos, M. Chakrabarti, S. Hajimolana, F. Mjalli, M. Saleem, *Journal of The Electrochemical Society*, **2011**,158, R55-R79.

[4] W. Wang, Q. Luo, B. Li, X. Wei, L. Li, Z. Yang, *Advanced Functional Materials*, **2013**, 23, 970-986.

[5] L. Li, S. Kim, W. Wang, M. Vijayakumar, Z. Nie, B. Chen, J. Zhang, G. Xia, J. Hu, G. Graff, *Advanced Energy Materials*, **2011**, 1, 394-400.

[6] B. Sun, M. Skyllas-Kazacos, *Electrochimica Acta*, **1992,** 37, 1253-1260.

[7] J. Langner, M. Bruns, D. Dixon, A. Nefedov, C. Wöll, F. Scheiba, H. Ehrenberg, C. Roth, J. Melke, *Journal of Power Sources*, **2016**, 321, 210-218.

[8] D. Kil, H.J. Lee, S. Park, S. Kim, H. Kim, *Journal of The Electrochemical Society*, **2017**, 164, A3011-A3017.

[9] T.J. Rabbow, M. Trampert, P. Pokorny, P. Binder, A.H. Whitehead, *Electrochimica Acta*, **2015**, 173, 17-23.

[10] C. Hartnig, I. Manke, N. Kardjilov, A. Hilger, M. Grünerbel, J. Kaczerowski, J. Banhart, W. Lehnert, *Journal of Power Sources*, **2008**, 174, 452-459.

[11] N. Zamel, R. Hanke-Rauschenbach, S. Kirsch, A. Bhattarai, D. Gerteisen, *International Journal of Hydrogen Energy*, **2013**, 38, 15318-15327.

[12] S. Cleghorn, C. Derouin, M. Wilson, S. Gottesfeld, *Journal of Applied Electrochemistry*, **1998**, 28, 663-672.

[13] I. Schneider, S. Von Dahlen, A. Wokaun, G. Scherer, *Journal of The Electrochemical Society*, **2010**, 157 B338-B341.

[14] I. Derr, A. Fetyan, K. Schutjajew, C. Roth, *Electrochimica Acta*, **2017**, 224, 9-16.

Chapter 2

Literature Review

This chapter provides a detailed review of the literature concerning a vanadium redox flow battery (VRFB). It includes the importance of VRFB storage system, its working principle, advantages and disadvantages, description of components and performance measures. It also describes in detail about the electrochemistry, various losses and electrode kinetics of a system. In addition, it also reviews the research including research gaps particularly in the areas of electrode and electrolyte utilization which are addressed in this PhD thesis. The review on the electrode properties, types of modifications method adopted, and proposed electron transfer mechanisms are discussed thoroughly. This is followed by the introduction on the in-situ study of the VRFB study to predict flow distribution and electrolyte utilization of the VRFB. A detailed review with respect to the segmentation of the cell is performed. Further, the chapter also includes the in-situ measurement of half-cell potential in detail.

2.1 Battery Energy Storage

The use of battery storage technology for electricity storage dates back even before the alternating current (AC) power was demonstrated by Nikola Tesla. From then on, many battery technologies were developed including efficient methods to use combined DC and AC power. With the rising demand in renewable energy, the demand for energy storage will also rise significantly as it is the key to unlock the intermittency in renewable energy. Prominent battery technologies for large-scale energy storage are listed below.

- *Lead-acid* batteries are the most mature and economical batteries for applications where weight is of little concern. It comprises of two lead plates, a positive plate covered with lead oxide and a negative made of sponge lead. The plates are submerged in the electrolyte (sulfuric acid and water). These batteries are simple to manufacture and have low self-discharge. However, lead-acid batteries have a limited cycle life, low specific energy (35-50 Wh- kg^{-1}) and are non-environmentally friendly [1, 2].

- *Sodium-Sulfur* battery is a molten salt battery comprising of sodium and sulfur. This type of battery typically operates from 300° - 350°C and has a high specific energy (180-220 Wh kg^{-1}), long life cycle, high efficiency and can be manufactured from low-cost materials. However, due to high-temperature operation and the highly corrosive nature of the sodium polysulfides, it poses operational safety concern such as fire, corrosion on the insulators, the highly oxidizing pure sodium element restricts the application of this battery to stationary storage application [3].

- *Lithium-ion* batteries are the most widespread and popular batteries owing to their long-term stability, high specific energy (80-240 Wh kg^{-1}), low cost, high cycling efficiency, and low self-discharge. These batteries are considered as the battery of choice for next-generation electric vehicles as well as plug-in hybrid vehicles. However, limited lithium resource, safety concern associated with the high volatility of lithium element, cost issue and sophisticated battery management system are a few disadvantages of lithium-ion batteries [4, 5].

- *Redox flow batteries (RFBs)* are rechargeable batteries that can resolve the constraint of secondary batteries in a large-scale application. RFB converts the chemical energy of two redox couples stored in external tanks to electrical energy. The energy conversion occurs when redox couples interact with electrodes after being pumped from the tank to the cells. All vanadium, Iron-Chromium, Zinc-Bromine, Bromine-Polysulphide, and Zinc-Cerium are among the few RFBs. Decoupling of power and capacity, low self-discharge, low maintenance cost and a possibility of deploying in large scale are some of the attractive features of these batteries [6, 7]. Some of the disadvantages are low energy density, upfront cost and requirement of complex hardware. The technology is progressing with the improved method of overcoming the aforementioned problems and making it one of the promising candidate for large-scale energy storage [6-8].

  Redox flow batteries can be classified by the type of active species used as the electrolyte. Many types of RFB have been investigated and developed since the first demonstration.

  Iron/chromium system employs the aqueous solution of the ferric/ferrous (Fe^{2+}/Fe^{3+}) redox couple as catholyte and chromic/chromous (Cr^{2+}/Cr^{3+}) redox couple as anolyte. The common supporting electrolyte in these type of RFBs is hydrochloric acid. The main disadvantage of iron/chromium RFB is that standard potential of Cr^{2+}/Cr^{3+} couple lies close to hydrogen evolution reaction, which causes side reactions.

  Vanadium/Bromide (Halide) uses VBr_2/VBr_3 as negative couples and the $Cl^-/BrCl_2$ (or $Br^-/ClBr_2$) couple as the positive electrolyte. The standard potential of the VBrRBF is 1.3 V. The main disadvantage of this system is the risk of emission of toxic bromine vapor.

  Bromide/Polysulfide RFB uses sodium tribromide ($NaBr_3$) solution as positive electrode and sodium polusulfide (Na_2S_2) as negative electrolyte. The main advantage of this system is the use of inexpensive electrolyte in the both side. However, the challenge of electrolyte crossover remains, resulting in the sulfur precipitation and risk of H_2S and Br_2 emission.

Vanadium/Air RFB employs V^{2+}/V^{3+} redox couple in the negative side and H_2O/O_2 in the positive side. The standard potential for this kind of cell is 1.5 V. The utilization of air as the redox couple reduces the weight and increases the power density.

Zinc/Bromide RFB utilizes bromide ions or molecules in the positive side in the aqueous phase. The negative electrode is metal electrode (zinc). The advantage of this kind of RFB is the high cell potential (1.85 V). A potential concern for this kind of RFB is the formation of toxic Br_2.

Among the RFBs, VRFB has received much attention in recent years for their widespread commercialization due to the use of same vanadium element in both positive and negative half-cell and hence avoid the issue of cross-contamination between the two cells.

2.2 Vanadium Redox Flow Battery

The development of VRFB has progressed significantly over the last two decades, resulting in its extended application from kW to MW scale. National Aeronautics and Space Administration (NASA) published the early works on redox flow battery in the 1970s and since then, several groups have begun to explore RFB. The first successful demonstration of VRFB employing vanadium in sulfuric acid solution in each half of the cell was performed by Maria Skyllas-Kazacos and coworkers at the University of New South Wales in the 1980s [9]. The VRFB pioneered by Maria Skyllas-Kazacos and coworkers at the University of New South Wales in the 1980s [9] has shown great promise for large scale application.

Further VRFB development and demonstration took place in Thailand, Japan and Australia [6, 8]. Today, a number of companies, such as Vfuel, Enerox GMbH, Cellennium, redT energy, Sumitomo, H2 AEC, Proxhima, Rongke Power etc. around the world are developing VRFB on a commercial scale. The target of VRFB commercialization includes large scale storage, power supply in isolated areas, load levelling and backup applications [10]. The ever-increasing use of renewables has paved the path for large scale commercial VRFB.

2.2.1 Working Principle of VRFB

VRFB employs a mixture of vanadium compounds dissolved in sulfuric acid as the electrolyte to store the chemical potential energy. VRFB exploits the ability of vanadium to exist in four different oxidation states in solution and uses this characteristic to make a battery with only one electroactive element. In VRFB, V^{+4}/V^{+5} (VO^{2+}/VO_2^{+}) redox couple serves as the positive electrolyte or catholyte and V^{2+}/V^{3+} serves as the negative electrolyte or anolyte with sulphuric acid as supporting electrolyte. The electrolyte of VRFB is generally prepared by dissolving vanadium pentoxide or vanadium sulphate in the sulphuric acid. The vanadium is below 2 M while the concentration of sulphuric acid is kept less than 5 M due to safety in acid handling. Due to the solubility limit of vanadium ions in sulphuric acid, the concentration of vanadium is kept below 2 M. To avoid the precipitation of the electrolyte, the system is operated between 10° to 40°C.

VRFB consists of an electrochemical cell and two tanks to store the electrolytes as shown in Figure 1.

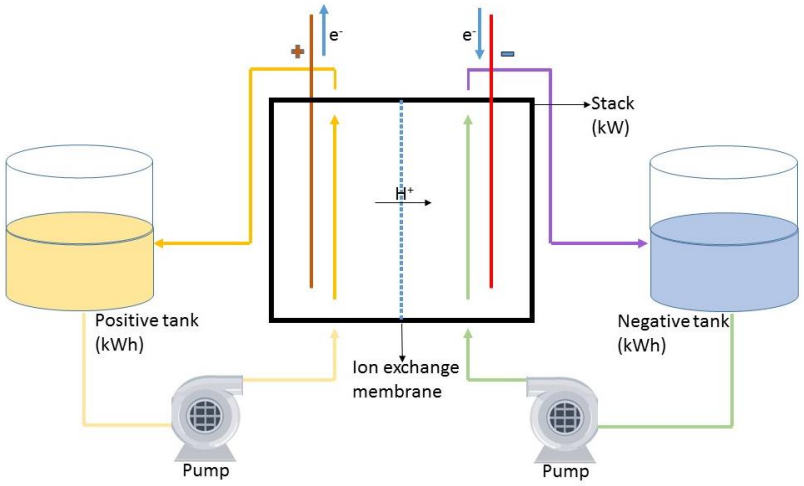

Figure 2.1 Schematic diagram of VRFB.

During charge and discharge following electrochemical reactions occur in each half of the cell.

Positive side, $VO^{2+} + H_2O \rightleftharpoons VO_2^{+} + 2H^{+} + e^{-}$ $E = 1.000\ V$

Negative side, $V^{3+} + e^{-} \rightleftharpoons V^{2+}$ $E = -0.255\ V$

Overall reaction, $V^{2+} + VO_2^{+} + 2H^{+} \rightleftharpoons VO^{2+} + V^{3+} + H_2O$ $E = 1.255V$

During discharge, V^{2+} ions in the negative tank are oxidized to V^{3+} while VO_2^+ ions in the positive tank are reduced to VO^{2+}. A reverse reaction occurs during the charging process. The presence of protons H^+ and water H_2O in the cathodic (positive side) reaction is to maintain the charge balance of the cell. Under long operation, electrolyte transfer occurs and causes the imbalance of electrolyte due to the convective transport of the electrolyte species. The net transfer of the electrolyte depends on the type of membrane (cation or anion exchange) used in the stack.

2.2.2 Advantages and Disadvantages of VRFB

VRFB has the following advantages:

- Decoupled power density and energy storage capacity: Energy capacity, which is a function of the concentration of the reactants and volume of electrolyte, and power, which is a function of electrode area and cell number in the stack can be optimized independently. This makes VRFB as one of the promising candidates for the large-scale energy storage application [7].
- Same electrolyte chemistry in both half of the cell: In VRFB, the same electrolyte with different oxidation state is used in both half of the cell. The different electrolyte species from one-half of the cell can crossover to the other half, as ion exchange membrane cannot fully block the species transport. However, due to the use of the same electrolyte in both half, the crossover is not detrimental and hence does not affect the performance [7].
- Fast response and high efficiency: Due to fast response time, the system can be utilized in uninterrupted power supply (UPS) like application, thus serves as an attractive alternative to lead-acid batteries and diesel generators [11]. VRFB is suitable for peak shaving and load levelling application due to high round trip efficiency.
- Deep discharge and no standby loss: Unlike other batteries (Li-ion and lead acid), VRFB can be fully discharged to a very low state of charge (SOC) and can be normally charged even after keeping it in discharging condition for a long duration. There is no standby loss, as the electrolyte is stored in the electrolyte tank.

- Low maintenance and longer lifetime: Theoretically, with proper remixing or rebalancing, depending on the type of membrane, the electrolyte can operate an infinite number of charging/discharging. The maintenance cost for VRFB is also negligible. Due to these characteristics, the battery is suitable to operate in a remote location where a standalone system is preferred.

In spite of these advantages, VRFB also suffers some disadvantages, which limit its operation, such as:

- Low specific energy: It is the major disadvantage of VRFB. In comparison to Li-ion and nickel metal hydride battery, the specific energy is around 25 Wh kg^{-1}. The low solubility of vanadium sulfate limits the energy density. The low energy density of VRFB makes it bulky and restricts its use in the mobile application.
- Limitation of operating temperature: The operating temperature of VRFB is generally between 10°C to 40°C. If the temperature reaches above 40°C, the positive electrolyte is precipitated while operation below 10° C results in irreversible precipitation of the negative electrolyte [12, 13]. Therefore, the narrow windows of operation temperature restrict its application in harsh climate areas [14].
- Cost of vanadium: Vanadium is expensive metal, which drive the cost of system. The upfront cost of vanadium is high, but it should be analyzed as the long-term investment.
- Environmental issue: Sulfuric acid is used as the supporting electrode in vanadium redox flow batteries. In case of spillage, it has detrimental effect on the environment. Therefore, the electrolyte is stored in the double container to avoid any kind of spillage.

2.2.3 Components of a VRFB Cell

The electrochemical cell of the VRFB consists of the following items:

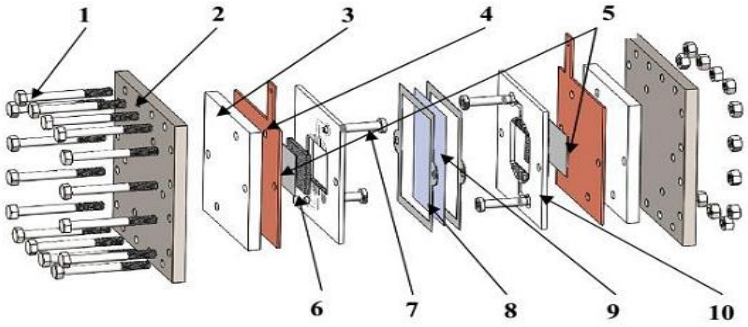

Figure 2.2 Components of VRFB cell.

1- Nut and bolt: For assembly of cell components by providing uniform pressure between each component.

2- End plates: To provide uniform compression during the cell assembly. Usually, material such as stainless steel, composites, plastics etc. are used as end plates.

3- Insulator plate: To prevent shorting between the end plate and the current collector

4- Current collector: To allow the collection of current. Typically, the collector is made of copper plates as they have excellent electrical conductivity.

5- Graphite electrode or Bipolar plate (BP): To separate the electrolyte from the metal current collector. It is made of graphite materials and is chemically inert with very high electrical conductivity. In a stack, BPs connects the cells in series.

6- Graphite felt electrode: To facilitate the redox couple reactions. Electrode with a higher surface area is necessary to provide abundant reaction sites in VRFB. As BP has a very low surface area due to its smoothness, carbon or graphite felt serve perfect. It has a high surface area, which can be significantly enhanced after pre-treatment. Similarly, graphite felts are chemically inert to withstand the highly corrosive environment and are conductive to transport current to BP.

7- Nozzle: To connect the flow frame to the external pipe from the electrolyte tank. The nozzle is typically made from polyvinyl chloride (PVC) material.

8- Gasket: To seal the flow frame and the membrane, usually silicon gaskets are used.

9- Membrane: To separate the two half-cells, and partially permits passage of the charge balancing ions like H^+, $SO_4^{2-}$and HSO_4^-[15]. Both anion and cation types can be used in VRFBs.

10- Flow frame (FF): To provide the window for the accommodation of the graphite felt. It consists of the milled channel for the even distribution of the electrolyte across the graphite felt. Depending upon the design of the cell, FF can be of PVC or silicon material.

2.2.4 Figure of Merit of VRFB

VRFB cells are charged and discharged at various current densities using a battery tester, which consists of a power supply and electrical loads. The performance of VRFB is evaluated by cell cycling. The important parameters to evaluate the performance of a VRFB are cell efficiencies, namely coulombic, energy and voltage efficiencies, which are also used to compare cell performance.

Coulombic efficiency (CE) is the ratio of charge extracted during the discharge process to the charge supplied during the charge process as expressed in Equation 2.1.

$$\eta_{coulombic} = \frac{Q_{discharge}}{Q_{charge}} = \frac{\int i_{discharge}(t)dt}{\int |i_{charge}(t)|dt} \tag{2.1}$$

Where $Q_{discharge}$ is the charge extracted from a cell in Amp hr, Q_{charge} is the charge supplied during the charge, $i_{discharge}$ is the current during discharge in Amp, i_{charge} is the current during charge and t is the time in hours. Coulombic efficiency depends on the properties of the membrane.

Energy efficiency (EE) is the ratio of energy acquired during discharge to the energy supplied during charging as expressed in Equation 2.2.

$$\eta_{energy} = \frac{\int P_{VRFB,discharge}(t)dt}{\int |P_{VRFB,charge}|(t)dt} \tag{2.2}$$

Where $P_{VRFB,discharge}$ is the energy delivered by the battery during discharge, $P_{VRFB,charge}$ is the energy supplied to a battery during charge in Watt, and t is time in hours.

Voltage efficiency (VE) is measured as the ratio of cell/stack voltage during discharge to the voltage during charge. It is also a measure of Ohmic and polarization losses during cell cycling as expressed in Equation 2.3.

$$\eta_{voltage} = \frac{\int U_{VRFB,discharge}(t)dt}{\int U_{VRFB,charge}(t)dt} \quad (2.3)$$

Where $U_{VRFB,discharge}$ is the voltage of the cell during discharge, $U_{VRFB,charge}$ is the voltage of the cell during charge and is the time in hour.

If mechanical losses (pump power) are not considered, then voltage efficiency is defined as the ratio of energy efficiency and coulombic efficiency as shown in Equation 2.4

$$\eta_{voltage} = \frac{\eta_{energy}}{\eta_{coulombic}} \quad (2.4)$$

Area-specific resistance (ASR) is one of the important parameters besides efficiencies used to compare different VRFB cell designs. The ASR during constant current charge and discharge is provided by Equation 2.5.

$$\rho = \frac{V_o(1 - VE)}{j(1 + VE)} \quad (2.5)$$

Where V_o is open circuit voltage during charge and discharge (~1.38 V), j is the current density in A cm^{-2}, VE is the voltage efficiency and ρ is the cell resistance in Ω cm^2.
Equation 2.5 is obtained based on the following derivation:

The average voltage on a charge,	$V_{charge} = V_0 + j.\rho$
The average voltage on discharge,	$V_{discharge} = V_0 - j.\rho$
The voltage efficiency,	$VE = V_{discharge}/V_{charge}$
Or,	$VE = (V_0 - j.\rho)/(V_0 + j.\rho)$
Or,	$VE.V_0 + VE.j.\rho = V_0 - j.\rho$
Or,	$j.\rho\,(1 + VE) = V_0(1 - VE)$
Or,	$\rho = \frac{V_0}{j}.(\frac{1 - VE}{1 + VE})$

ASR is also known as wet cell resistance since it provides a summation of all the resistances during cell operation. ASR is the best method for comparing cell sizes, design and the materials used.

2.3 Electrochemistry of Vanadium Redox Flow Battery

2.3.1 Nernst Equation

As mentioned earlier in section 2.2, the overall reaction in the VRFB is given by the following equation:

$$V^{2+} + VO_2^+ + 2H^+ \leftrightarrows VO^{2+} + V^{3+} + H_2O \qquad E = 1.255V \tag{2.6}$$

The equilibrium voltage E of a single cell is determined by introducing the Equation 2.6 into the Nernst Equation,

$$E = E^o + \frac{RT}{nF}\ln\left[\left(\frac{C_{VO_2^+}\,\gamma_{VO_2^+}\,C^2_{H+}\gamma^2_{H+}}{C_{VO^{2+}}\,\gamma_{VO^{2+}}}\right)\left(\frac{C_{V^{2+}}\gamma_{V^{2+}}}{C_{V^{3+}}\gamma_{V^{3+}}}\right)\right] \qquad [V] \tag{2.7}$$

Where R is the gas constant, T is the temperature, n is the number of electrons involved during the reaction, F is the Faraday constant, C is the concentration, γ is the activity coefficient and E^o is the standard electrode potential for the redox reaction [16].

Upon rearrangement of the activity and concentration into separate term, Equation 2.7 will be as follow:

$$E = E^o + \frac{RT}{nF}\ln\left[\left(\frac{\gamma_{VO_2^+}\,\gamma_{V^{2+}}\gamma^2_{H+}}{\gamma_{VO^{2+}}\gamma_{V^{3+}}}\right)\left(\frac{C^2_{H+}C_{VO_2^+}C_{V^{2+}}}{C_{VO^{2+}}\,C_{V^{3+}}}\right)\right] \qquad [V] \tag{2.8}$$

Activity coefficient is a thermodynamic factor that cannot be measured directly. The electron number involved in VRFB reaction is equal to one. Thus, formal potential $E^{o\prime}$ is introduced to hide the activity coefficient from Equation 2.8 [17].

$$E = E^{o\prime} + \frac{RT}{nF}\ln\left[\left(\frac{C_{VO_2^+}\,C^2_{H+}}{C_{VO^{2+}}}\right)\left(\frac{C_{V^{2+}}}{C_{V^{3+}}}\right)\right] \qquad [V] \tag{2.9}$$

Nernst Equation is possible applicable only in case of dilute concentration of hydrogen ion and vanadium species. At high concentration, the Nernst Equation should always include activities. Therefore, to describe all-important parameters in Equation 2.9, we consider the redox reactions taken place at a standard condition, namely: 1 M vanadium species concentration, temperature at 25 °C and all activity coefficients γ_i equal to one.
If formal potential (measured value) is not available, standard potential can be used without activity coefficients assuming identical activity coefficients of products to reactants [17]. Therefore, the final equation can be written as

$$E = E^o + \frac{RT}{nF}\ln\left[\left(\frac{C_{VO_2^+}\, C^2_{H+}}{C_{VO^{2+}}}\right)\left(\frac{C_{V^{2+}}}{C_{V^{3+}}}\right)\right] \qquad [V] \tag{2.10}$$

2.3.2 Standard Potential

The standard potential E^o in the Nernst Equation is of key importance as it gives reaction potential at standard condition. There are two methods to determine the standard potential.

Thermodynamic approach: This method relies on Gibbs free energy ΔG,

$$\Delta G = \Delta H - T\Delta S \qquad \left[\frac{J}{mol}\right] \tag{2.11}$$

Where ΔH = change in enthalpy [J/mol] and ΔS = change in entropy [J/K.mol]. The change in free energy that occurs with the formation of 1 M of the substance from the component at standard condition (25°C,101 kPa and 1M) is given by

$$\Delta G^o = \Delta H^o_{reaction} - T\Delta S^o_{reaction}\left[\frac{kJ}{mol}\right] \tag{2.12}$$

Where, $\Delta H^o_{reaction}$ and $\Delta S^o_{reaction}$ are the standard reaction enthalpy and entropy, which is a difference between reactants and products molar formation.

$$\Delta H^o_r = \sum_{products} \Delta H^o_{f,product} - \sum_{reactants} \Delta H^o_{f,reactant}\left[\frac{kJ}{mol}\right] \tag{2.13}$$

$$\Delta S^o_r = \sum_{products} S^o_{f,product} - \sum_{reactants} S^o_{f,reactant}\left[\frac{J}{K.\,mol}\right] \tag{2.14}$$

The standard reaction enthalpy can be calculated by incorporating the thermodynamic data

from Table 2.1 into Equation 2.13 provides standard reaction enthalpy as given in Equation 2.15. Similarly, using thermodynamic data from Table 2.1 in Equation 2.14 gives standard reaction entropy.

$$\Delta H^{o}_{reaction} = -155.6 \frac{kJ}{mol} \quad (2.15)$$

$$\Delta S^{o}_{reaction} = -121.7 \frac{J}{K.mol} \quad (2.16)$$

Table 2.1 Thermodynamic data for all species involved in VRFB at 25°C

Compound	ΔH° formation [kJ/mol)	ΔG° formation [kJ/mol)	S° formation [J/K.mol)	State
H+	0	0	0	aqueous
H_2O	-285.8	-237.2	69.9	aqueous
V^{2+}	(-266)	-218	(-130)	aqueous
V^{3+}	(-259)	-251.3	(-230)	aqueous
VO^{2+}	-486.6	-446.4	-133.9	aqueous
VO_2^{+}	-649.8	-587	-42.3	aqueous

The reaction of free energy change and the potential difference can be related as $\Delta G = -nFE$. Thus, the standard potential E^o can be calculated by combining it with Equation 2.12.

$$E^o = -\frac{\Delta G^o}{nF} = -\frac{\Delta H^o_{reaction} - T\Delta S^o_{reaction}}{nF} [V] \quad (2.17)$$

The standard potential E^o at 25°V is 1.23 V.

Standard reduction potential: The standard potential of a cell can be calculated by subtracting the reduction potential of the cathode to anode standard potential.

$$E^o = E^o_{cathode} - E^o_{anode} = 1.255\ V$$

The cathode and anode potential value is 1V and -0.255 V respectively. However, this method is only valid at a temperature.

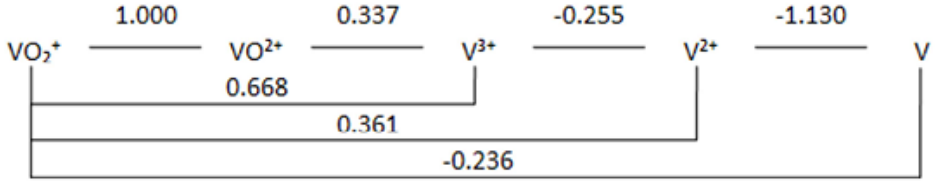

Figure 2.3 Potential diagram of vanadium species in strong acid solutions [18].

2.3.3 State of Charge (SOC)

SOC refers to the percentage of V^{2+} ion present in the negative electrolyte and V^{5+} ion present in the positive electrolyte. It is the most frequent terminology used in VRFB operation. It is not directly related to the performance of the battery, however, during operation, the upper and lower SOC are continuously monitored and controlled. Its value varies from 0 to 100%. Battery having 100% SOC means V^{2+} is 100% and V^{3+} 0%, whereas battery having 0% of SOC means 100% V^{3+} and 0% V^{2+} in the negative side. A similar condition applies to the positive side of the battery. State of charge is given by the concentration of vanadium species.

$$\mathrm{SOC} = \frac{\mathrm{C_{V^{2+}}}}{\mathrm{C_{V^{2+}} + C_{V^{3+}}}} = \frac{\mathrm{C_{VO_2^+}}}{\mathrm{C_{VO^{2+}} + C_{VO_2^+}}} \tag{2.18}$$

During the cell operation, open circuit voltage (OCV) can be used to calculate the SOC where the Nernst Equation can be used to calculate OCV.

$$\mathrm{OCV} = \mathrm{E_{cell}} = \mathrm{E_{cell}^o} + \frac{\mathrm{RT}}{\mathrm{nF}} \ln\left[\left(\frac{\mathrm{C_{H+}^2 C_{VO_2}^+ C_{V^{2+}}}}{\mathrm{C_{VO^{2+}}\, C_{V^{3+}}}}\right)\right] \qquad [V] \tag{2.19}$$

Where, $\mathrm{E_{cell}^o}$, R, T, n, F and C denotes the standard cell potential, gas law constant, temperature, number of electrons transferred in the reaction, Faraday constant and concentration of ions, respectively.

During the operation, $\mathrm{C_{VO_2}^+} = \mathrm{C_{V^{2+}}}$, $\mathrm{C_{VO^{2+}}} = \mathrm{C_{V^{3+}}}$ and also, $\mathrm{C_{VO_2}^+} \propto \mathrm{SOC}$, $\mathrm{C_{VO^{2+}}} \propto (1 - \mathrm{SOC})$. Therefore,

$$\mathrm{C_{VO_2^+}} = \frac{\mathrm{C_{VO_2^+}}}{\mathrm{SOC^*}} \text{ and } \mathrm{C_{VO^{2+}}} = \frac{\mathrm{C_{VO^{2+}}}}{1-\mathrm{SOC^*}}$$

Where, $\mathrm{SOC^*}$ is the state of charge expressed in fraction.

Replacing these terms in Equation 2.19, one gets,

$$\mathrm{OCV} = \mathrm{E_{cell}} = \mathrm{E_{cell}^o} + \frac{\mathrm{RT}}{\mathrm{nF}} \ln \mathrm{C_{H^+}^2} + \frac{\mathrm{RT}}{\mathrm{nF}} \ln\left(\frac{\mathrm{SOC^{*2}}}{(1 - \mathrm{SOC^*})^2}\right) \text{ [V]} \tag{2.20}$$

Equation 2.20 shows the theoretical calculation of SOC from OCV. While using the Nernst Equation, it is necessary to use activities rather than concentration and should also include a membrane junction correction. Based on experiments of a cell using electrolyte concentration of 1.6 M $V^{3.5+}$ in 4.5 M H_2SO_4 (the electrolyte we used for this project), the Nernst Equation gives:

$$\begin{aligned} OCV = {} & 1.38 - 0.00193(T - 273) \\ & + \frac{RT}{nF} \ln\left[\frac{(1.8 \times SOC' + 3)(1.8 \times SOC' + 4.8).SOC'^2}{(1 - SOC')^2}\right] \end{aligned} \tag{2.21}$$

Figure 2.4 shows the plot between OCV and SOC using Equation 2.21.

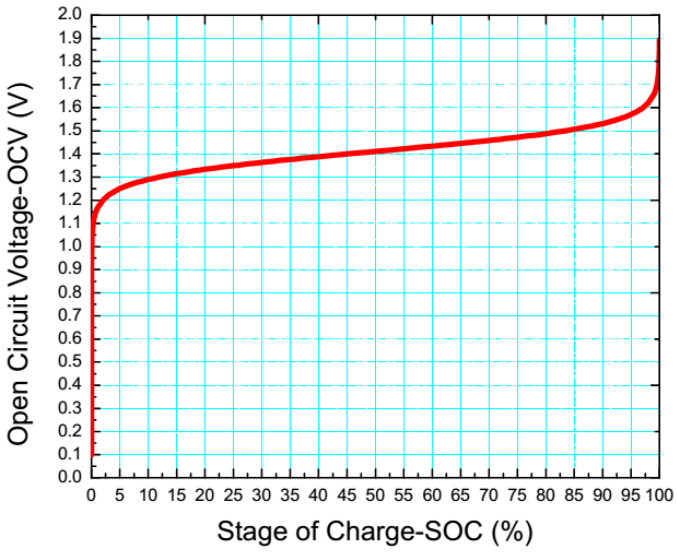

Figure 2.4 Relation between OCV and SOC according to Equation 2.21.

During the operation of the battery, SOC is always kept between the upper and lower limit, usually between (10-20% to 80-85%), so as not to operate in the region of the exponential rise of fall of OCV.

2.3.4 Electrode Kinetics

Equilibrium electrode reactions are defined by the Nernst Equation, which is already described in section 2.3.1. Other models such as Tafel Equation and Butler-Volmer models are widely used for the electrode kinetics study.

Current-overpotential equation

The Butler-Volmer Equation for kinetics is derived from the current-overpotential relation as given in Equation 2.26.

$$i = i_o \left[\frac{C_o(0,t)}{C_o^*}\exp(-\alpha f\eta) - \frac{C_R(0,t)}{C_R^*}\exp\big((1-\alpha)f\eta\big)\right] \quad (2.22)$$

Where C_o and C_R are bulk concentrations, $C_o(0,t)$and $C_R(0,t)$ are surface concentration of reduced and oxidised species, i_o is exchanged current, η is overpotential and α is the transfer coefficient. Transfer coefficient measures the symmetry of energy between forward or reverse current. A perfectly symmetric system has a value of 0.5, but the value may range from zero to one.

If the solution is stirred, i.e. there is no mass transfer or negligible mass transfer, hence the bulk electrolyte concentration and the electrolyte concentration at the surface of the electrode are same. In this situation, the Equation 2.22 becomes the *Butler-Volmer* Equation (Eq. 11), which is one of the most fundamental relationships.

$$i = i_o \left[\exp(-\alpha f\eta) - \exp\big((1-\alpha)f\eta\big)\right] \quad (2.23)$$

At characteristically small overpotentials, Equation 2.23 reduces to the linear form in Equation 2.24.

$$i = -i_o\, f\eta \quad (2.24)$$

From a plot of i versus η, i_o may be easily obtained from the slope of linear regression fit.

Tafel plot

In simple chemical kinetics, the rate of reaction is a function of temperature. The increase in temperature causes an exponential rise in rate constant K, which is described by the Arrhenius Equation. Similarly, the rate of electron transfer increases as the energy provided

to the electrons rises. While the rate of electron transfer is temperature dependent, its dependence on the electrode potential is very high. At fixed temperature [19,20].

$$I = a + b \exp \eta \tag{2.25}$$

Which is known as Tafel Equation. Where η= Overpotential (i.e. the difference between applied potential and equilibrium potential), a and b are empirical constants. The plot of $\log_{10}$I against η should be linear. Practically, such a plot is not linear except over a narrow range of potential [20].

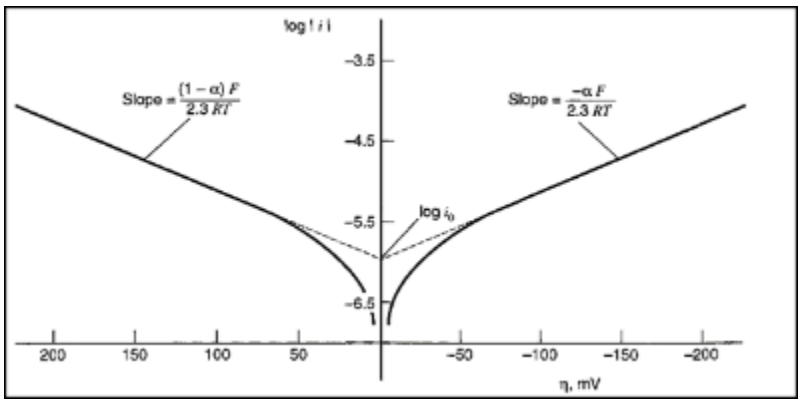

Figure 2.5 Tafel plot for a cathodic and anodic branch of the current-overpotential curve [19].

The Tafel Equation holds when the overpotential applied to a system is 100 mV or greater. In this region, the logarithm of current versus overpotential is used to evaluate the kinetic parameters. In such a plot, the slopes of cathodic and anodic branches for an electron transfer system are given by Equations 2.26 and 2.27 [20].

$$\text{Anodic branch:} \qquad \text{Slope} = \frac{-\alpha F}{2.3RT} \tag{2.26}$$

$$\text{Cathodic branch:} \qquad \text{Slope} = \frac{(1-\alpha)F}{2.3RT} \tag{2.27}$$

From Equation 2.26 and 2.27, the α for the reaction can be determined with ease. The linear segment of each branch may be extrapolated back to its intercept to determine the exchange current density of the system.

2.4 Losses in VRFB

When current starts to flow, the equilibrium condition no longer exists and cell voltage differs from equilibrium potential. The measured voltage of the battery differs from the equilibrium potential. This difference is often referred to as overpotential. The cell potential during operation is lower than the cell potential at equilibrium (i.e. OCV) as shown in Equation 2.28.

$$E_c = E_0 - iR_i - \eta_{act} - \eta_{conc} \quad (2.28)$$

Where E_c is operating cell voltage, E_0 is open circuit voltage, i is current density, R_i is area specific resistance, η_{act} is activation overpotential and η_{conc} is concentration polarization.

Polarization curve is often used to investigate overpotential. Polarization curve is obtained by plotting the voltage against the different current densities. It provides an overview of different losses occurring within the cell. Therefore, the importance is also growing in VRFB. Figure 2.6 depicts the polarization curve showing three distinct regions, namely activation, ohmic and mass transport polarization.

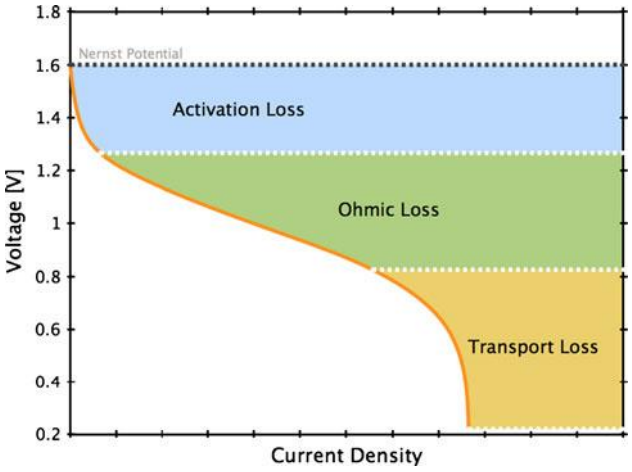

Figure 2.6 Polarization curve of VRFB during charging [21].

Polarization curve obtained during discharge is of more interest than during charging. During charging, the cell cannot be charged at higher current density as it can reach higher cell voltage, which will eventually deteriorate the electrode and BP. Discharging can be carried out at limiting current density without any risk.

The different types of polarization are explained as follows:

Activation polarization

The energy required to initiate the charge transfer is associated with activation overpotential. This is due to a slow charge transfer reaction at the interface between the electrode and the electrolyte, and is often observed at low current density. This type of loss is reduced with pre-treatment of the electrode.

Ohmic polarization

Ohmic polarization in a cell comprises of ionic transport resistance (electrolyte and membrane), electronic resistance of components (current collector, graphite felt and BP) and contact resistant at interfaces (current collector to BP, BP to the electrode). The linear part of the polarization curve exhibits the Ohmic loss and is obtained from the ratio of voltage to current.

Concentration polarization

Concentration overpotential is the result of the difference in electrolyte concentration between the electrode surface species and the bulk solution. Electron transfer occurs within the few nanometres of electrolyte adjacent to the electrode, which results in different layers of electroactive species. To keep up with the current, the reaction layer adjacent to the electrode surface should be continuously supplied with the reactants. When the rate of reaction is rapid, fresh reactants do not reach the surface of the electrode on time, resulting in concentration overpotential [22]. This overpotential is affected by flow rate, current density and electrolyte concentration.

The aforementioned polarization losses are not exclusive; all of them contribute whenever the current is flowing through the cell. However, the dominant effect of each type is observed in a particular region of the polarization curve [23].

In addition, there are also other losses occurring during the VRFB operation such as pumping loss, self-discharge loss, shunt current loss and capacity loss. Viscous flow resistance, which depends on the electrode permeability and viscosity of electrolyte can lead to a differential pressure between inlet and outlet. This differential pressure is directly

related to power consumption of the pumps. Self-discharge is the result of vanadium ions crossover across the membrane. Discharge rate depends on the diffusion coefficient of vanadium ions [24]. Shunt current loss occurs in a multi-cell stack due to the conductivity of the electrolyte and non-zero electrical field potential gradient. It affects VRFB performance by decreasing the energy transfer efficiency and shortening the cycle life [25]. Capacity loss is of two types namely, reversible capacity loss and irreversible capacity loss. During operation, the proton migrates across membrane along with water molecule, resulting in electrolyte imbalance. This type of loss is known as a reversible capacity loss. Some sulfate, bisulfate and vanadium ions are also transported across the membrane together with the water molecules. Hence, electrolyte rebalancing is required to prevent such loss. On the other hand, irreversible capacity losses are caused by electrode degradation, overcharging, surface passivation of the current collector, leakage of electrolyte, high-temperature operation etc.

2.5 Research Progress in VRFB

VRFB technology pioneered and developed by Maria Skyllas-Kazacos and her co-workers at the University of New South Wales, Australia in the 1980s. It is now emerging as one of the promising candidates for large-scale energy storage. However, despite being commercially available in the market, the capital investment for this battery is quite high. The price per kWh of vanadium redox flow battery ranges from US$ 500 to US$ 1000 (for capacity $\geq$ 100 kWh), making the capital investment higher compared to other storage systems. The major cost factors of VRFB are the membrane, electrode, and electrolyte. Research is ongoing toward price reduction of these expensive components as well as reducing the footprint of this system so that it can be applied in limited space with the better performance [7].

2.5.1 Electrolyte

VRFB use four different vanadium oxidation states, V^{2+}/V^{3+} as negative electrolyte and V^{4+}/V^{5+} as the positive electrolyte. Sulphuric acid is used as supporting electrolyte with a concentration often less than 5 M, due to safety in acid handling. Hence, the concentration

of vanadium is also taken into consideration and kept below 2 M to control the viscosity of the solution [12, 26].

The concentration of the vanadium species governs the energy density of a VRBF, and thus the energy capacity is directly proportional to concentration and/or volume of the solution. However, precipitation of solid vanadium oxides restricts the upper limit of the concentration, along with the temperature. The concentration of vanadium above 2M results in precipitation of V_2O_5 at a temperature above 40°C in the positive electrolyte and precipitation of VO at the temperature below 10°C in the negative electrolyte [13, 28]. Thus temperature, concentration and state of charge of the vanadium electrolyte determine the optimal concentration of vanadium used in the VRFB electrolyte [29, 30].

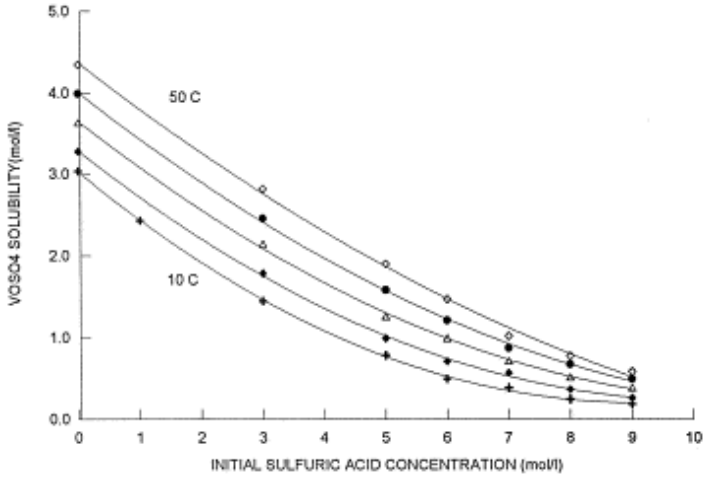

Figure 2.7 Variation in the solubility of $VOSO_4$ with a concentration of sulfuric acid [27].

The research on electrolyte is more focused on finding additives to increase the operating temperature window and enhancing the energy density as well as looking for alternative supporting electrolytes. To achieve these objectives, research on organic and inorganic additives that are stable in the long run, environmentally friendly, low cost and resistive to V^{5+} corrosive environment is progressing on. Organic compounds with carboxyl (oxalic acid, sodium oxalate, potassium oxalate, EDTA disodium salts), multi-functional groups (Lactic acid, Cysteine, Ascorbic acid, Citric acid, Ammonium citrate, Tannic acid) and alcohol (Resorcinol, Pinacol, Pyrogallol, Xylose, Glucose, PVA) have been investigated and proposed [31-36].

Regarding alternative supporting electrolytes, Skyllas-Kazacos research group has investigated the use of mixed halides such as mixed HCl and HBr and found that the vanadium concentration can be increased to ~3.5M in 12 M mixed HCl and HBr solution leading to substantial increased in energy density. However, further research is required to bring it to commercialization, as there is potential chlorine and/or bromine gas evolutions associated with the use of this supporting electrolyte [37]. In recent year, researchers from Pacific Northwest National Laboratory (PNNL) have also managed to raise the maximum concentration of vanadium to 2.5 M by adding HCl solution into the existing H_2SO_4 supporting electrolyte [38]. At present, this system is in the process of commercialization.

2.5.2 Membranes

The ion exchange membrane physically separates two half-cells containing the negative and the positive electrolyte, which prevents self-discharge but allows the transport of charge to keep electrical neutrality. Ion exchange membrane ideally must have properties, such as high selectivity for the charge transporting species with a minimum transport of vanadium cations, minimum transport of water across the membrane, mechanical stability and low cost [39, 40]. For VRFB applications, both, anion and cation type of membrane can be used.

The VRBF performance is directly correlated with the properties of the membrane. The properties govern the coulombic efficiency and contribute a large portion of the ohmic losses. For example, a thick separator results in high cell resistance, whereas a thin separator results in the fast crossover with electrolyte imbalance [41].

In VRBF applications, mainly two types of separator are used, namely cation exchange membrane and anion exchange membrane. Membranes containing negatively charged groups such as $–SO_3^-$, $-COO^-$, $-PO_3H^-$, etc. are cation exchange membranes and they are permeable to cations while restricting anions to pass through. On the other hand, membranes containing positive groups such as $–NR_3^+$, $-SR_2^+$,$-NH_3^+-$, etc. allowing anions to pass through are called anion exchange membranes [42].

Nafion membranes are widely used cation exchange membranes (CEM) for VFBF application despite their high cost due to excellent chemical and mechanical stability. A Nafion membrane consists of an array of hydrophilic channels, and its ion exchange properties are due to the sulphonate ($–SO_3^-$) group with fixed sites in the membrane. The sulphonate sites repel anions and are perm-selective for counter ions [43]. The exposure of the membrane to the dilute electrolyte i.e. below 0.1 mol L^{-1} restricts the anion from entering. However, if the concentration is above 1 mol L^{-1}, it uptakes anions with additional cations, which results in the transport of electrolyte [44, 45]. In addition to ionic transport, diffusion and osmotic drag results in water transport across the membrane[46].

For cost reduction, fluorinated Nafion membrane, membranes with partially fluorinated (e.g., anion FAP membrane from Fumatech GmbH) and non-fluorinated (Polyether ether ketone–PEEK membranes [47], sulfonated PEEK membranes [48], hydrocarbon-based CEM, etc.) membrane have been developed [49]. Crossover is one of the serious problems that cause an imbalance of electrolyte and charge imbalance, resulting in the reduction of usable energy. In this regard, the anion exchange membrane (AEM) are attractive due to their ability to contain the crossover of cationic species [50]. AEM reduce the crossover of vanadium by repelling the positively charged vanadium ions by positively charged fixed ionic groups. However, AEM also possesses certain disadvantages like swelling due to high water uptake, low conductivity etc. [50]. To resolve the issue of cross over different membranes, such as amphoteric membrane [51], bipolar membrane [52] and use of a combination of anion and cation exchange membranes [53, 54] have been proposed.

2.5.3 Electrodes

The electrodes play a key role in VRFB performance by providing the electroactive sites for redox couples. The electrodes affect the activation and concentration polarization, which govern the energy efficiency of the VRFB. Ideal electrodes for VRFB should have the following criteria: (1) high electrical conductivity; (2) chemically stable in a highly acidic environment; (3) can take part in the reaction without undergoing any participation itself; and (4) electrochemically stable within the operational potential window [55]. The electrode can affect VRFB performance in various ways. For instance, electrochemical

reactivity influences the voltage efficiency, whereas chemical stability will determine the lifetime. Similarly, the pressure drop is affected by the electrode porosity.

The electrode in VRFB is mainly carbon-based material with thickness varies from several mm to few micrometres depending on the cell design. Different precursor materials have been used to produce carbon fibres, such as polyacrylonitrile (PAN) and rayon (cellulose based). Carbon precursor fibres (stabilized PAN or cellulose staple fibres) are needle-punched into a three-dimensional network of the porous structure (precursor felt). The manufacturing process involves various steps of stabilization and graphitization of felts. The felts are heated in an inert atmosphere (either nitrogen or argon) from 200°C to 2000°C using the two-step process. Thus, the properties of the electrodes vary depending on the graphitization temperature and heating rate steps [56]. PAN-based graphite felt is most extensively used as electrodes in VRFB due to its high surface area. In particular, graphite felts provide ample of redox reaction sites due to their high surface area, good stability and good electronic conduction. However, they have a sluggish electrochemical reaction and poor wettability in electrolyte due to its hydrophobic nature and poor reaction kinetics linked with oxidation and reduction of vanadium ions [57-59]. Therefore, various modification methods have been adopted to activate the surface of the graphite felt to improve VRFB performance.

2.5.4 Modification/Activation of Electrodes

Various techniques to modify graphite felt have been tried to enhance their performance. Modification of electrodes is expected to increase the electrochemical activity by increasing surface area, introducing oxygen-containing functional groups, increasing defects, etc. Various approaches of modifications are discussed in the following sections.

2.5.4.1 Thermal Treatment

Thermal treatment of the graphite felt is the most widely used technique for activation to create oxygen-containing functional groups. The initial study of the effect of thermal treatment on the carbon felt was carried out by Skyllas-Kazacos and coworkers. They investigated the carbon felt treated at different temperatures for a specific time of 30 hours. The carbon felt activated at 400°C for 30 hours (3mm thick, FMI Inc., USA) exhibited the

most significant increase in efficiency. The mass loss of 1.07% was observed for the graphite felt heated at 400°C for 30 hours while increasing the heating temperature to 500°C for 30 hours resulted in a mass loss of 11.02%. The improvement at 400°C for 30 hours was attributed to the increased oxygen-containing functional groups, such as C-OH and C=O, thus providing the active site for redox couple [60]. Similarly, Kim et al. [61] studied the influence of temperature on the carbon felt from 200°C to 600°C for 5 hours in the air and found that carbon felt surface was oxidized effectively beyond 400°C. Surface area and the ratio of O1s to C1s gradually increased with an increase in treatment temperature, increasing the oxygen-containing functional group formed on the surface of the carbon felt. Kim et al. [59] also studied electrochemical performance with structural change and found that the felt treated at 500°C for 5 hours exhibited improved energy efficiency and maintained even after 500 cycles.

Beside thermal modification in the air, thermal treatments in other atmospheric condition have also been investigated. Flox et al. [62] proposed thermal treatment of graphite felt based on NH_3:O_2 (1:1) at 400°C, 500°C and 600°C for various treatment time ranging from 6 hours to 36 hours. The highest electrochemical activity was observed to occur for the felt heated at 500°C for 5hr. The increase in graphite-like C-N bond with increasing treatment time is responsible for the high electrochemical activity. An increase in the electroactive surface area of more than 73% compared to the as-received felt was reported. Langer et al. [56] studied the effect of graphitization of carbon at the inert atmosphere at 1500°C and 2000°C, followed by thermal oxidation at different temperature. The correlation of oxygen-containing functional group with the electrochemical activity of V^{2+}/V^{3+} was investigated. The result showed that 5% of oxygen content significantly increased the electrochemical activity in negative half- cell. However, below 5% of oxygen content, V^{3+} reduction was significantly lowered.

2.5.4.2 Chemical treatment

Surface modification of carbon felt by acids, such as H_2SO_4, HNO_3 and H_3PO_4 has been widely studied. Sun et al. [63] performed the activation of graphite felt samples in a solution containing different concentrations of sulphuric acid, nitric acid and a mixture of both at various time. A decrease in cell resistivity resulting in increased energy efficiency

was observed for the electrode treated at concentrated sulphuric acid for 5 hours. The electrochemical activity of carbon felt increased with increasing concentration of sulphuric and nitric acid. Cell resistance increased with increasing treatment time above 5 hours. Improved performance for the electrode activated at concentrated H_2SO_4 for 5 hours was attributed to the formation of oxygen-containing the functional groups. Electrode treated with nitric acid and a mixture of H_2SO_4 and HNO_3, however, exhibited high cell resistance compared to sulphuric acid treatment with prolonged exposure. Surface analysis by XPS showed an increase in C-O and C=O functional group but with prolonged exposure surface chemisorbed oxygen decomposed with the release of CO and CO_2 resulting in the reduced activity. Li et al. [64] studied the carbon felt modification by initially treating the felt with 98% of sulphuric acid for 5 hours followed by thermal treatment at 450°C for 2 hours. The synergistic effect of acid and heat treatment increased the number of COOH functional group and surface area. Li et al. [65] observed excellent electrochemical properties after treating graphite felt with the mixed acid of HNO_3 and H_3PO_4 in the ratio of 3:1 for the different time at 80°C and attributed it to the increase in OH containing functional group. A different approach of hydrothermal ammoniate treatment of carbon felt was performed by Wu et al. [66]. The graphite felt was exposed to ammonia solution in an autoclave at 180°C for the different durations. Through ammonia treatment, the electrochemical activity of the graphite felt increased significantly for V^{4+}/V^{5+} redox reaction, resulting in improved efficiencies. The increase in electrochemical activity was attributed to surface-active nitrogen groups, resulting in increased charge transfer between vanadium ion and electrode

2.5.4.3 Catalyst functionalization

An alternative method to improve the reaction kinetics is to deposit a catalyst onto the surface of the electrode. This approach has already been reported in the early development of iron-chromium flow batteries by NASA in the 1970s [67]. While using catalyst-functionalized electrodes in a VRFB, several parameters should be taken into consideration, such as the susceptibility of hydrogen evolution in the negative half-cell, stability of the catalyst in the highly acidic environment and uniform distribution of the catalyst throughout the electrode thickness. Furthermore, the method used for deposition of the catalyst plays a crucial role since the catalyst need to bind effectively to the surface

of the carbon fibre in order to establish electronic contact. The catalyst should also show sufficient stability against dissolution or electrochemically induced ageing. The cost and availability of the catalyst also play important roles in the practical application.

Noble metals, such as Pt, Ir, Mn, Pd, and Au were deposited onto the carbon fibre to enhance the reaction kinetics. As expected, hydrogen evolution was prominent for Pt, Au and Pd decorated electrodes, whilst an Ir-coated electrode was found to exhibit the best electrochemical behaviour [68, 69]. Gonzalez et al. [70] modified GF with nanodispersed bismuth, and claimed excellent electrochemical performance on the positive half-cell with long-term stability. Similarly, electrodes containing metal oxides, such as Nb_2O_5, Mn_3O_4, and WO_3 were reported as promising materials for VRFB, particularly due to their low cost [71-73]. Nb_2O_5 was shown to have powerful catalytic activity toward both VRFB couples. In contrast, WO_3 has limited catalytic effect, whereas Mn_3O_4 is soluble under acidic condition.

Recently, transition metal nitrides and carbides have gained increasing attraction due to their stability and good electrical conductivity [74-77]. Wei et al. [78] bonded titanium carbide nanoparticles onto carbon paper by means of Nafion™ ionomer. Yang et al. [79] deposited titanium nitride nanoparticles onto carbon paper and reported better electrochemical activity and reversibility at the negative side of VRFB. Similarly, Wei et al. [80] employed titanium nanowire-decorated graphite felt (GF) in both half-cells, and found it exhibited higher electrolyte utilization and energy efficiency even at high current density.

2.5.4.4 Other Modification Techniques

Several other techniques of surface modification have been studied for improving the surface oxygen-containing functional groups. Komsiyska et al. [81] performed carbon felt treatment with plasma using different types of gas such as nitrogen, compressed air or argon at various flow rates and times. The results showed significant changes in the morphology for plasma treatment and destruction of the felt for prolonged exposure. Among the samples treated with different gases, nitrogen plasma treated felt showed the highest catalytic activities at the same conditions of operation [81]. Xu et al used

microwave treatment to activate the carbon felt at various times and temperatures. The microwave treatment resulted in the rough surface of the fibre with increased specific surface area. An increase in the oxygen-containing functional group was observed, which favoured the electrochemical reaction by providing more active sites for $V^{4+/}V^{5+}$ redox reaction [82].

Park et al. [59] proposed oxygen plasma and gamma-ray irradiation. The oxygen plasma treatment increased the surface area of the carbon felt with increased oxygen-containing functional group. However, for gamma-ray irradiation, an increase in surface area was negligible with no change in the morphology of carbon fibre being observed resulting in similar efficiencies as that of bare carbon felt. Kim et al. [83] proposed a new strategy of treating carbon felt by combining corona discharge and hydrogen peroxide. The proposed modification method was seen to be effective in producing oxygen-containing functional groups, which is due to the reaction of free radicals produced during corona discharge and its reaction with hydrogen peroxide. Schweiss et al. [84] studied the properties of carbon fibre with regard to varying nitrogen content and fibre crystallinity. The best voltage efficiency and electrolyte utilization were obtained for the glassy carbon like felt with around 2% of nitrogen content.

The table 2.2 summarizes the research progress related to the activation/modification of the electrode and selection of catalyst.

Table 2.2 Various method for the modification of the graphite felt.

Type	Modification method	Reagent or treatment condition
Graphite felt itself	Thermal	Air
	Thermal	NH3/O2:1/1
	Acid	H2SO4
	Acid	HNO_3
	Acid	(H_2SO_4/HNO_3:3/1)
	Thermal and Acid	H_2SO_4 + 450°C for 2hours
	Acid	(HNO_3/H_3PO_4: 3/1)
	Hydrothermal	NH_3
	Plasma	N_2, O_2
	Microwave	400°C, 15 min
Metal or metal oxide modification	metal impregnation	Pt, Ir, Mn, Pd, and Au
	Bi	electrodeposited
	Mn_3O_4	$((C_2H_3O_2)_2Mn{\cdot}4H_2O)$,

	hydrothermal
Nb_2O_5	1 M $(C_2H_3O_2)2Mn{\cdot}4H_2O$, 200 °C
WO_3	$(NH_4)6W_7O_{24}{\cdot}6H_2O$, 550 °C in N_2
TiN_3	0.2 M $TiCl_4$, hydrothermal and annealed (700-900°)

2.5.5 Interaction of Electrode Material with Vanadium Electrolyte

The V^{2+}/V^{3+} and VO_2^+/VO^{2+} redox reactions were first proposed by Sun et al. [55, 63]. The role of oxygen-containing functional groups at the surface of the carbon electrode and its interaction with the electrolyte was carried out. It was reported that C-OH functional group acts as the active site for the oxidation of VO^{2+}. Sun et al. proposed a three-step diagram, as shown in Figure 2.8 to explain the reaction mechanism for VO_2^+/VO^{2+} interaction with the electrode surface.

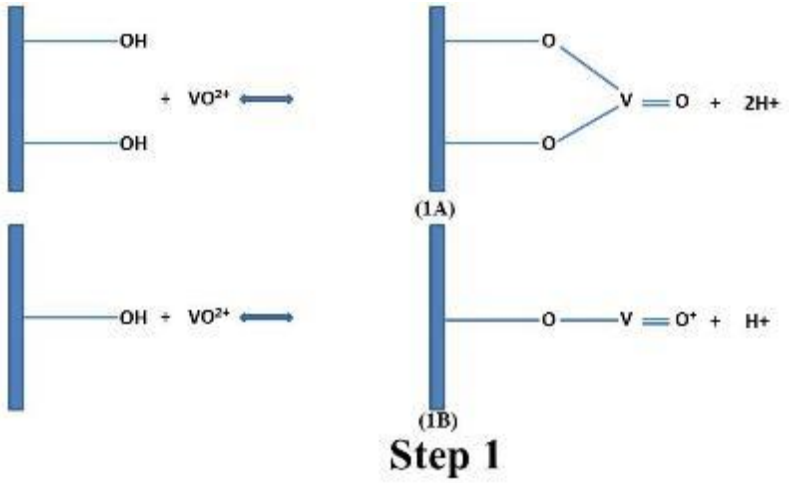

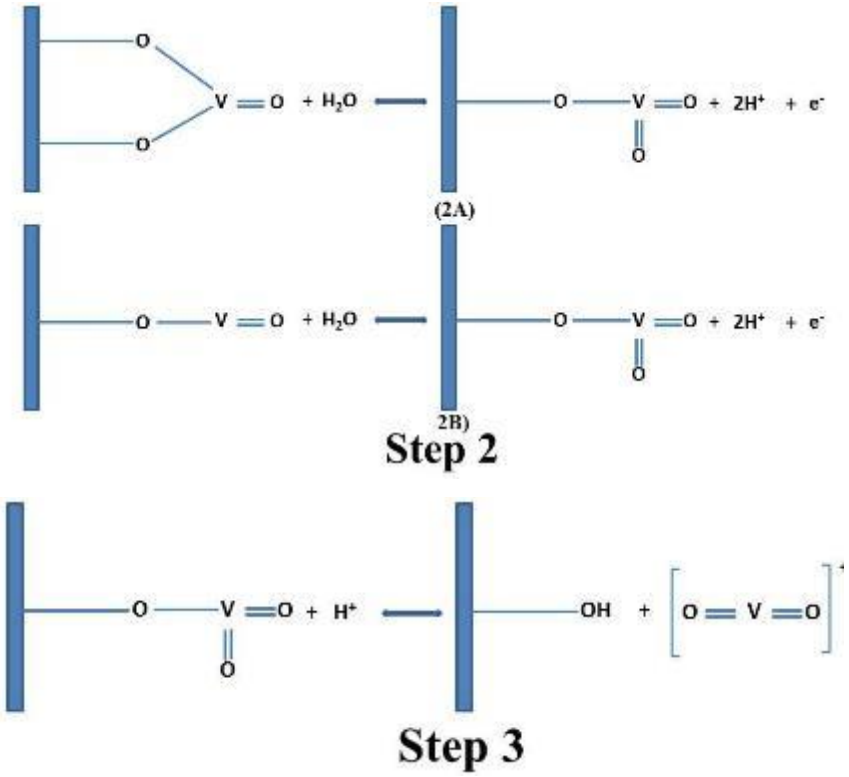

Figure 2.8 Schematic illustration of the redox reaction mechanism for the positive redox couple in VRFB.

In the first step, VO^{2+} diffuses from the bulk solution to the surface of the electrode. Ion exchange occurs between the VO^{2+} ions from the bulk of solution and H^+ ion from the phenolic groups on the carbon surface as depicted in step 1. This first step is followed by transfer of an electron from VO^{2+} to electrode along –C-O-V- bond and transfer of one oxygen atom from C-O functional group take place to form VO_2+. Finally, ion exchange takes place between VO_2+ and H+ from the solution and diffuses to the bulk solution. During discharge, the reaction occurs in the opposite direction but with more difficulty due to the bulky VO_2+ ion attached with C-O functional group [85]. It was suggested that the charging and discharging process at the positive electrode is associated with the transfer of oxygen atom, which is likely to be the rate-determining step.

Sun et al. [63] also proposed a reaction mechanism for the negative electrolyte. They also proposed a three-step mechanism similar to the positive electrolyte, as shown in Figure 2.9.

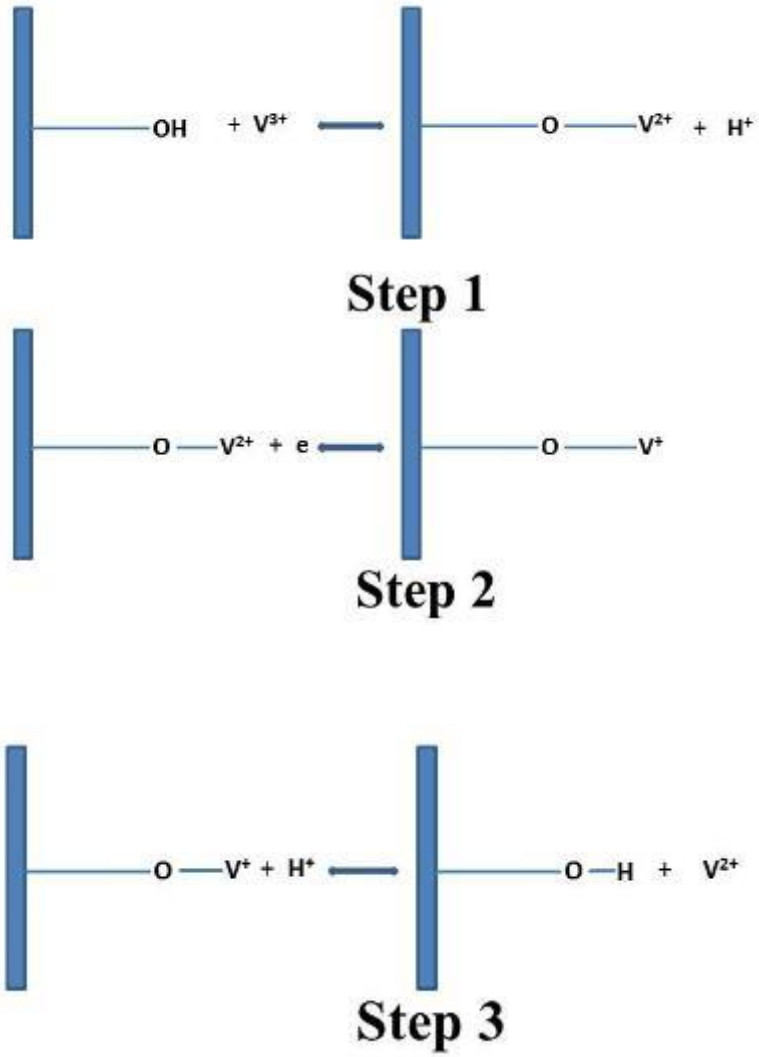

Figure 2.9 Schematic illustration of the redox reaction mechanism for negative redox couple.

During the charging process, V^{3+} diffusion takes place from the bulk solution to the surface of the electrode. Ion exchange occurs between the V^{3+} and the hydrogen from the phenol group in the first step. It is then followed by electron transfer from the electrode to V^{3+} along –C-O-V- bond forming V^{2+}. Finally, ion exchange occurs between V^{2+} and hydrogen from the solution and eventually diffusion occurs to the bulk solution. The discharge process is the reverse of the charging process. It is reported that although there is no oxygen transfer during the charging and discharging process, however, after ion exchange with the hydrogen of C-OH functional group, the transfer of electron might be facilitated.

Since the initial proposed mechanism from Skyllas-Kazacos research group, there have been ample attempts to further clarify the reaction mechanism for both redox couples. There have been numerous studies carried out in negative redox couples, and it is unanimously agreed that pre-treatment of the electrode enhances the electrochemical activity. Almost all studies concluded that surface functional groups, such as hydroxyl and carbonyl on carbon surface increase the wettability and catalyze the negative redox couple. However, for positive half-cell redox couple, various studies demonstrated that the oxygen-containing functional groups on the carbon surface impede or have no effect on the positive redox couple. Friedl et al. [86] investigated the positive redox couple reaction using multiwall carbon nanotube electrode decorated with different amounts of surface functional groups and found that the positive redox couple rate constant decreases with the amount of the surface functional groups. Schweiss et al. [87] similarly reported that excessive surface oxidation of PAN and rayon-based carbon felt induced a slightly detrimental effect on the positive redox couple. Langner et al. [88] conducted overpotential study by placing reference electrode at inlet and outlet of the cell, and observed no change in overpotential in the positive side between pristine and the thermally oxidized carbon felt.

2.5.6 Side Reactions at Electrodes

A number of undesirable reactions do occur in the VRFB along with the desired redox reactions. These undesirable reactions result in the evolution of gases (hydrogen, oxygen, carbon monoxide and carbon dioxide) and are parasitic, thus resulting in an irreversible capacity loss. The presence of gas reduces the liquid electrolyte in electrode resulting in the flow restriction, reduced active surface area and reduced charge and mass transfer coefficient [89]. In VRFB, the reduction potential of V^{3+} to V^{2+} occurs at 350 mV below the NHE (Normal hydrogen electrode), which allows simultaneous hydrogen evolution with vanadium reduction. With increasing SOC, the electrode is polarized more negatively with more hydrogen evolution. Hydrogen evolution occurs in the negative electrolyte of VRFB without any applied voltage. Sun et al. [90] related the hydrogen evolution rate with the electrochemical surface area for electrodes. Employing the high surface area (ECSA) the performance of VRFB increased significantly but the rate of side reactions increased

leading to decreased capacity. Liu et al. [91] investigated the corrosion of graphite felt and reported the evolution of CO and CO_2 on the graphite electrode simultaneously with the onset potential of 1.6 V, while oxygen evolution needs higher potential above 1.8 V.

2.6 In-situ Study of VRFB

Numerous studies of vanadium redox flow batteries (VRFBs) have been dedicated to electrode modification [59, 60, 63, 84, 92], higher stability of electrolyte [32, 36, 93, 94], membrane [95, 96] and cell architecture [97-99] to improve the overall cell performance. In order to evaluate the overall VRFB cell performance, ex-situ characterization techniques are usually used. This black box approach, however, is unable to provide any deeper understanding of the changes that occur within the cell during the operation. Therefore, the in-situ approach could be of great importance due to the availability of real-time data and hence can reflect VRFB performance during cell operation.

2.6.1 Spatially Resolved Current or Voltage Mapping

Segmented cell is a unique tool to investigate the local behaviour through the analysis of local voltage or current. This approach has been extensively used in PEM fuel cells [100-103] to measure the current distribution, however, this type of study is rarely performed in VRFB.

In term of cell architecture and flow configuration, the segmented cell is similar to the normal cell. However, instead of a two-terminal, segmented cell has multiple terminals, and each terminal can be independently controlled. The electrode and/or current collector is divided into a number of segments, and each of the divided segments is insulated from each other. Therefore, it is possible to independently control the charging and discharging of each individual segment. Hence, the resistance, current and voltage can be monitored independently in each segment. The most frequently used techniques to monitor each segment can be classified into three types: resistor network, Hall effect sensors and printed circuit board (PCB) types. These techniques require the segmentation of either current collector (CC), bipolar plate or both. In the resistor network approach, the shunt resistor is connected in series with each segment and the current density is obtained from the voltage drop across the respective shunt resistor [104]. PCB technique employs thin, flat circuit

board CCs that are placed between the flow field and end plate. This cell architecture ensures a low contact resistance between the PCB and the current collector. Hall effect sensor technique involves the connection of one Hall sensor to each segment. The magnetic flux density passing through each sensor determines the voltage of the sensor, which is proportional to the current [105].

There are only a few studies dedicated to the application of segmented cells in RFBs [106-108]. Hsieh et al. [106] investigated two different cell designs (A and B) of the segmented flow cell with an active area of 100 cm^2. The cell was divided into 25 segments and a shunt resistor was used to measure the local current or voltage of each segment. In the first design (A), only the current collector was segmented without the segmentation of graphite plate (5 mm thick), whereas in their second design (B), connecting cables were directly embedded into the segmented graphite collector (10 mm thick). For type (A), non-uniform compression and contact resistance variation between the segments produced noticeable effects on the distribution of the current. Similarly, due to higher contact resistance and use of the bipolar plate, the application of design (B) resulted in low discharge capacity, voltage efficiency and poor distribution. Clement et al. [107] implemented printed circuit board technique and segmented a 9 cm^2 cell into 36 segments. The cell used bipolar plates with serpentine flow Ffield and multiple layers of thin electrodes. Their finding suggested that the current distribution reflected the electrolyte concentration gradient across the active cell area. Their study, however, was performed using thin carbon paper electrodes and a different cell architecture than in conventional flow batteries.

One of the important differences between the fuel cell type cells and a conventional VRFB is the direction of convection of the reactants. In the fuel cell type designs, forced convection in through-plane direction dominates, whereas in conventional VRFBs convective transport preferably takes place in the in-plane direction. Segmented cell studies using the conventional design of VRFBs (flat plate and porous carbon felt electrode) have only been reported by Hsieh et al. [106] and Bhattarai et al. [108, 109]. Overall, the general procedure to conduct the segmented cell study is presented in Figure 2.10.

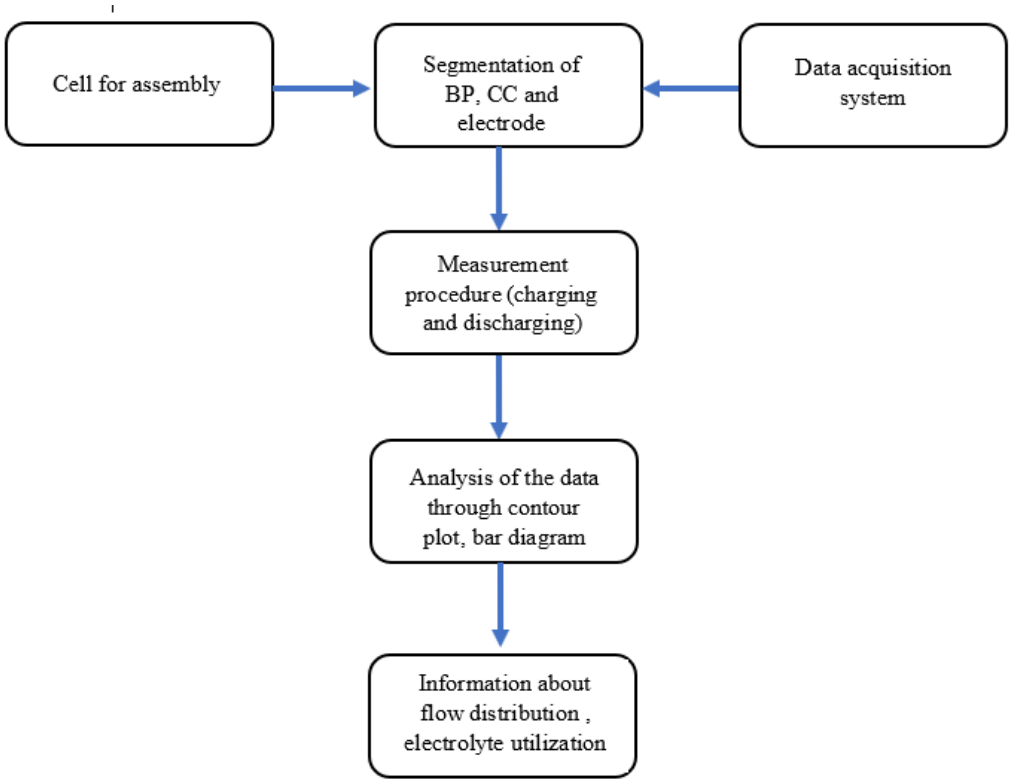

Figure 2.10 General scheme of segmented cell study

As stated earlier, the segmented cell technique has not been fully explored in redox flow batteries. One of the problems encountered for segmented cell study is the uneven compression of the graphite felt electrode and bipolar plate at the interface. This results in uneven contact resistance and thus may cause the cell to suffer from the lateral flow of current from one segment to another, leading to misinterpretation of data acquired from current-voltage distribution. This might be a probable reason that the segmented cell study is rare in flow batteries.

2.6.2 Use of Reference Electrode

One of the best ways to acquire information about the losses occurring in VRFB is to design the geometry of the cell to make it suitable for the reference electrode configuration. This was first realized in the fuel cell, where the fine reference wire electrode is sandwiched between the two membranes [110] or is attached to a region within polymer electrolyte that extends beyond the cell [111]. In VRFB, Aaron et al. [112] implemented the dynamic

hydrogen electrode (DHE) as a reference electrode for a study on the kinetics of the negative and positive side. The study reported greater kinetic polarization at the negative electrode compared to the positive electrode. Similarly, Yassar et al. [113] investigated the potential distribution in through-plane direction by stacking the electrodes and inserting the probes in between and placing the DHE between the two membranes. The study revealed the potential distribution as a function of discharge current density and predicted the lowest potential region close to the flow frame.

Reference electrode measurements were used to compare the performance of pristine and thermally oxidized carbon felts at positive half and negative half-cell. Langner et al. [88] placed the Ag/AgCl reference electrodes at the inlet and outlet tubings of the cell. Their result showed that the performance gain of the thermally oxidized carbon felt is mostly related to the negative half-cell. Similarly, Ventosa et al. [114] inserted the silver wire as a reference electrode between the two membranes and studied the ammoxidized graphite felts. They demonstrated a slower electrochemical reaction in VO^{2+}/VO_2^{+} than that of V^{2+}/V^{3+}. The half-cell study could be extended to investigate the change in overpotential with the change in electrode type, electrolyte flow rate, state of charge of the electrolyte and concentration of the electrolyte. Moreover, the tool can be used to investigate the potential in each half-cell at various operating condition and different material types.

2.7 Scope of This Study in the Context of Literature

The research on VRFB is primarily focused on four areas, namely electrode, electrolyte, membrane, stack design and optimization. This PhD research aims to work on electrode modification and carry out optimization to improve VRFB performance as well as establish a proper in-situ technique to investigate electrolyte distribution in the cell. The research and its scope are designed in collaboration with the industrial partner, SGL Carbon. The electrode has been supplied by the industrial partner throughout the research. Commercial anion exchange membrane (FAP 450) from Fumatech GmbH, Germany and standard electrolyte with concentration 1.6 M $V^{+3.5}$ in total 4 M sulfate (GFE, Germany) are used in all experiments.

Electrode modification is one of the major research areas in the VRFB. Most of this modification is focused on thermal oxidation treatment and metal doping on electrode as part of attempts to improve VRFB performance. Besides, proper monitoring technique that allows the collection of real-time measurement data throughout the operation is essential to enable correct evaluation of cell performance. Hence, this PhD work focuses on the optimization of the thermally oxidized electrode by varying temperature and treatment times and electrode doping with a low-cost catalyst. Further, this PhD study will also include the development of suitable methods to study the in-situ behaviour of the cell using a segmented cell and reference electrode insertion approach.

The Figure 3.10 presents the overall logic line or scope of the PhD work.

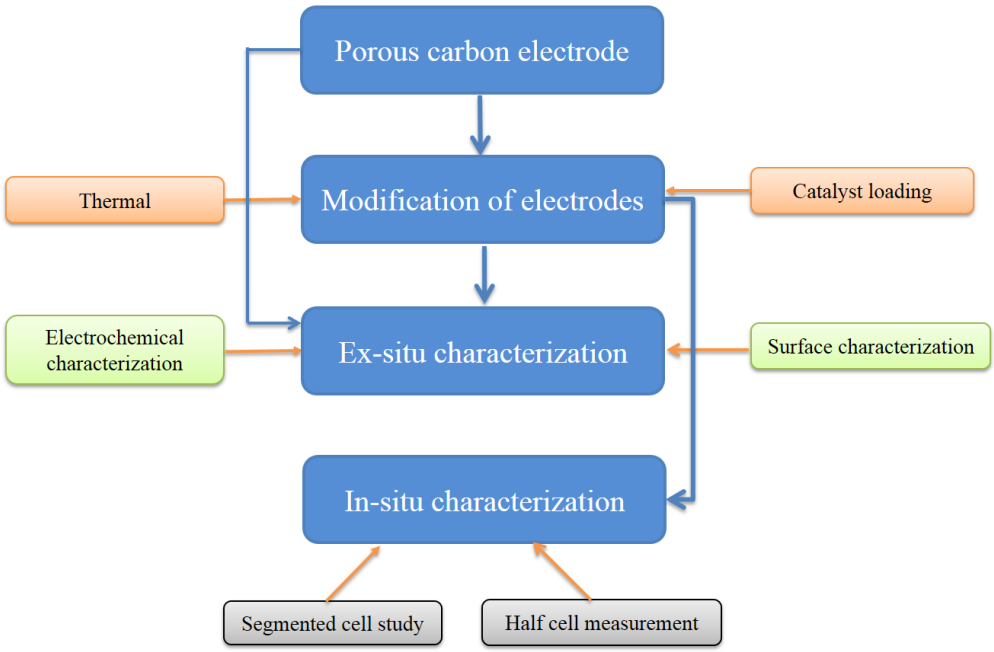

Figure 2.11 Scope of the PhD work.

References

[1] K.R. Bullock, *Journal of power sources*, **1994**, 51, 1-17.

[2] C.D. Parker, *Journal of Power Sources*, **2001**, 100, 18-28.

[3] Z. Wen, J. Cao, Z. Gu, X. Xu, F. Zhang, Z. Lin, *Solid State Ionics*, **2008**, 179, 1697-1701.

[4] A. Ritchie, W. Howard, *Journal of Power Sources*, **2006**, 162, 809-812.

[5] J.S. Lee, S. Tai Kim, R. Cao, N.S. Choi, M. Liu, K.T. Lee, J. Cho, *Advanced Energy Materials*, **2011**,1, 34-50.

[6] M. Skyllas-Kazacos, M. Chakrabarti, S. Hajimolana, F. Mjalli, M. Saleem, *Journal of The Electrochemical Society*, **2011**,158, R55-R79.

[7] A. Parasuraman, T.M. Lim, C. Menictas, M. Skyllas-Kazacos, *Electrochimica Acta*, **2013**, 101, 27-40.

[8] P. Alotto, M. Guarnieri, F. Moro, *Renewable and Sustainable Energy Reviews*, **2014**, 29, 325-335.

[9] M. Rychcik, M. Skyllas-Kazacos, *Journal of Power Sources*, **1988**, 22, 59-67.

[10] G. Kear, A.A. Shah, F.C. Walsh, *International Journal of Energy Research*, **2012**, 36, 1105-1120.

[11] A. Poullikkas, *Renewable and Sustainable energy reviews*, **2013**, 27, 778-788.

[12] Y. Wen, Y. Xu, J. Cheng, G. Cao, Y. Yang, *Electrochimica Acta*, **2013**, 96, 268-273.

[13] F. Rahman, M. Skyllas-Kazacos, *Journal of Power Sources*, **2009**, 189, 1212-1219.

[14] S. Kim, E. Thomsen, G. Xia, Z. Nie, J. Bao, K. Recknagle, W. Wang, V. Viswanathan, Q. Luo, X. Wei, *Journal of Power Sources*, **2013**, 237, 300-309.

[15] B. Schwenzer, J. Zhang, S. Kim, L. Li, J. Liu, Z. Yang, *ChemSusChem*, **2011**, 4 1388-1406.

[16] C. Blanc, Christian, R. Alfred , *In Tech*, **2010**.

[17] C. Blanc, *Modeling of a vanadium redox flow battery electricity storage system*, PhD thesis, **2009**.

[18] A.J. Bard, R. Parsons, J. Jordan, *CRC press*, **1985**.

[19] A.J. Bard, L.R. Faulkner, *Electrochemical Methods*, **2001,2,** 482.

[20] P.M. Monk, Fundamentals of electroanalytical chemistry, John Wiley & Sons, 2008.

[21] D. Aaron, Z. Tang, A.B. Papandrew, T.A. Zawodzinski, *Journal of Applied Electrochemistry*, **2011**, 1175.

[22] K.J. Yoon, W. Huang, G. Ye, S. Gopalan, U.B. Pal, D.A. Seccombe, *Journal of the Electrochemical Society*, **2007**, 154, B389-B395.

[23] M.M. Mench, *John Wiley & Sons*, **2008**.

[24] J. Sun, D. Shi, H. Zhong, X. Li, H. Zhang, *Journal of Power Sources*, **2015**, 294, 562-568.

[25] F. Xing, H. Zhang, X. Ma, *Journal of Power Sources*, **2011**, 196, 10753-10757.

[26] Y. Wen, H. Zhang, P. Qian, P. Zhao, H. Zhou, B. Yi, *Acta physico-chimica Sinica*, **2006**, 22, 403-408.

[27] F. Rahman, M. Skyllas-Kazacos, *Journal of Power Sources*, **1998**,72, 105-110.

[28] M. Skyllas-Kazacos, C. Menictas, M. Kazacos, *Journal of the Electrochemical Society*, **1996**, 143, L86-L88.

[29] X. Lu, *Electrochimica acta*, **2001**, 46, 4281-4287.

[30] M. Kazacos, M. Cheng, M. Skyllas-Kazacos, *Journal of Applied electrochemistry*, 20 **1990**, 20, 463-467.

[31] F. Rahman, M. Skyllas-Kazacos, *Journal of Power Sources*, **2017**, 340, 139-149.

[32] G. Wang, J. Chen, X. Wang, J. Tian, H. Kang, X. Zhu, Y. Zhang, X. Liu, R. Wang, *Journal of Energy Chemistry*, **2014**, 23, 73-81.

[33] G. Wang, J. Zhang, J. Zhang, J. Chen, S. Zhu, X. Liu, R. Wang, *Journal of Electroanalytical Chemistry*, **2016,** 768, 62-71.

[34] G. Wang, J. Chen, X. Wang, J. Tian, H. Kang, X. Zhu, Y. Zhang, X. Liu, R. Wang, Journal of Electroanalytical Chemistry, **2013**, 709, 31-38.

[35] M. Kazacos, M.S. Kazacos, *High energy density vanadium electrolyte solution* , in Google Patents, **2006**.

[36] Y. Lei, S.-q. Liu, C. Gao, X.-x. Liang, Z.-x. He, Y.-h. Deng, Z. He, *Journal of The Electrochemical Society*, **2013**, 160, A722-A727.

[37] S. Roe, C. Menictas, M. Skyllas-Kazacos, *Journal of The Electrochemical Society*, **2016**, 163, A5023-A5028.

[38] L. Li, S. Kim, W. Wang, M. Vijayakumar, Z. Nie, B. Chen, J. Zhang, G. Xia, J. Hu, G. Graff, *Advanced Energy Materials*, **2011**, 1, 394-400.

[39] T. Sukkar, M. Skyllas-Kazacos, *Journal of Membrane Science*, **2003**, 222, 249-264.

[40] T. Mohammadi, M. Skyllas-Kazacos, *Journal of Membrane Science*, **1995**, 98, 77-87.

[41] S. Jeong, L.-H. Kim, Y. Kwon, S. Kim, *Korean Journal of Chemical Engineering*, **2014**, 31, 2081-2087.

[42] H. Prifti, A. Parasuraman, S. Winardi, T.M. Lim, M. Skyllas-Kazacos, *Membranes*, **2012, 2,** 275-306.

[43] M.W. Verbrugge, R.F. Hill, *Journal of The Electrochemical Society*, **1990**, 137, 893-899.

[44] A. Lehmani, P. Turq, M. Périé, J. Périé, J.-P. Simonin, Journal of Electroanalytical Chemistry, **1997**, 428, 81-89.

[45] Y. Tanaka, Ion exchange membranes: fundamentals and applications, Elsevier, **2015**.

[46] B.S. Pivovar, W.H. Smyrl, E.L. Cussler, *Journal of the Electrochemical Society*, **2005**, 152, A53-A60.

[47] C. Jia, J. Liu, C. Yan, *Journal of Power Sources*, **2010**, 195, 4380-4383.

[48] K.S. Yoon, J.Y. Lee, T.H. Kim, D.M. Yu, D.W. Seo, S.-K. Hong, Y.T. Hong, *Journal of Industrial and Engineering Chemistry*, **2014**, 20, 2310-2316.

[49] M. Ulaganathan, V. Aravindan, Q. Yan, S. Madhavi, M. Skyllas-Kazacos, T.M. Lim, *Advanced Materials Interfaces*, **2016**, 3,1.

[50] M.S. Cha, H.Y. Jeong, H.Y. Shin, S.H. Hong, T.-H. Kim, S.-G. Oh, J.Y. Lee, Y.T. Hong, *Journal of Power Sources*, **2017**, 363, 78-86.

[51] J. Qiu, M. Li, J. Ni, M. Zhai, J. Peng, L. Xu, H. Zhou, J. Li, G. Wei, *Journal of Membrane Science*, **2007**, 297, 174-180.

[52] T. Franken, *Membrane Technology*, **2000**, 8-11.

[53] B. Arjun, S. Rüdiger, W. Adam, G.S. Günther, W. Nyunt, C.G. Purna, D.N. Tam, O.O. Moe, H. Huey Hoon, *International flow battery forum*, 2017.

[54] A. Pellegri, B.M. Broman, *World Intellectual Property Organization, WO99,* **1999**, 39397.

[55] K.J. Kim, M.-S. Park, Y.-J. Kim, J.H. Kim, S.X. Dou, M. Skyllas-Kazacos, *Journal of Materials Chemistry A*, **2015**,3, 16913-16933.

[56] J. Langner, M. Bruns, D. Dixon, A. Nefedov, C. Wöll, F. Scheiba, H. Ehrenberg, C. Roth, J. Melke, *Journal of Power Sources*, **2016**,321, 210-218.

[57] P. Leung, X. Li, C.P. De León, L. Berlouis, C.J. Low, F.C. Walsh, *Rsc Advances*, **2012**, 2, 10125-10156.

[58] J. Yang, Y. Liu, S. Liu, L. Li, C. Zhang, T. Liu, *Materials Chemistry Frontiers*, **2017**,1, 251-268.

[59] K.J. Kim, Y.-J. Kim, J.-H. Kim, M.-S. Park, *Materials Chemistry and Physics*, (**2011**, 131, 547-553.

[60] B. Sun, M. Skyllas-Kazacos, *Electrochimica Acta*, **1992**, 37, 1253-1260.

[61] K.J. Kim, M.-S. Park, J.Y. Kim, Y.-J. Kim, *The Electrochemical Society*, **2010**, 405-405.

[62] C. Flox, J. Rubio-García, M. Skoumal, T. Andreu, J.R. Morante, *Carbon*, **2013**, 60, 280-288.

[63] B. Sun, M. Skyllas-Kazacos, *Electrochimica Acta*, **1992**, 37, 2459-2465.

[64] X.-g. Li, K.-l. Huang, S.-q. Liu, L.-q. Chen, *Journal of Central South University of Technology*, **2007**,14, 51-56.

[65] W.W. Li, Y.Q. Chu, C.A. Ma, *Advanced Materials Research, Trans Tech Publ*, **2014**, pp. 471-475.

[66] T. Wu, K. Huang, S. Liu, S. Zhuang, D. Fang, S. Li, D. Lu, A. Su, *Journal of Solid State Electrochemistry*, **2012**, 16, 579-585.

[67] L.H. Thaller, Electrically rechargeable redox flow cell, **1976**.

[68] B. Sun, M. Skyllas-Kazakos, *Electrochimica Acta*, **1991**, 36, 513-517.

[69] W. Wang, X. Wang, *Electrochimica Acta*, **2007**, 52, 6755-6762.

[70] Z. González, A. Sánchez, C. Blanco, M. Granda, R. Menéndez, R. Santamaría, *Electrochemistry Communications*, **2011**, 13, 1379-1382.

[71] B. Li, M. Gu, Z. Nie, X. Wei, C. Wang, V. Sprenkle, W. Wang, *Nano Letters*, **2013**, 14, 158-165.

[72] K.J. Kim, M.-S. Park, J.-H. Kim, U. Hwang, N.J. Lee, G. Jeong, Y.-J. Kim, *Chemical Communications*, **2012, 48**, 5455-5457.

[73] C. Yao, H. Zhang, T. Liu, X. Li, Z. Liu, *Journal of Power Sources*, **2012**, 218, 455-461.

[74] Y. Dong, Y. Wu, M. Liu, J. Li, *ChemSusChem*, **2013**, 6 2016-2021.

[75] T.M. Keller, M. Laskoski, A.P. Saab, S.B. Qadri, M. Kolel-Veetil, *The Journal of Physical Chemistry C*, **2014**, 118, 30153-30161.

[76] Z. Jin, P. Li, D. Xiao, *Scientific reports*, **2014**, 4.

[77] H. Wang, Y. Zhang, H. Ang, Y. Zhang, H.T. Tan, Y. Zhang, Y. Guo, J.B. Franklin, X.L. Wu, M. Srinivasan, *Advanced Functional Materials*, **2016**, 26, 3082-3093.

[78] L. Wei, T. Zhao, L. Zeng, X. Zhou, Y. Zeng, *Energy Technology*, **2016**, 4, 990-996.

[79] C. Yang, H. Wang, S. Lu, C. Wu, Y. Liu, Q. Tan, D. Liang, Y. Xiang, *Electrochimica Acta*, **2015**, 182, 834-840.

[80] L. Wei, T. Zhao, L. Zeng, Y. Zeng, H. Jiang, *Journal of Power Sources*, **2017**, 341, 318-326.

[81] E.-M. Hammer, B. Berger, L. Komsiyska, *International Journal of Renewable Energy Development*, **2014**, 3, 7.

[82] X. Wu, H. Xu, P. Xu, Y. Shen, L. Lu, J. Shi, J. Fu, H. Zhao, *Journal of power sources*, **2014**, 263, 104-109.

[83] K.J. Kim, S.-W. Lee, T. Yim, J.-G. Kim, J.W. Choi, J.H. Kim, M.-S. Park, Y.-J. Kim, *Scientific reports*, **2014**, 4.

[84] R. Schweiss, *Journal of Power Sources*, **2015**, 278, 308-313.

[85] M. Rychcik, M. Skyllas-Kazacos, *Journal of Power Sources*, **1987**, 19, 45-54.

[86] J. Friedl, C.M. Bauer, A. Rinaldi, U. Stimming, *Carbon*, **2013**, 63, 228-239.

[87] R. Schweiss, C. Meiser, F.W.T. Goh, *ChemElectroChem*, **2017**, 4, 1969-1974.

[88] J. Langner, J. Melke, H. Ehrenberg, C. Roth, *ECS Transactions*, **2014**, 58, 1-7.

[89] A. Shah, H. Al-Fetlawi, F. Walsh, *Electrochimica Acta*, **2010**, 55, 1125-1139.

[90] C.-N. Sun, F.M. Delnick, L. Baggetto, G.M. Veith, T.A. Zawodzinski, *Journal of Power Sources*, **2014**, 248, 560-564.

[91] H. Liu, Q. Xu, C. Yan, *Electrochemistry Communications*, **2013**, 28, 58-62.

[92] P.C. Ghimire, R. Schweiss, G.G. Scherer, N. Wai, T.M. Lim, A. Bhattarai, T.D. Nguyen, Q. Yan, *Journal of Materials Chemistry A*, **2018**, 6, 15, 6625-6632.

[93] X. Wu, S. Liu, N. Wang, S. Peng, Z. He, *Electrochimica Acta*, **2012**,78 475-482.

[94] T.D. Nguyen, A. Whitehead, G.G. Scherer, N. Wai, M.O. Oo, A. Bhattarai, G.P. Chandra, Z.J. Xu, *Journal of Power Sources*, **2016**, 334, 94-103.

[95] X. Li, H. Zhang, Z. Mai, H. Zhang, I. Vankelecom, *Energy & Environmental Science*, **2011**, 4, 1147-1160.

[96] D. Chen, M.A. Hickner, E. Agar, E.C. Kumbur, *Electrochemistry Communications*, **2013**, 26, 37-40.

[97] T.J. Latha, S. Jayanti, *Journal of Applied Electrochemistry*, **2014**, 44, 995-1006.

[98] D. Aaron, Q. Liu, Z. Tang, G. Grim, A. Papandrew, A. Turhan, T. Zawodzinski, M. Mench, *Journal of Power Sources*, **2012**, 206, 450-453.

[99] A. Bhattarai, N. Wai, R. Schweiss, A. Whitehead, T.M. Lim, H.H. Hng, *Journal of Power Sources*, **2017**, 341, 83-90.

[100] C. Hartnig, I. Manke, N. Kardjilov, A. Hilger, M. Grünerbel, J. Kaczerowski, J. Banhart, W. Lehnert, *Journal of Power Sources*, **2008**, 176, 452-459.

[101] N. Zamel, R. Hanke-Rauschenbach, S. Kirsch, A. Bhattarai, D. Gerteisen, *International Journal of Hydrogen Energy*, **2013**, 38, 15318-15327.

[102] S. Cleghorn, C. Derouin, M. Wilson, S. Gottesfeld, *Journal of Applied Electrochemistry*, **1998**, 28, 663-672.

[103] I. Schneider, S. Von Dahlen, A. Wokaun, G. Scherer, Journal of The Electrochemical Society, **2010**, 157, B338-B341.

[104] C. Kalyvas, A. Kucernak, D. Brett, G. Hinds, S. Atkins, N. Brandon, *Energy and Environment*, **2014**, 3, 254-275.

[105] L.C. Pérez, L. Brandão, J.M. Sousa, A. Mendes, *Renewable and Sustainable Energy Reviews*, **2011**, 15, 169-185.

[106] W.-Y. Hsieh, C.-H. Leu, C.-H. Wu, Y.-S. Chen, *Journal of Power Sources*, **2014**, 271, 245-251.

[107] J.T. Clement, D.S. Aaron, M.M. Mench, *Journal of The Electrochemical Society*, **2016**, 163, A5220-A5228.

[108] A. Bhattarai, N. Wai, R. Schweiss, A. Whitehead, G.G. Scherer, P.C. Ghimire, T.D. Nguyen, H.H. Hng, *Journal of Power Sources*, **2017**, 360, 443-452.

[109] P.C. Ghimire, A. Bhattarai, R. Schweiss, G.G. Scherer, N. Wai, Q. Yan, *Applied Energy*, **2018**, 230, 974-982.

[110] F.N. Büchi, G.G. Scherer, *Journal of the Electrochemical Society*, **2001**, 148, A183-A188.

[111] A. Küver, I. Vogel, W. Vielstich, *Journal of power sources*, **1994**, 52, 77-80.

[112] D. Aaron, C.-N. Sun, M. Bright, A.B. Papandrew, M.M. Mench, T.A. Zawodzinski, *ECS Electrochemistry Letters*, **2013**, 2, A29-A31.

[113] Y.A. Gandomi, D. Aaron, T. Zawodzinski, M. Mench, *Journal of The Electrochemical Society*, **2016**, 163, A5188-A5201.

[114] E. Ventosa, M. Skoumal, F.J. Vázquez, C. Flox, J.R. Morante, *Journal of Power Sources*, **2014**, 271,556-560.

Chapter 3

Experimental Methodology

This chapter presents the material, experimental design and procedure employed in this study. The methods used are explained and the rationale behind using the specific technique is elucidated. The first section reveals the idea of electrode selection, the description of the thermal oxidation method and the technique to synthesize the titanium carbide (TiC) catalyst. The second section includes the method applied to analyze the physical and electrochemical characterization of pristine and modified electrodes. It also includes the description of the VRFB single cell for the performance evaluation. This is then followed by the description of segmented cell components, its hardware system and measurement procedure for the in-situ performance measurement. The experimental setup and measurement procedure for the optimization of the compression of the electrode is also described in detail. Finally, the measurement setup and procedure for the half-cell measurement is explained.

3.1 Electrode Selection

The graphite felt manufactured by SGL carbon (SIGRACELL GFD 4.6 EA) was used throughout the research. This material is graphitized in argon at temperatures more than 2000°C. Therefore, there is always a probability that the carbon surface area may vary due to synthesizing conditions and precursor. To investigate the reproducibility of the electrode used during the experiment, three different electrodes produced from three different batches were obtained for comparison study where these electrodes were evaluated through physical, electrochemical, spectroscopic and single cell characterization.

3.2 Thermal Modification and Optimization of the Electrodes

Graphitized PAN felts (SIGRACELL GFD 4.6 EA) produced on the same batch, received from SGL Carbon GmbH, Meitingen, Germany were used as the electrodes. The samples were washed with ethanol and deionized water, and dried under vaccum. The electrodes were thermally oxidized under air in a furnace (Nabertherm GmbH). The electrodes were configured inside the furnace in such a way that they were lying freely inside the furnace with the help of ceramics bed while being oxidized. The samples were heated at a rate of 5°C min^{-1} until the target temperature was reached and the samples were then held at the target temperature for a given period, followed by cooling rate at a 5°C min^{-1} until it reached the room temperature. For electrode treated at 750°C, the furnace was heated to 750°C, afterwards, the electrode was inserted into the furnace for a given period, followed by unleashing of the electrode to ambience atmosphere. For each experiment, the pre-treatment of the electrode was performed right before the experiment was carried out. The mass loss due to oxidation was calculated at each temperature by weighing the mass of the electrode before and after the thermal treatment.

3.3 Titanium Carbide (TiC) Decoration of the Graphite Felt

A precursor solution was obtained by mixing TiF_4 and de-ionised (DI) water. A sheet of GF was sonicated in ethanol, washed with DI water and finally vacuum-dried at 80°C before being immersed into the precursor solution. The GF was then transferred to a Teflon-lined autoclave containing the precursor solution, and the hydrothermal reaction was maintained at 180°C for 14 h. The as-prepared samples were freeze-dried overnight

followed by vacuum drying at 60°C for 14 h. The GF containing TiO_2 nanoparticles was subsequently transferred to a tube furnace for annealing in an Argon atmosphere. The temperature was ramped up from ambient temperature to 1250°C at a heating rate of 5°C min^{-1} and was kept at 1250°C for 5 h. After cooling, TiC particles could be readily observed on the carbon fibre surface.

3.4 Characterization of Electrodes

The physical, electrochemical, spectroscopic and single cell characterization was carried out to evaluate the performance of the VRFB cell. Each characterization technique is described in detail.

3.4.1 Morphological Characterization

3.4.1.1 Field Emission Scanning Electron Microscopy (FESEM)

FESEM was used to visualize the topography of the carbon surface. Particularly, the high magnification FESEM image was used to differentiate the surface morphology between the modified and as-received carbon fibre. In addition, FESEM assisted in determining the uniformity and size of the catalyst deposited onto the electrode which is highly important. FESEM is a microscope that works with electron instead of light. Field emission source emits electrons and the ejected electrons are accelerated in a high electric field gradient. In the high vacuum column, these primary electrons produce a narrow scan with the aid of lenses. These primary electrons bombard the object, resulting in the emission of secondary electrons. The detector catches the secondary electron and the electrical signal is produced, which is then transformed into video scan-image [1, 2]. The morphology of electrodes was characterized by field emission scanning electron microscopy, FESEM (JEOL, Model JSM-7600F) with an acceleration voltage of 5 kV.

3.4.1.2 High-resolution Transmission Electron Microscopy (HRTEM)

HRTEM is a specialized TEM that has highly specialized imaging mode. TEM works based on the electron diffraction principle. It is the best tool for the visualization of the structure, defect location and identification. An electron beam is focused on the object through which the beam is transmitted. The transmitted beam is focused by the objective

lens into an image. This is then enlarged by the means of enlarging lenses and a projector lens. The direct imaging on the atomic scale is possible via HRTEM [3, 4]. In this study, with the aid of HRTEM, the particle distribution, its size, lattice spacing and the structure were determined. High-resolution transmission electron microscopy (HRTEM) images were obtained using a JEOL, JEM-2100 system, operating at an acceleration voltage of 200 kV.

3.4.2 Structural Characterization

3.4.2.1 X-ray Diffraction (XRD)

X-ray diffraction is a widely used technique for the identification of crystallinity or determination of the crystal structure. In XRD, the X-ray beam is projected to the surface and interference effect between an atom of crystal and X-ray is observed. XRD is used to determine the phase identification after electrode modification. In this study, XRD was mostly used for the catalyst-modified electrodes, as changes are much prominent in these electrodes. The structural defects induced by the modification can be observed by comparing the XRD patterns or diffraction peaks. X-ray diffraction (XRD) patterns were obtained by using a Shimadzu (XRD-6000 setup) X-ray diffractometer with Cu-Kα radiation ($\lambda = 1.5406$ Å) operated at 40 kV and 30 mA.

3.4.2.2 Raman Spectroscopy

Raman spectroscopy is a nondestructive technique used to provide information about the changes that occur on the surface. In the field of carbon, it provides information about the graphitization degree of the graphitic material [5, 6]. Raman spectroscopy measures the molecular vibration induced by the monochromatic light. Latest Raman spectroscopy utilizes a laser source. The laser light interaction with the object results in a combination of three phenomena, namely: (a) light passes without any interaction or (b) light leaves the sample with the same frequency as it entered (elastic scattering or Rayleigh scattering) or (c) the light is scattered idealistically by molecules in the sample (Raman scattering) [2]. Most of the scattered light is Rayleigh-type and does not provide useful information. However, a very tiny fraction of the light is scattered inelastically and provides useful information.

The penetration depth of the 488 nm laser is about (10-50) nanometer, as exact confocal penetration depends on the instrumental parameter, sample parameter and interaction of the sample with optics [7].

The D and G bands measured are used to characterize the graphite samples. First order Raman mode, also known as G band (Graphitic) appears around 1585 cm^{-1} corresponding to sp^2 carbon atoms. Similarly, the D band (disordered) provides information about the amorphous carbon and defects originating from a second order scattering which appears around 1355 cm^{-1} [8]. The change in the structural ordering and crystallinity is analysed by the intensity ratio between the intensity of D band to G band as shown in Figure 3.1.

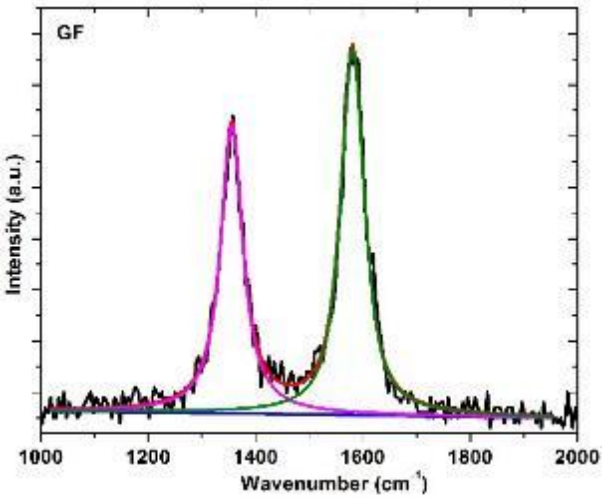

Figure 3.1 Raman fitting of a graphite felt (GF) sample with D and G band.

Raman Spectroscopy was conducted using Witech Alpha300 SR system with a laser wavelength of 488 nm, laser power of 35 mW, a 20X objective lens and 318.5nm spot size. Raman spectra were recorded from 1000 to 2000 cm^{-1} to obtain the D and G band.

3.4.3 BET Surface Area Measurement

Brunauer-Emmett-Teller (BET) is a common method used to gather the textural properties, such as surface area, pore volume, pore size distribution. It explains the physical adsorption of gas molecules on the surface and aids the analysis technique for measuring the specific surface area of the material. Argon and Nitrogen are standard gases used for BET measurement of powders. However, in this experiment, Krypton gas was used, as large

molecule size is more suitable for low specific surface area measurement. For the experiments, BET surface area was determined by Krypton adsorption using an Autosorb™ setup (Quantachrome, Odelzhausen, Germany).

3.4.4 Thermogravimetric Analysis

Thermogravimetric analysis (TGA) was conducted using a TA instrument TGA 2950 (USA). The samples were heated to 760 °C at a rate of 10°C/min under air atmosphere and the weight loss with temperature is obtained.

3.4.5 Surface Characterization

3.4.5.1 X-ray Photoelectron Spectroscopy

X-ray photoelectron spectroscopy (XPS) is a surface analytical technique, which utilizes photoelectric effect and binding energy (BE) of an element to provide information about the chemical composition. The technique probes the distribution of energy of electron from the surface by X-rays and the photoelectric effect, which contains information regarding the atomic composition and oxidation state. In XPS, the sample is first irradiated with the monochromatic X-rays. The sample is placed on the chamber, which is maintained at almost vacuum. The generation of x-rays takes place when accelerating electrons strike high voltage target. The target should produce X-ray and should have high energy to eject core electrons from a large range of elements [9, 10]. The emitted X-ray ejects the atoms from the inner core shells, which is the photoelectric effect. The kinetic energy of the ejected electron is then measured and binding energy is obtained, which is characteristic of the chemical element and its binding state.

XPS experiment was performed using AXIS supra spectrometer at the base pressure of 1.5 X 10^{-8} Torr and working pressure of $2.6x10^{-9}$ Torr by using mono Al Kα (energy 1486.71) generated at 75 Watt. Survey scan was performed between 5- 1100 eV with a dwell time of 100 ms and step of 1eV. The narrow scan was recorded step of 0.05eV with a dwell time of 100-400 ms depending upon the concentration and number of the sweep. Samples are analysed using mono Al kα X-ray source (300-700 μm spot size). XPSPEAK 4.1 with non-linear least squares curve fitting with a Gaussian-Lorentz optimization algorithm was used.

The average surface composition was obtained from the elemental peak, subtracting from the linear background using the atomic sensitivity factor: C1s (0.278) and O1s (0.780). At least two spots were chosen to obtain the spectra to provide information regarding the shift in the peak.

For quantitative analysis, the C 1s spectra were deconvoluted to obtain various components, graphitic carbon C=C (284.5 eV), hydrocarbons C-C (285 eV), C-O (286.5 eV), C=O (288.3 eV) and π-π* (291 eV) peaks of graphite as shown in Figure 3.2 [11]. To obtain the oxygen-containing functional groups, the O 1s spectra were fitted with C-O group at 532.5 eV and carbonyl (i.e. C=O) group at 531.5 eV as shown in Figure 3.2 [12].

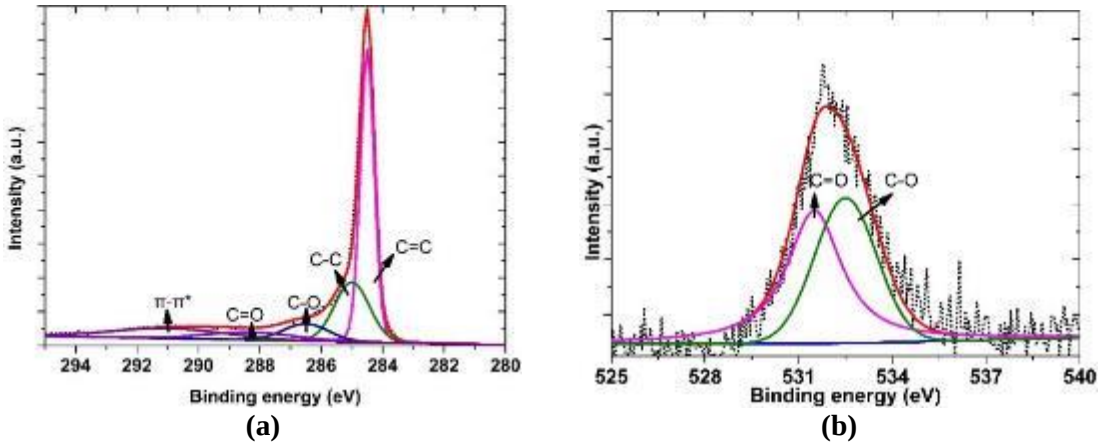

Figure 3.2 Peaks assignment from deconvolution of C 1s (a) and O1s (b).

3.4.6 Electrochemical Characterization

3.4.6.1 Cyclic Voltammetry (CV)

CV is an electrochemical measurement technique, which measures the current produced in the electrochemical cell when a potential is applied. Mostly, a CV electrochemical cell consists of three electrodes, namely a working electrode, a counter electrode and a reference electrode. In CV, the potential of the working electrode is ramped linearly versus the time. The potential is swept between the two potentials i.e. between upper potential and a lower potential. The potential measurement takes place between the working and reference electrode, whereas the current is recorded between the working and counter electrode. The current in a working electrode is plotted against the applied potential to

obtain the CV plot. The excitation signal and corresponding voltammogram are shown in Figure 3.3a and b.

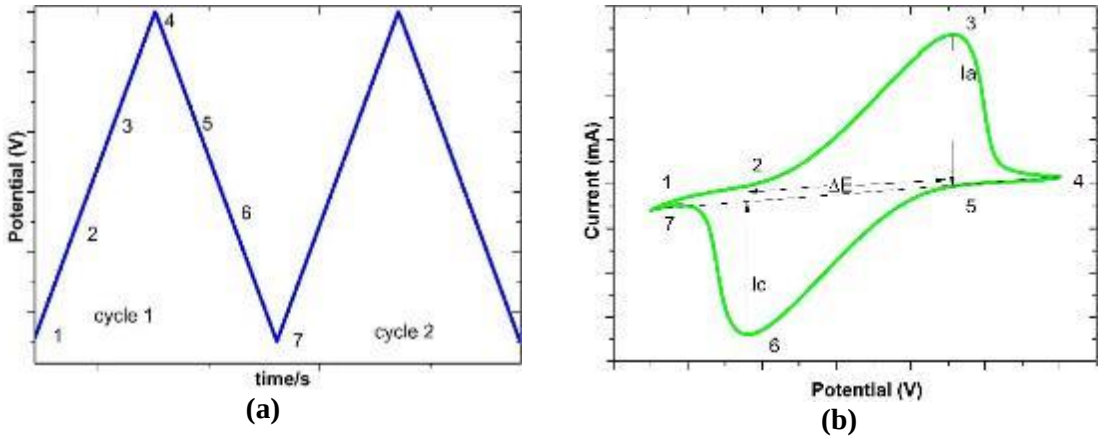

Figure 3.3 (a) CV excitation signal (b) corresponding voltammogram.

The analysis of the CV curve is dependent on the maximum anodic (I_a) and cathodic current (I_c) and the separation potential between the peak (ΔE). The lower value of the ΔE signifies the fast electron transfer process i.e. fast reaction kinetics. Similarly, the ratio of anodic to cathodic current provides information about the reversibility of the reaction. Usually, the information acquired from the analysis of the CV curve is straightforward in case of the planer electrode. However, in this study, a 3D porous electrode is used, which makes it difficult to carry out the CV due to two reasons. Firstly, the electrochemical active surface area (ECSA), as the peak current is directly proportional to the ECSA. The direct measurement ECSA is not possible, so the closest to it is BET, which only refers to the physical surface area. The other disadvantage of the 3D electrode is the volume of electrolyte inside the electrode, which might be exchanged only by the diffusion.

The CV was performed using three-electrode configurations via Biologic workstation (VMP3). An electrode of the area (1 cm x 1 cm) with graphite current collector was compressed in a PVC holder and was used as the working electrode. A saturated mercury sulphate electrode (SMSE, $Hg|Hg_2SO_4|$sat. K_2SO_4) and platinum mesh were used as the reference and counter electrode, respectively. The CV test was performed vs SMSE at the scan rate of 1-5 mV s^{-1}. Before electrochemical measurement, the electrodes were

immersed in the electrolyte to imbibe the electrolyte. For uniformity, all of the electrodes were treated with the same procedure.

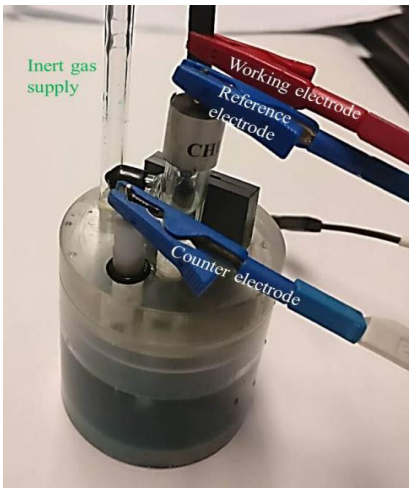

Figure 3.4 Electrochemical cell set-up for measuring CV.

3.4.6.2 Electrochemical Impedance Spectroscopy (EIS)

EIS is a technique to study the frequency behaviour and the corresponding resistive value of a given sample. It provides information about ohmic resistance, charge transfer resistance, diffusion etc. and are expressed in Nyquist and Bode plot.

In potentiostatic EIS measurement, an AC voltage (V_t) with amplitude (V_A) is applied with a certain frequency range ($\omega=2\pi ft$) at a certain potential. Usually, the applied AC voltage is kept between 5-10 mV. This is then expressed in Equation 3.1,

$$V_{(t)} = V_A * \mathrm{Sin}(2\pi ft) = V_A * \mathrm{Sin}(\omega t) \quad (3.1)$$

This input signal results in a change in current (I_t) with an amplitude (I_A) and a phase shift (φ).

$$I_{(t)} = I_A * \mathrm{Sin}(\omega t + \varphi) \quad (3.2)$$

The input voltage can be correlated according to responding current which can be expressed in the form of impedance and phase shift as,

$$Z = \frac{V_{(t)}}{I_{(t)}} = \frac{V_A * \mathrm{Sin}(\omega t)}{I_A * \mathrm{Sin}(\omega t + \varphi)} = Z_A * \frac{\mathrm{Sin}(\omega t)}{\mathrm{Sin}(\omega t + \varphi)} \quad (3.3)$$

This can now be resolved into the real and imaginary part as,

$$Z = \frac{V}{I} = Z_A * e^{j\varphi} = Z_A * (\mathrm{Cos}(\varphi) + j * \sin(\varphi)) = Z_{\mathrm{real}} + j * Z_{\mathrm{im}} \quad (3.4)$$

The impedance data can be represented in the Nyquist plot as shown in Figure 3.5.

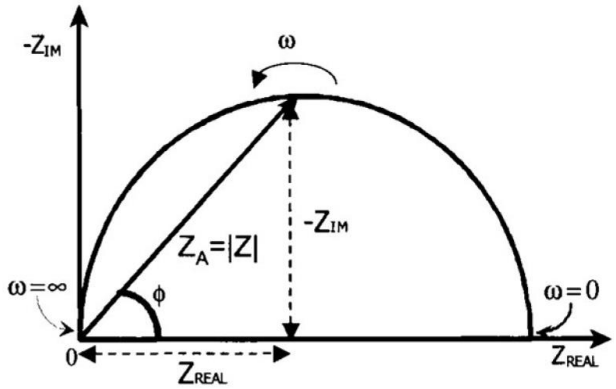

Figure 3.5 Complex plane (Nyquist plot) of impedance [13].

In an electrochemical experiment with redox couple in the conductive electrolyte, the ohmic resistance occurs in high frequency (MHz to kHz), the charge transfer process is observed in the medium range (Hz) while low-frequency range (mHz) is dominated by the diffusion. A physical model has to be employed in order to analyse the impedance data. A simple physical model consists of inductive, resistive and capacitive elements.

The electrochemical interface is often described by planer electrode and ion conducting electrolyte. For this classical electrochemical interface, the reaction occurs at the surface of the electrode. Mostly, the Nyquist plot is obtained using the Randles equivalent circuit. However, the highly porous electrodes have a very high surface area and exhibit different character as compared to a planar electrode. Therefore, it cannot be described by the same equivalent circuit. In planer electrodes, the reaction takes place directly on the surface of the electrodes. Compare to planer electrode, the reaction speed within pores of the porous electrode is limited. The small inner pore volume limits the access for ions moving to the

active interface. Therefore, the electrochemical reaction rate exceeds the diffusion rate of the ions in the pore and thus becomes the dominant step. The transmission line model describes the stepwise flux of ion within a pore [14]. The equivalent circuit in our system is simulated using a Bisquert diffusion element as shown in Figure 3.6.

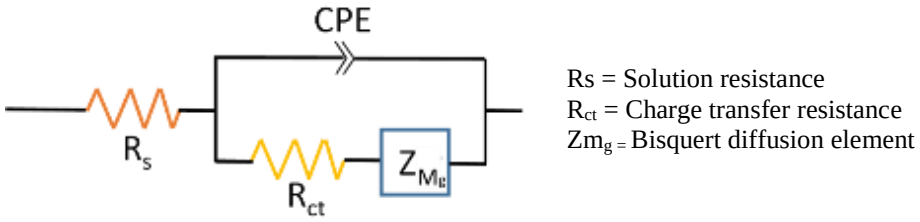

Figure 3.6 Equivalent circuit for EIS fitting.

For the experiments, the same three-electrode setup as that of CV was used. The EIS was performed from 100 kHz to 10 mHz with an applied AC amplitude of 10 mV for the comparison of charge transfer resistance between the samples. Both CV and EIS were performed with the electrolyte containing 1.6 M V^{2+}/V^{3+} in 4 M sulphate at 50% state of charge (SOC).

3.4.6.3 Double Layer Capacitance (DLC)

For estimation of the ECSA, the correlation between DLC and the active surface area plays a significant role. The double layer capacitance (DLC) was also measured using the three-electrode configuration. DLC was performed in the 4 M H_2SO_4 at the scan rate of 10, 20, 50 and 100 mV s^{-1}. The current corresponding to the non-faradic region of 0.2V was used for the calculation. The capacitance was obtained from the slope with the linear fit of scan rate vs current.

For all of the electrochemical experiments, nitrogen gas was purged throughout to create the inert atmosphere. The temperature of the electrolyte was kept constant throughout the experiment.

3.4.6.4 Hydrogen Evolution Reaction (HER)

HER for different types of electrodes was investigated using the three-electrode configuration in M H_2SO_4. The single sweep voltammetry was carried out from 0.2 to -1.6 at a scan rate of 10 mV s^{-1} to measure the onset potential for HER.

3.5 Single Cell Setup and Measurement Procedure

The in-house fabricated flow cell (Figure 5.6) with the active surface area of (5 cm X 4 cm) was used for the investigation of VRFB cell performance. To facilitate the uniform distribution of the electrolyte throughout the porous electrode, the flow channels were provided in the flow frame. As-received graphite felts were employed as the positive electrode, whereas thermally treated electrodes were investigated in the negative side. A cell was assembled with graphite current collectors (SGL Technic Inc., Valencia, CA, USA), an anion exchange membrane (Fumasep FAP 450®, Bietigheim, Germany) and silicone gasket. The electrode compression of 25% was maintained with respect to the initial thickness. To maintain the consistency of electrode compression for experiments, a torque wrench was used during the cell assembly. Each tank of the system is filled with 100 mL of commercial electrolyte with 1.6 M $V^{+3.5}$ in a total of 4 M sulphate (GFE, Nuremberg, Germany). The peristaltic pumps continuously supplied the electrolyte at the rate of 60 mL min^{-1}. The electrolyte temperature was maintained at 24±1 °C throughout the VRFB measurements. A paraffin oil layer was placed on the surface of the electrolyte to prevent the aerial oxidation of the electrolyte during the cell cycling. The cell was charged and discharged with current density ranging from 60 to 100 mA cm^{-2} using a battery charger (NEWARE, China, 10 V/10 A). The long-term performance was evaluated by carrying out 60 cycles test at the current density of 80 mA cm^{-2}. Cell cycling was conducted between the cell potential of 0.9 V and 1.65 V.

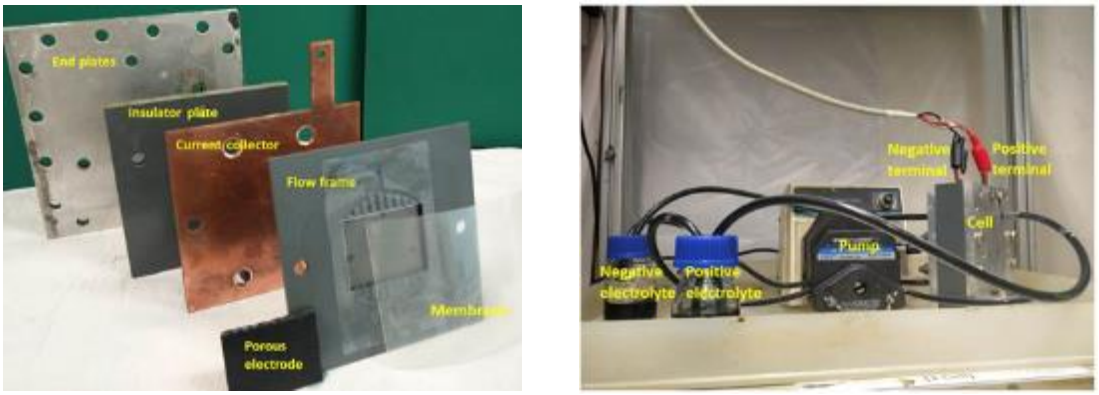

(a) **(b)**

Figure 3.7 Experimental VRB cell (a) exploded half-cell view (b) test setup.

3.6 Segmented Cell

The in-situ investigation of cell performance with varying operating parameters was performed with the aid of the segmented cell.

3.6.1 Experimental Setup

The current collector and bipolar plate on the negative half-cell were divided into sixteen segments as shown in Figure 3.8. The total active area of the cell was 100 cm^2.

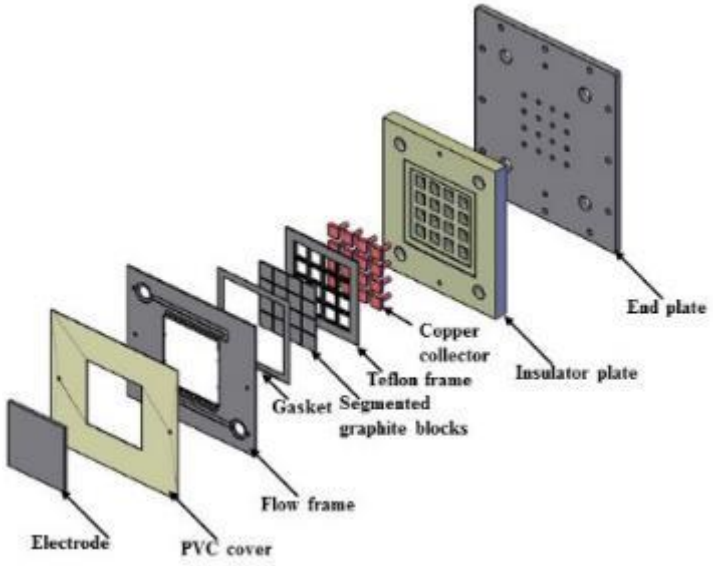

Figure 3.8 Exploded view of a VRFB single cell with segmented negative half-cell components.

PVC insulator plate containing sixteen cavities in order to accommodate segmented CCs and BPs was fabricated. Sixteen small area BPs (type Diabon® F100, SGL Carbon, Meitingen, Germany) were embedded into a Teflon® frame. The CCs were each fixed into cavities in the insulator plate. The latter was positioned adjacently to a PTFE frame containing embedded BP segments. The end plate was fitted with 16 holes to allow the banana plug to be inserted into the holes on the backside of CCs. The flow frame was designed with integrated flow guides to uniformly distribute the electrolyte into the electrode space. Since the porous felt electrode was not segmented and the flow was maintained along the cross-section of the porous electrode, segmentation of components does not affect the flow distribution. To protect the cell from external and internal electrolyte leakage, silicon gaskets were used at the interface between the insulator plate and flow frame. Table 3.1 shows the list of materials used during the assembly of the segmented cell.

Table 3.1 Material used during cell assembly.

Porous electrode	PAN-based carbon felt SIGRACELL GFD 4.6 EA from SGL Carbon (Meitingen, Germany), thermally treated in the air at 600°C for 5 hours, 4.6 mm uncompressed thickness
Bipolar plate (BP)	2 mm thick Diabon® F100 graphite plate segments from SGL Carbon (Meitingen, Germany)
Membrane	Anion exchange membrane FAP 450 (Fumatech GmbH, Bietigheim, Germany), used as-received
Electrolyte	0.8 M $V^{+3.5}$ in 4 M total sulfate (GFE, Nuremberg, Germany)

The experimental setup is shown in Figure 3.9a and b, respectively. Figure 3.9c shows the arrangement of the different segments. The electrolyte flow was maintained upward. Segments (1-4) represent the inlet segments, whereas the segments (13-16) correspond to the outlet segments.

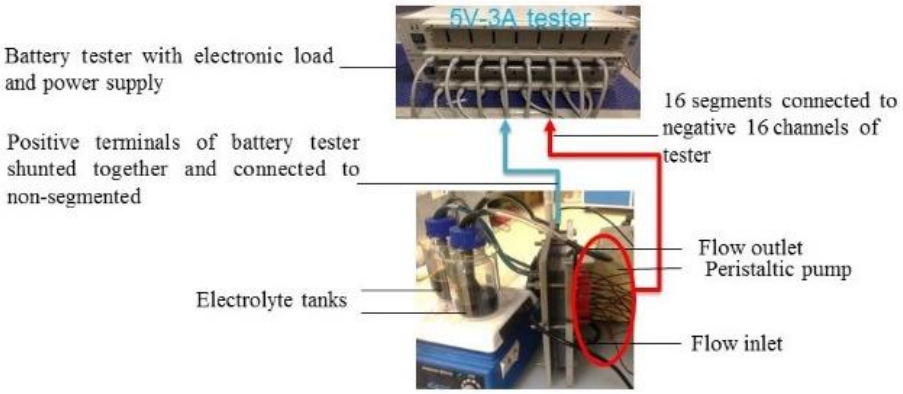

(a)

(b)

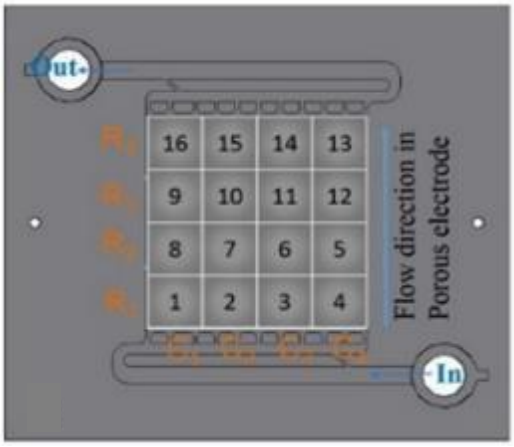

(c)

Figure 3.9 (a) Experimental set up (b) Negative side with the sixteen cables along with inlet and outlet tube (c) arrangement of the sixteen segments showing the direction of electrolyte flow.

The electrolyte volume in each tank is 200 mL with 0.8 M $V^{+3.5}$ in total 4 M sulfate. The low concentration of vanadium of 0.8 M was chosen deliberately in order to operate in the mass transport dominant regime already at relatively high stoichiometry. The compression of the electrode was maintained at 25% (equivalent to 75% of the initial thickness) and a uniform compression during the assembly was ensured using a torque wrench.

3.6.2 Measurement Procedure

A battery tester (NEWARE, China, 5 V, 3 A) with integrated load and power supply, consisting of 16 terminals, was used to charge/discharge each segment. The BTS software allows the control of all sixteen segments en masse as well as independently. The data

recorded for each segment were stored in separate files. Since the segmentation was performed on the negative side, each negative segment was connected to an individual channel of the battery tester, whereas all positive terminals of the battery tester were shunted together and connected to the positive half of the cell. The electrolyte was initially charged to 50% SOC. Thereafter, segments were discharged for a minute, followed by termination at open circuit voltage (OCV). The OCV hold was carried out until all segments were equilibrated. The OCV values, 5 s after the termination of discharge, were plotted into contour diagrams to study the flow distribution. The cell was again charged back to 50% SOC (i.e. OCV = 1.41V) before any subsequent tests. The corresponding SOC for each OCV value was calculated using the following relationships (Equations 1 to 5). Applying the Nernst Equation for the overall cell reaction, the reversible cell potential (open circuit potential, E_{OCV}) can be expressed as:

$$E_{OCV}(T) = E_0(T) + \frac{RT}{F} \ln\left(\frac{a_{V^{2+}} \cdot a_{VO_2^+} \cdot a_{H^+}^2}{a_{V^{3+}} \cdot a_{VO^{2+}}}\right) \tag{3.5}$$

Where E_0 represents the standard cell potential, R is the universal gas constant (R= 8.314 J mol^{-1} K^{-1}), T represents the temperature in Kelvin, F is the Faraday constant (F= 9.648 x 10^4 C mol^{-1}) and a is the chemical activity for the relevant species.

Given the relationships between state-of-charge (SOC) and the stoichiometry of the cell reactions

$$C_{V^{2+}} = C_{VO_2^+} = SOC \cdot C_V \tag{3.6}$$

$$C_{V^{3+}} = C_{VO^{2+}} = (1 - SOC) \cdot C_V \tag{3.7}$$

For the sulfuric acid concentrations of several molar, which are typical of flow battery electrolytes, the proton concentration due to dissociation can be approximated by the sulfuric acid concentration c_{SA}. Considering the formation of a stoichiometric quantity of protons (n = 2) during charge, the total hydrogen ion concentration is

$$c_{H^+} = c_{SA} + 2 \cdot c_V \cdot SOC \tag{3.8}$$

Combining Equations 3.5 to 3.8 yields a general expression for the open circuit voltage of the VRFB cell (E_{OCV}) at a given temperature T

$$E_{OCV}(T) = E_0(T) + \frac{2RT}{F}\ln\left[\frac{c_{SA}\cdot SOC + 2c_V\cdot SOC^2}{1-SOC}\right] \quad (3.9)$$

With c_V and c_{SA} being the concentrations of vanadium and sulfuric acid in the VRFB electrolyte and E_0 the standard electrochemical potential of the cell reaction. This relationship has been verified by potentiometric titrations of the electrolyte samples.

3.7 Compression Cell Setup and Experimental Measurement

An in-house developed flow cell with an active area of 100 cm^2 (10 cm x 10 cm) was used in this study where the arrangement of the different components is shown in Figure 3.10. The PVC flow frames were provided with flow guides to facilitate the uniform flow of electrolyte through the porous electrode. Stainless steel plates (10 mm thick) were used as end plates for pressing the components into contact. Copper plates were selected as current collectors. Battery-grade polyacrylonitrile (PAN)-based carbon felts (Sigracell® GFD, 6 mm thick, SGL Carbon GmbH, Meitingen, Germany) were employed as electrodes. Felts were thermally activated in air at 600°C for 5 hours. The cell was assembled with Sigracell® TF6 graphite BPs (SGL Technic LLV, Valencia, CA, USA) and an anion exchange membrane (FAP 450, Fumatech GmbH, Bietigheim-Bissingen, Germany).

Six different compression levels of the porous electrode (15%, 20%, 25%, 30% 35% and 40%) were investigated. The electrode compression was varied by using combinations of silicone and Teflon™ gaskets of different thickness. A torque wrench was employed to ensure uniform compression of the electrode. After each assembly, the thickness between the two end plates was measured to ensure the exact compression of the electrode. The volume of the electrolyte in each tank was 150 mL and the concentration of the electrolyte was 1.6 M $V^{+3.5}$ in total 4.5 M sulphate (GFE, Nürnberg, Germany). The electrolyte flow rate in both half-cells was kept constant at 100 mL min^{-1} by means of peristaltic pumps. Nitrogen at a flow rate of 10 mL min^{-1} was supplied routinely to both electrolyte tanks to maintain an inert atmosphere in the headspace of the electrolyte. The pressure drop in each half-cell was continuously measured using two pressure gauges (Georg Fischer, Germany).

Similarly, the temperature was continuously monitored in both the tanks by PT100 type sensors.

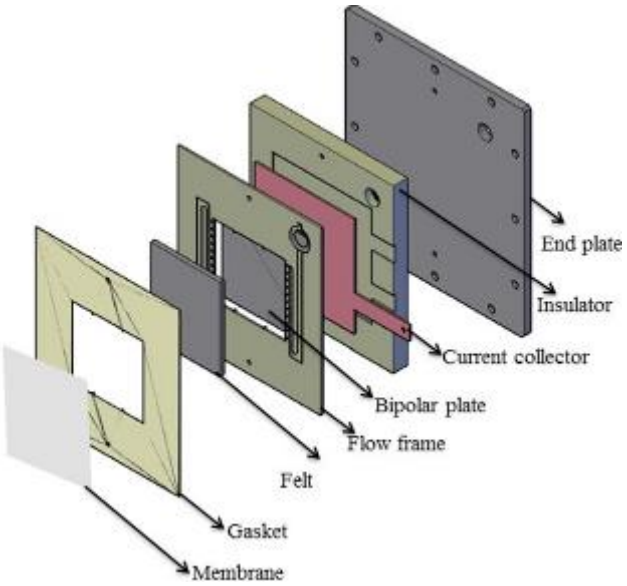

Figure 3.10 A half-cell arrangement of the VRFB showing the different components.

An identical cell was assembled without the ion-exchange membrane to determine the dry cell resistance by means of the four-probe method. Cell cycling was performed using a battery charger (NEWARE, China, 10 V, 10 A). Five cycles were run at varying current densities between 40 to 80 mA cm^{-2}, followed by 50 long term cycles at 40 mA cm^{-2}. Galvanostatic charge and discharge cycles were conducted between cut-off voltages of 1.65 V and 0.9 V, respectively.

3.8 Half-cell Measurement

Half-cell potential measurements through reference electrode insertion in VRFB cell allow an independent study of both half-cells. The results from the individual study of half-cells can be used to improve the battery components and optimize the operation.

3.8.1 Set-up for the Overpotential Measurement

An in-house fabricated VRFB single cell with an active area of 20 cm^2 (5 cm x 4 cm) was used. The cell was assembled using 4.6 mm graphite felt electrodes (SIGRACELL GFD 4.6 EA, SGL Carbon GmbH, Meitingen, Germany), 0.6 mm thick graphite bipolar plates (SIGRACELL® TF6, SGL Technic LLC, Valencia, USA) and anion exchange membrane

(Fumasep® FAP 450, Fumatech GmbH, Bietigheim-Bissingen, Germany). A commercial VRFB electrolyte: 1.6 M $V^{+3.5}$ in a total of 4 M sulfate (GFE, Nuremberg, Germany) was used unless stated otherwise. The flow rate was kept constant at 60 mL min^{-1} using peristaltic pumps. Paraffin oil was used to prevent aerial oxidation of the V^{+2} during cell operation. The electrolyte temperature was kept constant at 24±1°C throughout the measurement. Saturated mercurous sulphate electrode (SMSE), $Hg|Hg_2SO_4|$ sat. K_2SO_4) as reference electrodes were inserted near the outlet of each half-cell, using purpose-built holders, as shown in Figure 3.11. The tip of the inserted electrode was only in contact with outflowing electrolyte.

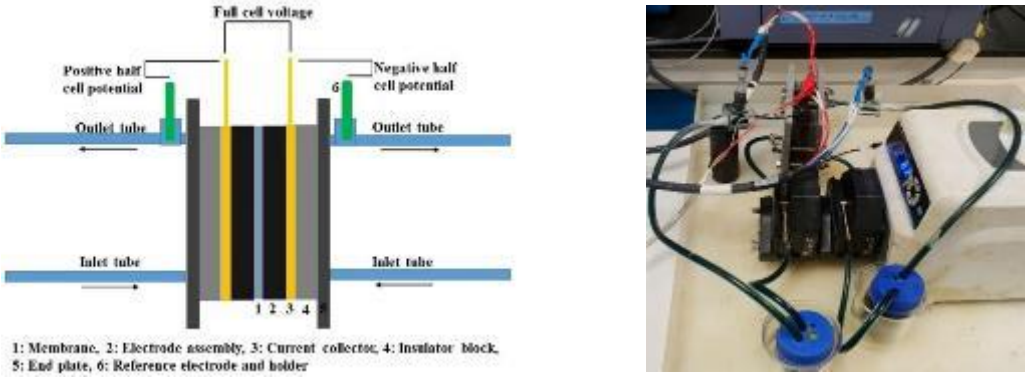

Figure 3.11 Cell set-up for half-cell potential measurement (a) schematic diagram and (b) picture of the setup.

Cell cycling and polarization measurement were performed using a battery charger (NEWARE, China, 3 V/3 A). Simultaneously, using two channels from a multi-channel potentiostat (VMP3-BioLogic, France), the half-cell potentials (measured against the appropriate reference electrode) were recorded. From the measurements, cell voltages of both half-cells and the full cell during charging/discharging can be determined. This procedure allowed the separation of the potential difference terms in the cell. Before each experiment, both of the reference electrodes were dipped in the same electrolyte and the difference in voltage was measured. The difference in voltage was zero, which ensured that the reference electrode did not create an imbalance in potential so that the data acquired during the experiment were precise. The pristine, heat treated (600°C for 5 hours in the air) and mixed acid treated (H_2SO_4/HNO_3:3/1) electrodes were used during cell assembly for testing at various experimental conditions.

3.8.2 Measurement Procedure

The cell cycling was performed between a cut-off voltage of 0.9 V and 1.65 V at 80 mA cm^{-2}. The polarization measurement was carried out by varying current densities from 20 mA cm^{-2} to 140 mA cm^{-2}. For polarization measurement, the cell was charged to 50% state of charge and followed the routine: 1 min OCV, 1 min charge, 1 min OCV and 1 min discharge. The same routine was repeated with varying current density. All the experiments were performed in galvanostatic mode.

References

[1] G. Lawes, *Analytical Chemistry by Open Learning*, John Wiley & Sons, **1987**, 54-85.

[2] C.R. Brundle, C.A. Evans, S. Wilson, Encyclopedia of materials characterization: surfaces, interfaces, thin films, *Gulf Professional Publishing*, **1992**.

[3] J.C. Spence, Experimental high-resolution electron microscopy, *Oxford University Press*, **1988**.

[4] J. Spence⊥, H. Kolar, G. Hembree, C. Humphreys, J. Barnard, R. Datta, C. Koch, F. Ross, J. Justo, *Philosophical Magazine*, **2006**, 86, 4781-4796.

[5] G. Washer, F. Blum, Raman spectroscopy for the nondestructive testing of carbon fiber, *Advances in Materials Science and Engineering*, **2008 (2009)**.

[6] M. Pimenta, G. Dresselhaus, M.S. Dresselhaus, L. Cancado, A. Jorio, R. Saito, *Physical chemistry chemical physics*, **2007**, 9, 1276-1290.

[7] M.D. Bertolucci, D. Harris, Symmetry and spectroscopy: An Introduction to vibrational and electronic spectroscopy, *Courier Dover Publications*, NY, **1978**.

[8] F. Tuinstra, J.L. Koenig, *The Journal of Chemical Physics*, **1970**, 53, 1126-1130.

[9] J. Craig, Practical surface analysis, volume 1—auger and x-ray photoelectron *spectroscopyWiley, Chichester*, **1990**.

[10] J.F. Watts, J. Wolstenholme, An introduction to surface analysis by XPS and AES. *John Wiley and SonsLtd*, **2003**.

[11] E.H. Lock, D.Y. Petrovykh, P. Mack, T. Carney, R.G. White, S.G. Walton, R.F. Fernsler, *Langmuir*, **2010**, 26, 8857-8868.

[12] E. Desimoni, G. Casella, A. Morone, A. Salvi, *Surface and Interface Analysis*, 15 **1990**, 15, 627-634.

[13] V.F. Lvovich, Impedance spectroscopy: applications to electrochemical and dielectric phenomena, *John Wiley & Sons*, **2012**.

[14] J. Bisquert, *Journal of Electroanalytical Chemistry*, **2001**, 499, 112-120.

Chapter 4

Electrode Material and its Modification to Enhance the Performance of VRFBs

This chapter discusses the three-core set of results related to electrode properties and the techniques for electrode modification to enhance VRFB performance. First, the physical and electrochemical properties of the pristine electrodes were investigated to obtain information about the electrode activation required in each half of the cell. The second part relates to investigating the effect of thermal oxidation time and temperature on the physical and electrochemical properties, and proposes the most optimized time and temperature for thermal treatment. Finally, a section describing doping of titanium carbide catalyst onto the electrode to enhance the electrochemical activity in a negative half-cell is presented.

A part of the findings in this section is published as an original research paper:
-Ghimire, P.C., Schweiss, R., Scherer, G.G., Wai, N., Lim, T.M., Bhattarai, A., Nguyen, T.D. and Yan, Q., 2018. Titanium carbide-decorated graphite felt as high performance negative electrode in vanadium redox flow batteries. Journal of Materials Chemistry A, 6(15), pp.6625-6632.
-Ghimire, P.C., Schweiss, R., Scherer, G.G., Wai, N., Lim, T.M., Bhattarai, A., Nguyen, T.D. and Yan, Q, A comprehensive study of the thermal oxidation of PAN-based carbon felts and its optimization for the negative half-cell of the all-vanadium redox flow battery,Carbon-[Under Review]

4.1 Electrode Material, Properties and its Reproducibility

PAN-based graphite felts are the most widely used material for the VRFBs. During production, the fibres are stabilized and graphitized at various temperatures in nitrogen or argon atmosphere between 300°C-2000°C. Therefore, there is a probability that the carbon surface properties may vary due to operating conditions and precursor. The objective of this study is to investigate the physical and electrochemical properties of the as-received PAN-based graphite felt. Before the modification of the graphite felt, it is very important to realize that the material received for the experiments have the same physical and electrochemical properties. The graphite felt from three different batches of production were obtained for the comparison. The correlation is sought between the properties and the performance of the electrodes. The samples from the three different batches are named GF-A, GF-B and GF-C, respectively.

4.1.1 Analysis by SEM, XRD and Raman

The surface morphology of the graphite fibres obtained from SEM is shown in Figure 4.1. As shown, there is almost no difference between the fibres at the magnification of 8000. The graphite fibres show characteristic striations parallel to its length due to the fabrication process from PAN precursors.

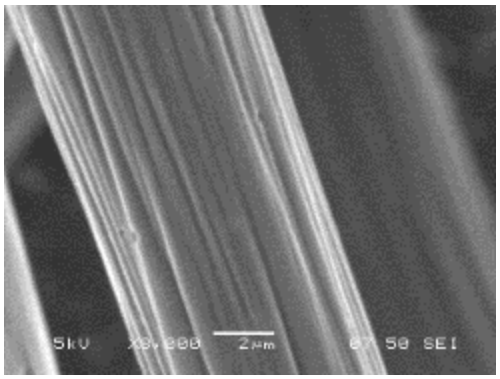

GF-A

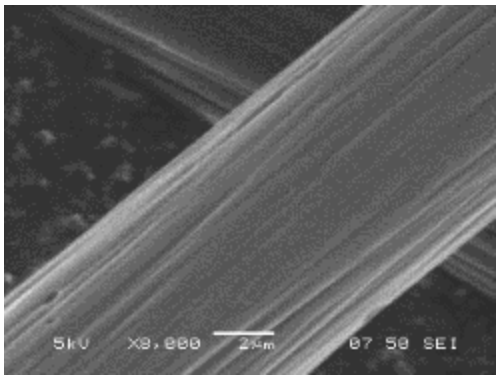

GF-B

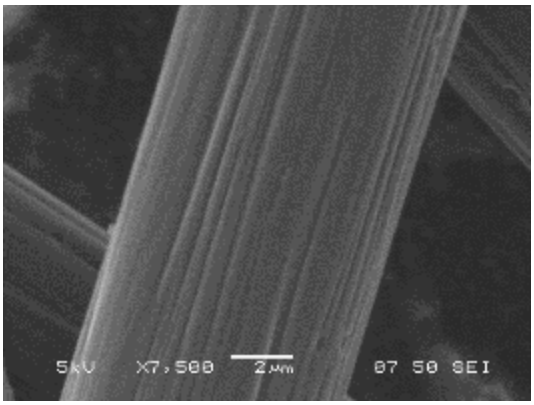

GF-C

Figure 4.1 SEM Images for three different as-received carbon fibres.

XRD results of the graphite felts from different batches are shown in Figure 4.2. The most significant diffraction peak is located at 26.5° corresponding to (002) plane. Similarly, two weak diffraction peaks are observed at 43.5° and 54° corresponding to (100) and (004) planes. It is clear from the XRD spectrum that there is no significant difference in peak intensity among the samples, signifying a similar proportion of the graphitic phase and amorphous carbon.

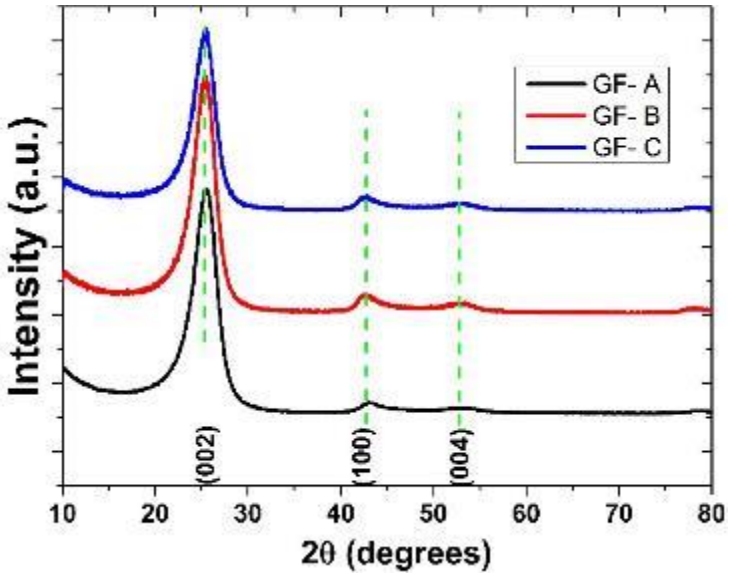

Figure 4.2 SEM Image for as-received electrodes.

Figure 4.3 shows the Raman spectrum, which can provide in-depth information about the crystallinity and structural order of the surface of the graphite fibre and the ratio of the defects to the graphitization degree for the given samples. Figure 4.3a shows the D band

corresponding to structural defects or amorphous carbon around 1280-1350 cm^{-1} and G band corresponding to sp^2 carbon around 1580-1600 cm^{-1}. The ratio of the intensity of defects to graphitization i.e. I_D to I_G thus indicates the degree of crystallinity. As shown in Figure 4.3b, all of the samples exhibit a similar ratio, signifying the same degree of defects on the surface of the fibre.

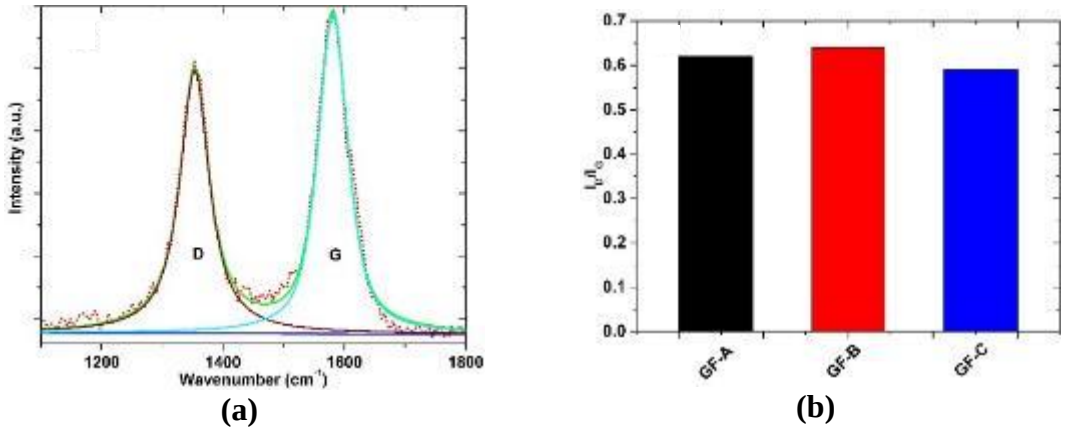

Figure 4.3 (a) Raman spectrum (b) I_D/I_G ratio for three different as-received electrodes.

4.1.2 XPS Analysis

In order to understand the surface chemistry of the graphite felt, it is important to investigate the surface composition and type of functional groups present. XPS being the most suitable technique is employed to monitor the composition and functional groups. It is to be noted that XPS is a surface sensitive technique and the information provided by it is limited to only a few nanometers of the surface.

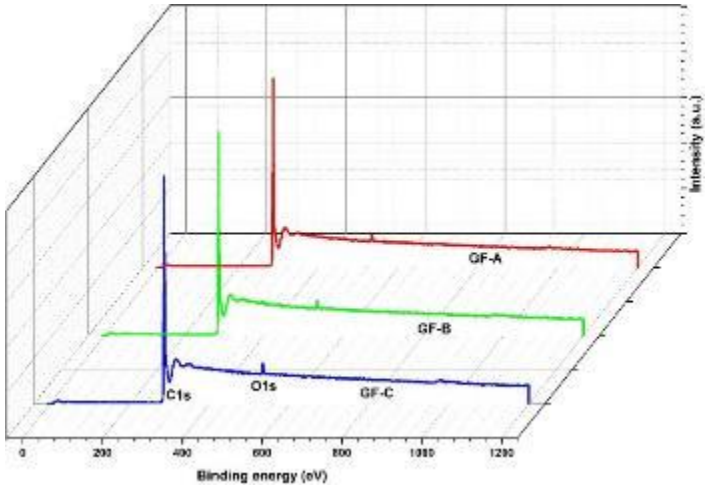

Figure 4.4 XPS survey spectra of different samples.

Figure 4.4 shows the XPS survey spectra of the different samples. The corresponding elemental content of the samples is listed in Table 4.1. The results show that there is no noticeable difference between the carbon and oxygen content among the samples investigated. From the survey spectra, it is not possible to trace the presence of nitrogen, as the presence of nitrogen might be below the detection limit of the XPS.

Table 4.1 Surface composition from XPS (atomic %).

Sample number	Carbon %	Oxygen %
GF-A	98.69	1.38
GF-B	98.99	1.88
GF- C	98.37	1.42

For the quantitative analysis of the graphitic and amorphous carbon, C 1s spectra was fitted with different peaks. The components are attributed to the graphitic carbon, C=C (284.5 eV), hydrocarbons, C-C (285 eV), C-O (286.5 eV), C=O (288.3 eV) and π-π* (291 eV). Figure 4.5 shows the respective deconvoluted peaks for different samples, and the percentage is listed in Table 4.2.

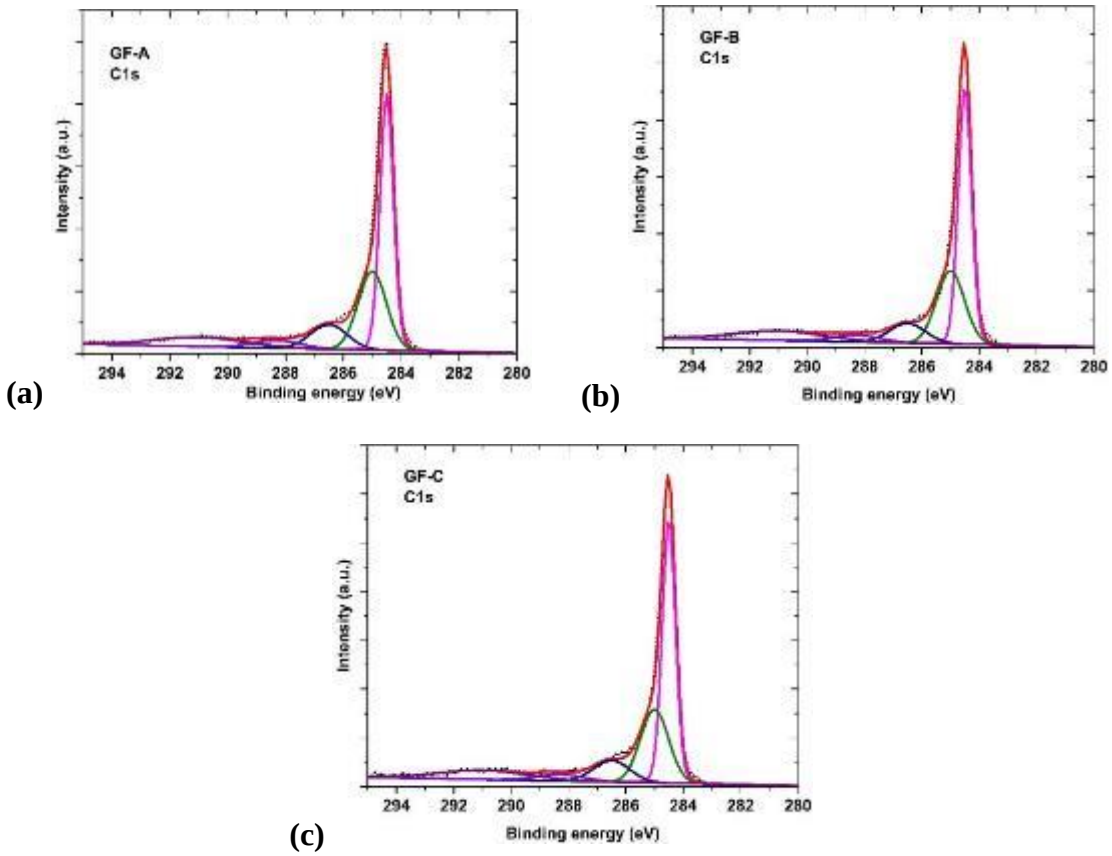

Figure 4.5 XPS C1s spectra components of samples GF-A (a), GF-B (b) and GF-C (c).

The amorphous and graphitic carbon content remains almost the same for all of the samples investigated. The oxygen-containing functional groups obtained from the C1s spectra also show a similar amount of C-O and C=O groups.

Table 4.2 Percentage of oxygen-containing functional groups obtained from deconvolution of C1s spectra.

	B.E	GF-A (%)	GF-B (%)	GF-C (%)
C=C	284.50	55.59	54.25	56.86
C-C	285	20.56	19.25	19.24
C-O	286.50	12.23	12.10	11.31
C=O	288.30	7.11	7.81	6.98
π-π	291.00	4.50	6.57	5.58

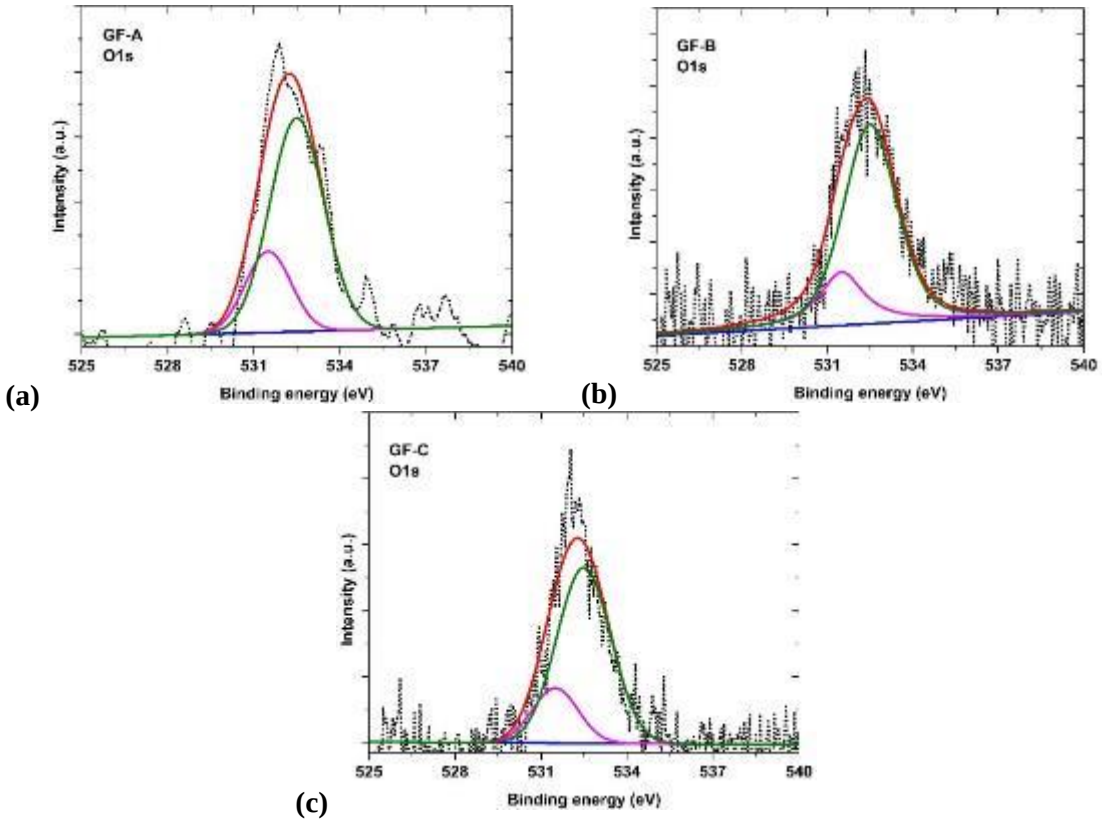

Figure 4.6 XPS O1s spectra components of samples GF-A, GF- B and GF- D.

To further quantify and analyze the various oxygen-containing functional groups, O1s spectra were deconvoluted using the two peaks C-O at 532.5 eV and C=O at 531.5 eV.

Figure 4.3 shows the O1s spectra for the different samples and the fitting results are listed in Table 4.3. It is observed that there is no significant difference in either C=O or C-O groups for the samples.

Table 4.3 Percentage of oxygen-containing functional groups obtained from deconvolution of O1s spectra.

	B.E	**GF-A (%)**	**GF-B (%)**	**GF-C (%)**
C=O	531.50	24.26	22.41	20.88
C-O	532.50	75.74	77.59	79.12

The results from the O1s deconvolution indicates a similar result as obtained from C1s deconvolution, signifying the ratio of C-O to C=O remains similar for different pristine samples. Therefore, it is well established from the result of the XPS that the surface compositions of the pristine graphite felt from different batches obtained for the study have similar physical properties.

4.1.3 Electrochemistry (Single Electrode)

CV and EIS are the most effective techniques to understand the electrochemical activity of the electrodes. For comparison, all of the samples are subjected to the CV and EIS in both negative and positive redox couple. The surface area for as-received samples is extremely low (0.4-0.6) $m^2 g^{-1}$ in comparison to activated sample. In addition, the number of defects and oxygen content is also low. These properties result in different kinds of interaction between the electrode with negative and positive redox couple.

In the negative redox couple, the wettability of the electrode is extremely low. Therefore, the electrode is unable to exhibit any kind of oxidation or reduction peak as shown in Figure 4.7a. For this reason, the wettability of the electrode can be increased by immersing it into the negative electrolyte with vacuum pumping being performed in order to remove the air trapped inside the electrode. However, it is difficult to reproduce the CV result using this method, as there is no accurate technique to quantify the process itself.

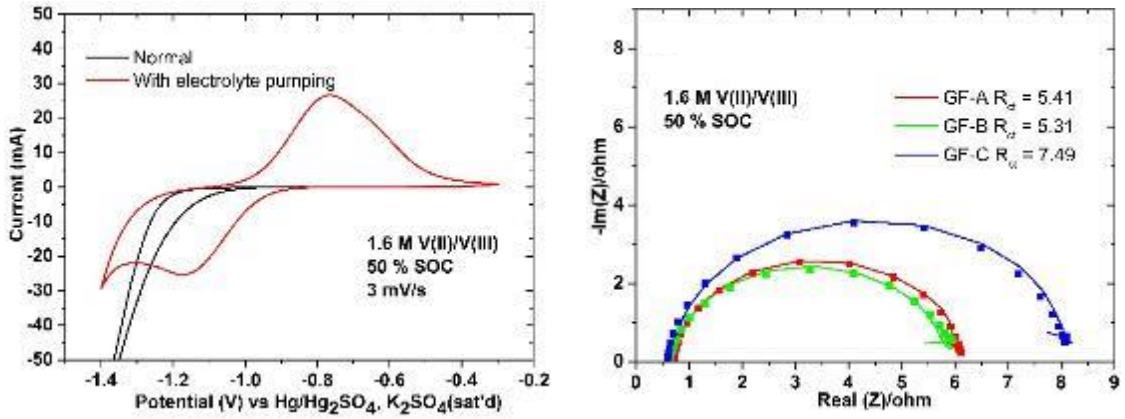

(a) **(b)**

Figure 4.7 (a) CV for the pristine graphite felt with and without vacuum pumping of electrolyte and (b) EIS of the pristine samples GF-A, GF-B and GF-C in negative redox couple.

Figure 4.7b shows the Nyquist plot for three different pristine electrodes in negative redox couple. The highest charge transfer resistance is exhibited by GF-C, whereas GF-A and GF-B showed the same charge transfer resistance. This small discrepancy of R_{ct} value in the sample GF-C might be possibly due to gas trapped inside the porous electrode, which will result in less active area and higher charge transfer resistance.

In contrast, the electrochemical properties exhibited by the electrodes on the positive electrolyte are very different. The pristine electrode is immediately wetted as soon as it is immersed in the positive redox couple. Therefore, there is no necessity to imbibe the electrode in the electrolyte with the aid of a vacuum pump before the experiment. The CV curve and Nyquist curve for the given samples are shown in Figure 4.8a and 4.8b.

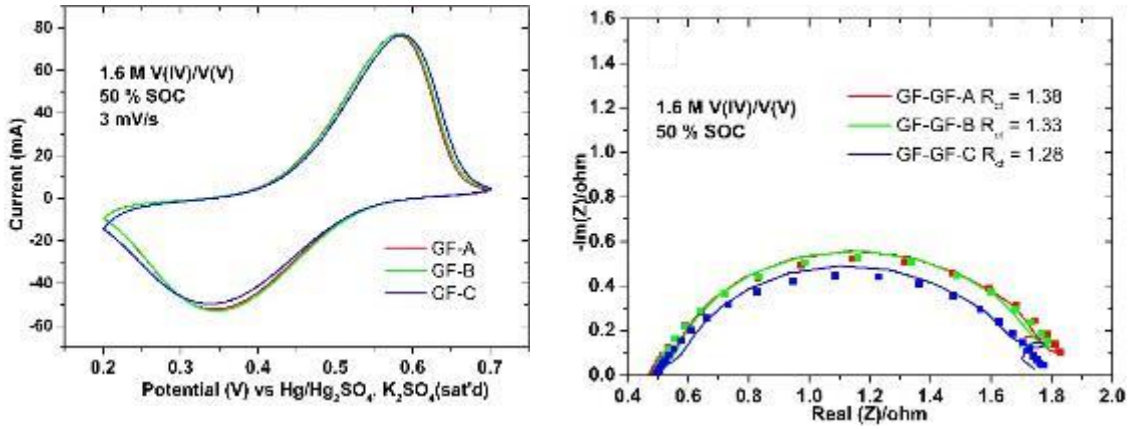

(a) **(b)**

Figure 4.8 (a) CV for pristine samples and (b) EIS for pristine samples in the positive redox couple.

As can be observed from the CV result, the oxidation and reduction peaks for all three samples lie in the same potential with the same peak current. This signifies that electrochemical activity of the pristine electrodes is similar in positive redox couple. The EIS results are also in good agreement with the CV. The charge transfer resistance for all of the samples is almost similar.

The electrochemical behaviour of the electrode is reflected by major changes, such as electrochemically active surface area (ECSA), defects number and oxygen-containing functional groups [1, 2]. Double layer capacitance (DLC) reflects the change in all of these parameters. The DLC calculation has already been described in subsection 3.4.6.3. Table 4.4 shows the DLC values for the pristine samples.

Table 4.4 Area specific DLC values for pristine samples.

Sample	DLC (µF cm^{-2})
GF-A	3.29
GF-B	4.68
GF-C	3.77

It is clear that all samples exhibit a similar value of DLC. It is worth to be noted that the pristine electrode has very low DLC value and the DLC value increases after the modification/activation of the electrodes.

In the negative half-cell of VRFB, hydrogen evolution reaction (HER) is an undesirable side reaction. Therefore, it is necessary to investigate the samples performance of samples using linear sweep voltammetry as described in section 3.4.6.4.

Figure 4.9 shows the onset potential for all of the samples investigated. It is clear from the plot that the onset potential for all of the samples is similar, signifying hydrogen evolution potential in negative half-cell is almost the same for all of the electrodes studied.

Overall, it can be concluded from the electrochemical analysis that the electrochemical interaction of the pristine electrodes is different for positive and negative redox couple, and

the investigated pristine electrodes showed similar electrochemical properties with respect to DLC, R_{ct}, CV and EIS results.

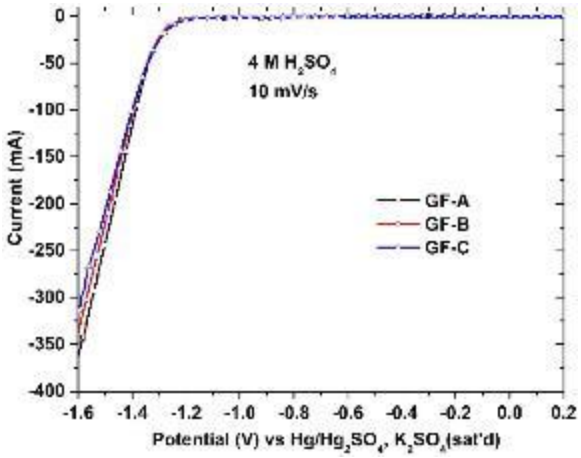

Figure 4.9 Liner sweep experiment in 4 M H_2SO_4 to evaluate HER.

4.1.4 Flow Cell Performance

To evaluate the flow cell performance, cell cycling tests were performed by utilizing each electrode at various current densities ranging from 60 mA cm^{-2} to 100 mA cm^{-2}. The cell was assembled with 25% of electrode compression.

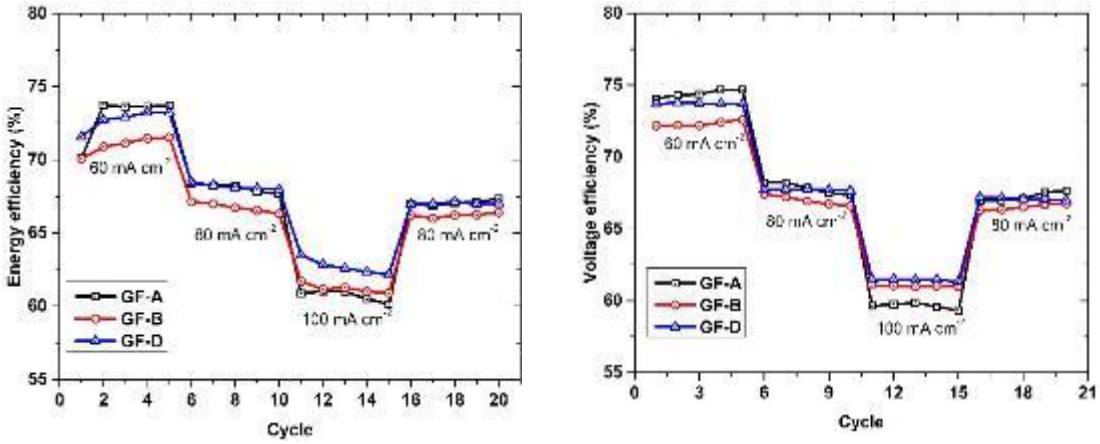

(a) **(b)**

Figure 4.10 (a) EE (b) VE at various current densities.

The performance evaluation of the flow cell is expressed in terms of energy efficiency (EE) and voltage efficiency (VE) and the results are shown in Figure 4.10. It is evident from cell cycling test results that VE and EE are very low for all of the samples investigated. The discrepancy among the EE even at the highest current density of 100 mA cm^{-2} is less than

1.5%, which might be due to the difference in electronic resistance. During cell assembly, special consideration has been taken by using the same torque to fasten the cell, so as to keep the similar dry cell resistance. Despite all these considerations, a minor possibility of variation due to electronic resistance always exists. Overall, all of the samples exhibited almost the same EE and VE at various current densities.

To observe the stability or to see changes occurring as the cycle number progresses, cell cycling has been performed at 80 mA cm^{-2} for 65 cycles. The CE, EE and VE are shown in Figure 4.11.

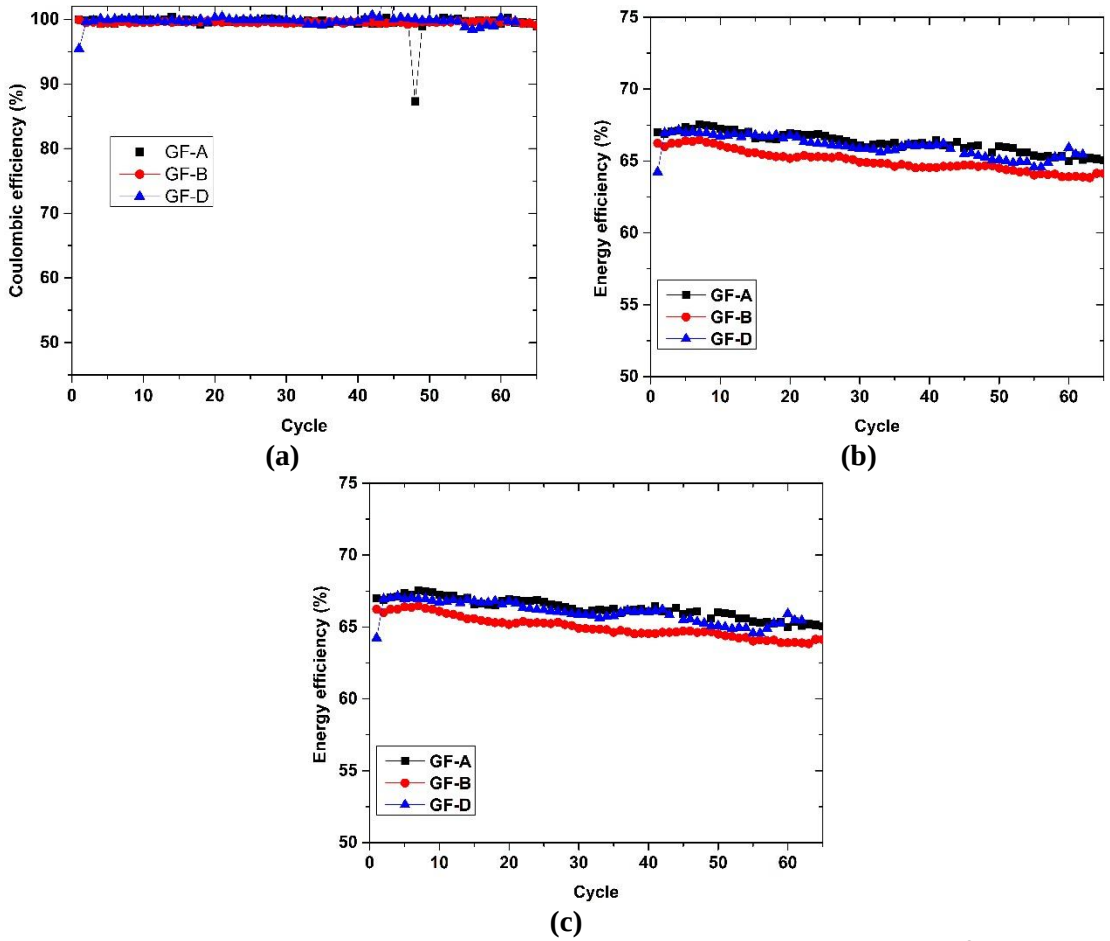

Figure 4.11 (a) CE (b) EE and (c) VE at constant current density of 80 mA cm^{-2}.

CE is the same for the entire cell assembled, as it is dependent on the membrane property. Since the same kind of membrane has been used throughout the experiment, CE is constant. EE and VE showed exactly the same result as that of short cell cycling. One of the features observed over the long run is the slow decay of capacity, which is the result of the crossover

of the active species. However, it can be recovered by the rebalancing of the electrolyte. Cell cycling clearly shows the similarity of electrodes in term of cell performance.

4.2 Requirement for Electrode Modification/Activation

In the previous section, an investigation about pristine electrode properties and their reproducibility has been performed. To enhance the performance of the VRFB, the modification of the electrode before the cell assembly is necessary. From the literature review, it can be concluded that different type of modification/activation techniques can be implemented. However, it is necessary to have clarity for the activation of the electrode in each half-cell. To investigate the performance of each half-cell, a completely new experimental configuration has been developed. The detail of the experimental setup and the measurement procedure is described in subsection 3.7. A full investigation of the electrode type, stoichiometry variation, electrolyte variation etc. of this setup is explained in chapter 5.2. In this section, only the half-cell performance with two different types of electrodes are described to understand the degree of the overpotential.

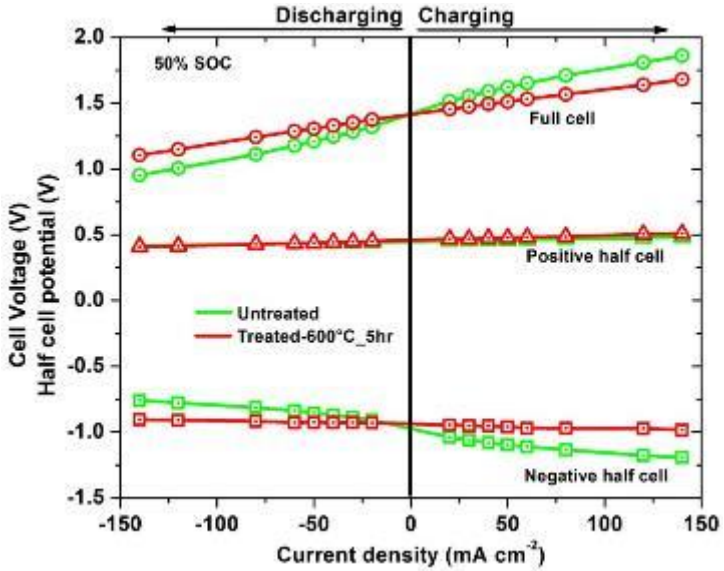

Figure 4.12 E-I curve for as-received and thermally treated graphite felt at 50% SOC and flow rate of 60 mL min^{-1}.

Figure 4.12 shows the polarization curve performed at 50% of SOC at the flow rate of 60 mL min^{-1}. The positive half-cell does not show any significant change with the use of a thermally treated electrode (600°C for 5hours). If examined in detail, the slight increase in

overpotential is observed, which is in total agreement with the previous studies [3, 4]. In contrast, a significant reduction in overpotential is observed with the use of the thermally treated electrode. This clearly indicates that the negative half-cell is the performance-limiting reaction in VRFBs. Therefore, in the upcoming subsection, the techniques to enhance the negative half-cell performance through different electrode modification will be studied.

4.3 Optimization of Thermal Oxidation of the Electrodes

The objective of this study is the systematic investigation of thermal oxidation of the electrode and its effect on the electrochemical properties by varying temperature and duration in a negative half-cell. Although, there have been previous studies on the thermal modification of the graphite felt, almost all of the studies have taken either constant temperature or constant time variation with respect to thermal oxidation. Therefore, in this study, we have considered the temperature and time impact on the oxidation along with the thermogravimetric curve by varying both temperature and time. The results from various characterization techniques along with cell cycling test are employed to identify the crucial electrode properties, such as surface composition, specific surface area, defects and electrochemical parameters including wetting properties, mass loss, surface morphology etc. Finally, the optimized electrode treatment temperature is proposed, which is applicable to the lab as well as industrial scale.

4.3.1 Temperature-time Selection Criteria

The temperature ranges were selected based on the result of TGA analyses (Figure 4.13). The first region of selection is at 400°C, which reflects minor mass loss due to desorption of adsorbed impurities and moisture. For the samples treated at 400°C, the oxidation time was varied from 10 to 30h. For temperatures ranging from 500°C to 600°C, we kept the treatment time constant (5 h). Finally, to observe the changes occurring at a higher temperature, a temperature of 750°C within the zone of rapid decomposition was selected. To avoid massive mass losses of the felt, the treatment time of the electrode at this temperature (750°C) was kept at 5, 10 and 15 min, respectively. Figure 4.13 shows the TGA results with the prefix T denoting the oxidation temperature, suffix h and m referring

to the hours and minutes, respectively. GF represents the pristine graphite felt from the manufacturer.

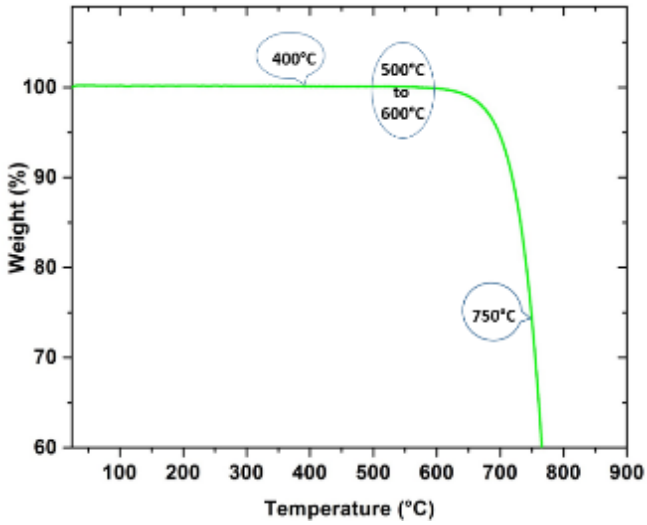

Figure 4.13 Thermogravimetric analysis of pristine electrode.

4.3.2 Mass Loss due to Thermal Oxidation

Figure 4.14 shows the weight loss (%) of the graphite felt samples at different oxidation temperatures and times. The mass loss is insignificant for the felts treated at 400°C. The mass loss increases with temperature even being exposed for shorter intervals.

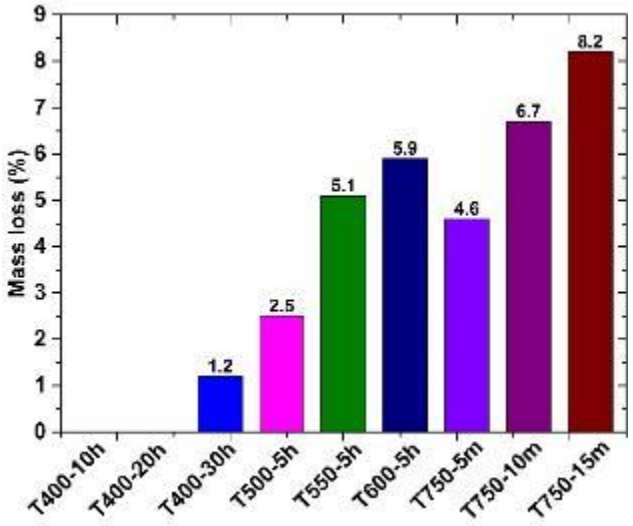

Figure 4.14 Mass loss of electrode as a function of oxidation temperature and time.

CO_2 evolution occurs with progressive mass loss. The active sites on the surface of the carbon fibre form oxygen-containing functional groups and eventually release CO_2. The

stepwise mechanism, as shown in Figure 4.15 for the graphite fibre surface oxidation has been widely described [5, 6].

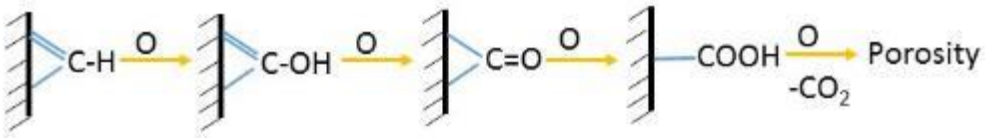

Figure 4.15 Progressive oxidation mechanism for graphite fibre surface.

4.3.3 Morphological and Structural Change in Properties

Figure 4.16 shows the materials characterization by XRD and FESEM. The most significant diffraction peak is located at 25.6°, corresponding to the (002) plane. In addition, two smaller peaks can be observed at 43.1° and 53.5°, corresponding to the (100) and (004) planes, respectively. An increase in oxidation temperature leads to a slight decrease in diffraction intensity. The peaks are distinct for as-received graphite felt (GF), but a small decrease in intensity is observed with increasing temperature and treatment duration. The fading intensity of diffraction may be due to the defects introduced on the surface by the oxidation. However, this is not normal, as the carbon fibres are already graphitized above 1800°C, and hence, there is very little probability of a change in bulk properties due to thermal oxidation.

For investigation, the interlayer spacing (d_{002}) and crystallite stacking height (L_c) have been calculated using the Scherrer formula. The plot of d_{002} and L_c is provided in Figure 4.16c. It is observed that d_{002} of the pristine fibre is 3.46 A° and increases with the increase in oxidation temperature and reaches a maximum of 3.52 A° for the sample T600-5h. This may be due to the increased oxidation temperature, with increased material removal rate each layer comprising fibre may have become more disordered, resulting in imperfect layer stacking. However, the L_c remains almost constant irrespective of the thermal oxidation influence.

For further investigation, the FESEM images of the carbon fibre are taken as shown in Figure 4.16b. The fibre surface of the GF is smooth, whereas visible morphological changes are observed after thermal oxidation. An increase in temperature and in duration leads to an increase in the surface roughness. For fibres treated at temperatures of T600-5h

and T750-15m, even small cavities and initiation of delamination are observed. Partial decarboxylation that results in mass loss leads to an increase in the roughness of the fibre surface. The pore and morphology changes depend upon the temperature and extent of CO_2 evolution.

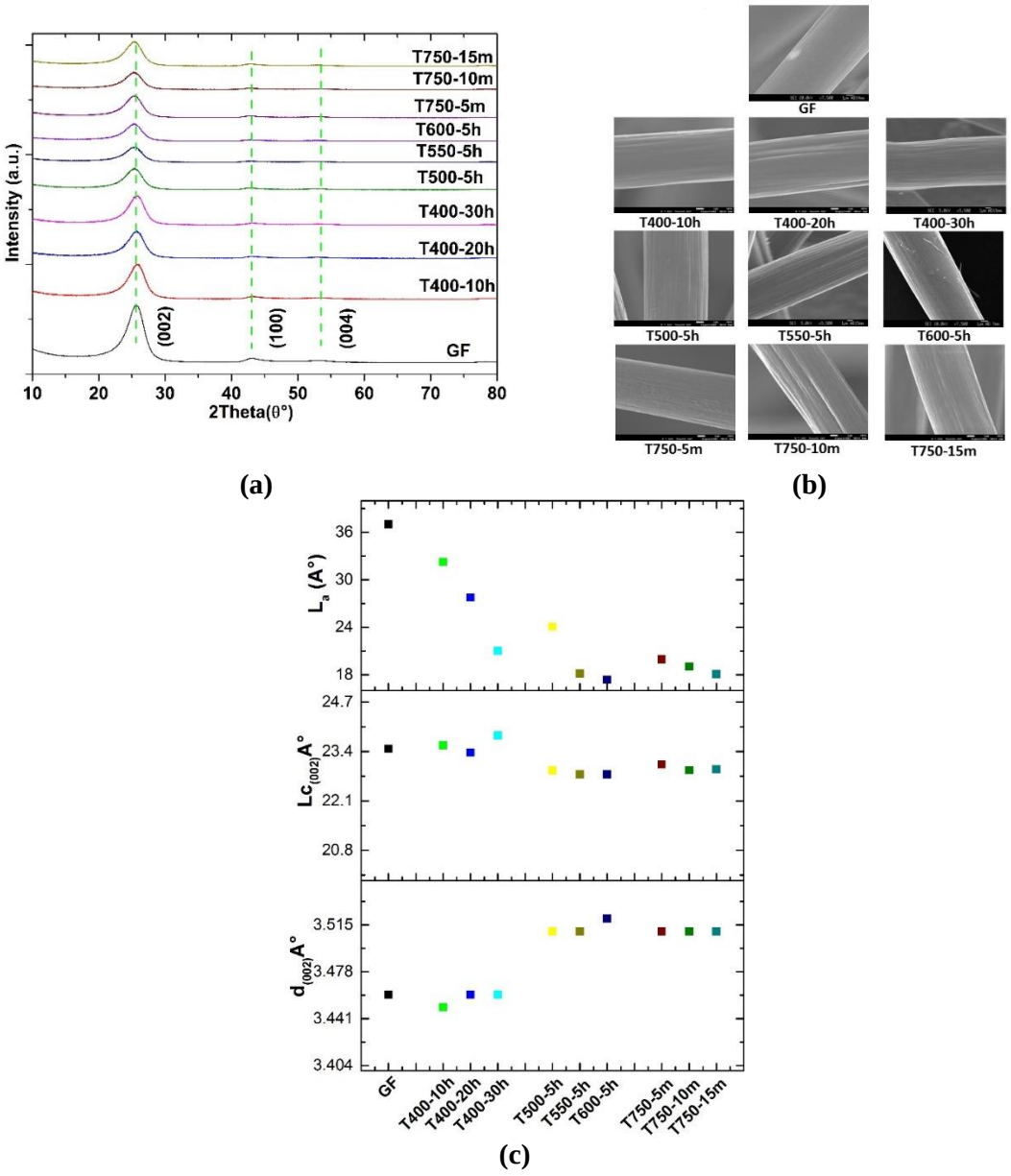

Figure 4.16 (a) XRD pattern of the graphite felt at various oxidation temperature (b) FESEM image of carbon fibre at various oxidation temperature (c) Change in d-spacing (002), $L_{c\ (002)}$ obtained from XRD and L_a obtained from Raman spectroscopy for as- received and thermally treated electrodes.

The electrolyte accessibility of the electrodes is evaluated by simple wetting tests and the results are shown in Figure 4.17a. Electrolyte droplets at different sizes are formed due to higher contact angle for the electrodes which are not activated or partially activated. The droplets on the surface of the GF and the T400 series samples remain unchanged. Absorption is gradual for the sample T500-5h, as traces of the electrolyte can be observed on the surface. However, immediate electrolyte uptake is observed for the rest of the sample, signifying improved hydrophilicity of electrodes after oxidation with an increase in temperature. Nevertheless, the electrolyte accessibility technique provides only qualitative information about the characteristics of electrode/carbon fibre before and after oxidation.

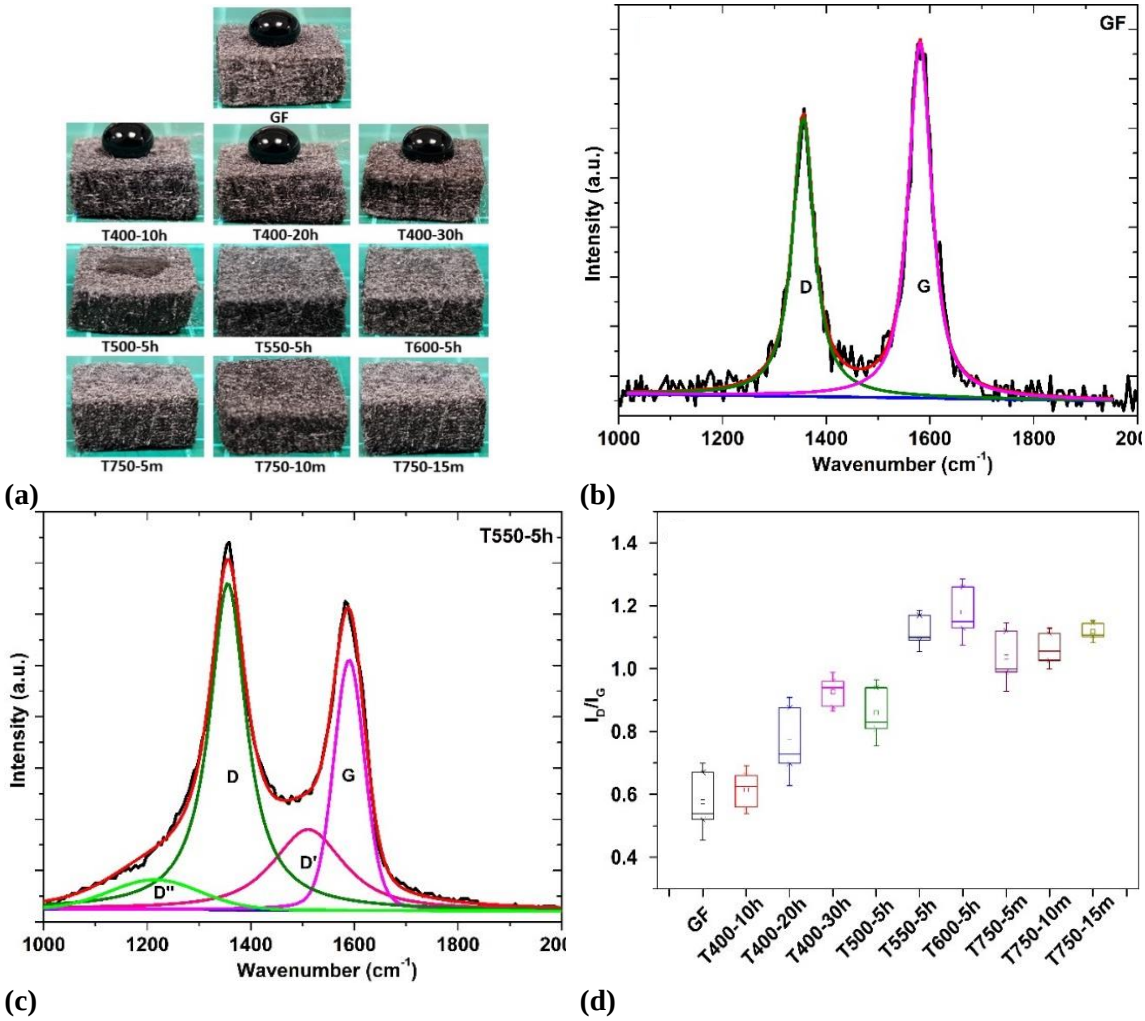

Figure 4.17 (a) Electrolyte accessibility photograph for various electrodes (b) Raman spectra for the as-received electrode (c) Raman spectra for electrode pre-treated at T550-5h (d) ratio of the intensity of D band to G band.

The amount of defects and graphitic degree of the samples have been determined with confocal Raman. The D and G bands measurement is used for the characterization of samples. The first order Raman mode, also known as G band (Graphitic) appear at around 1585 cm^{-1} corresponding to sp^2 carbon atoms. Similarly, the D band (disordered) which provide information about the amorphous carbon and defects originating from a second order scattering appear at around 1355 cm^{-1} [7]. Raman spectra of the GF reveals two distinct peaks of G and D band as shown in Figure 4.17b. However, the activated electrodes showed the reduced G peak and increased D band with a broadening of two peaks as shown in Figure 4.16c. The enlarged spectrum allows for fitting additional peaks at 1210 cm^{-1} (D'') and 1510 cm^{-1} (D'), which is assigned to the disordered graphitic lattice and amorphous carbon, respectively [8]. The change in the structural ordering and crystallinity is analysed by the intensity ratio between the I_D and I_G band. The penetration depth of the 488 nm laser is about 50 nm [9], as the exact confocal penetration depends on the instrumental and sample parameters. Hence, the spectra reflect the surface properties only. Figure 4.17d presents the ratio of intensity for D to G band for all of the samples, ascribing the increase in this value to an increase in surface defects or decrease in graphitic domains. It is very obvious that the thermal oxidation induces defects (i.e. edge sites) on the surface of the fibre. Similarly, the amount of amorphous carbon content also increases. Therefore, the ratio increase with increasing temperature and exposure time. The highest defect density is observed for the samples treated at T550-5h, T600-5h and T750 series. Samples T550 and T600 need to be exposed for a longer time than the sample T750 for the emergence of major defects and increase in sp^3 carbon content.

The Raman spectrum was also used to calculate the crystalline size (L_a) [10] and the results are plotted along with d_{002} and L_c from XRD to acquire the correlation as shown in Figure 4.16c. With the procession of the material loss, the decrease of L_a is observed, and reached a minimum for T750-15m and T600-5h, directly correlating with the burn-off amount. This is the effect of removal of C atoms from the edge of the crystallites. Thus, the crystallinity

of the thermally oxidized fibre becomes more disordered with decreasing size of the crystallites than pristine fibre.

4.3.4 Electrochemical Properties

The electrochemical properties of the various electrodes have been investigated with respect to the negative half-reaction by cyclic voltammetry and the results are shown in Figure 4.18. The parameters obtained from Figure 4.18 are listed in Table 4.5. The vertex potentials for the CV are selected in order to avoid the hydrogen evolution reaction (HER) as it is an undesirable side reaction. HER may influence the reaction by forming bubbles on the surface of the electrode as well as influencing/blocking the diffusion of the reactant to the surface.

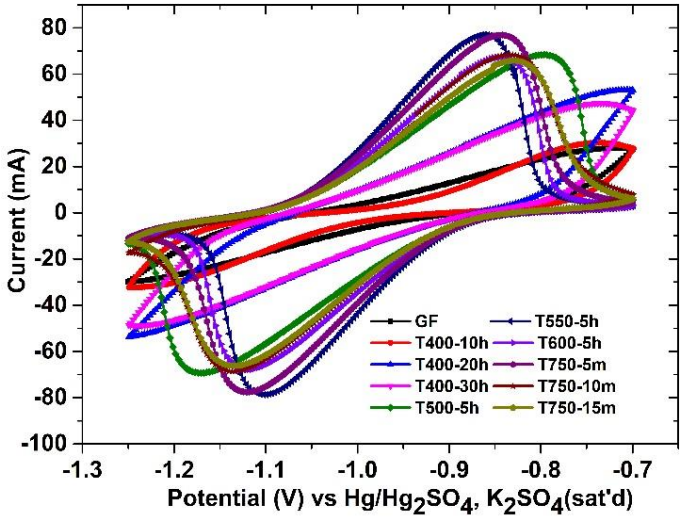

Figure 4.18 CV curve recorded at 5 mV s^{-1} for as-received and thermally oxidized electrodes in a negative redox couple.

As can be seen from Table 4.5, increasing oxidation temperature (T550-5h to T750-5m) reduces peak separation. This value exhibits a minimum for the T550-5h sample. The peak current intensity is at maximum for the T550-5h, T600-5h and T750-5m samples. This implies that the electrochemical activity for T550-5h, T600-5h and T750-5h samples are maximum. However, the specimens treated at T400 show a very high peak potential separation, indicating sluggish electron transfer. All samples exhibited the same ratio of anodic to cathodic peak current, indicating similar degrees of reversibility.

Table 4.5 The parameters obtained from CV curves for various electrodes.

Sample	ΔEp (V)	I_a/I_c	Sample	ΔEp (V)	I_a/I_{pc}
GF	0.52	1.05	**T550-5h**	0.24	1.01
T400-10h	0.50	1.03	**T600-5h**	0.27	1.01
T400-20h	0.51	0.99	**T700-5m**	0.26	1.01
T400-30h	0.49	1.03	**T700-10m**	0.30	1.01
T500-5h	0.37	1.01	**T700-15m**	0.30	1.01

Figure 4.19 displays the Nyquist plot of electrodes with an excitation signal of 10 mV under open circuit potential, and the corresponding impedance parameter are shown in Table 4.6. All Nyquist plots are deemed to have semicircle and a linear part corresponding to a high and low frequency, respectively. It is evident from the figure that the system is mixed controlled by diffusion and charge transfer. The ohmic resistance of solution and electrode is obtained from the point of intersection of a semicircle, the x-axis at high frequency (Rb), the diameter of the semicircles provides the charge transfer (R_{ct}) value, and the inclined line at low frequency represents the ion diffusion in the pore of the electrodes. R_{ct} value of the GF is the largest, indicating poor electrochemical activity.

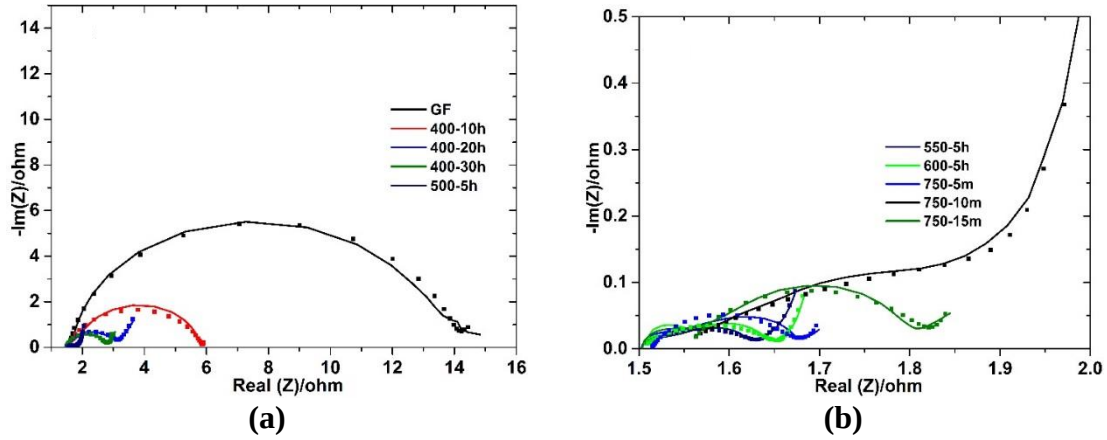

Figure 4.19 Nyquist diagrams obtained using the different graphite felt electrodes.

The electrochemical performance is enhanced by the electrode oxidation temperature. The best result is exhibited by the T550-5h, followed by T600-5h and T750-5m samples. It can be observed from the R_b values that the oxidation hardly influences the conductivity of the electrodes. R_{ct} of the GF is the largest, indicating poor electrochemical activity (slow charge transfer kinetics). As expected, the value of the R_{ct} reduces after oxidation. The lowest R_{ct} is found for the samples oxidized at T550-5h, followed by T600-5h and T750-

5m. The constant phase element (Q) increases with the oxidation temperature, indicating that oxidation enhances double layer capacitance of the solution/electrode interface, which reflects a higher surface area. The results obtained from EIS are in total agreement with the results obtained from the CV.

Table 4.6 Impedance parameter obtained from fitting the experimental data for different electrodes.

Sample	R_b (Ω)	R_{ct} (Ω)	Q ($F.s^{\wedge(a-1)}$)	a
GF	1.54	12.29	1.25E-03	0.91
T400-10h	1.52	5.86	1.41E-03	0.88
T400-20h	1.49	1.66	8.43 E-03	0.86
T400-30h	1.51	1.51	1.80 E-03	0.77
T500-5h	1.52	0.32	9.00E-02	0.65
T550-5h	1.50	0.13	1.12 E-02	0.51
T600-5h	1.50	0.15	8.20 E-02	0.53
T700-5m	1.50	0.15	1.40 E-02	0.63
T700-10m	1.50	0.29	7.81 E-02	0.61
T700-15m	1.50	0.27	3.80 E-02	0.72

Double layer capacitance (DLC) is a quantity which depends on the electronic structure of the carbon surface. Graphite electrode consists of basal and edge planes, which have different specific capacitance values [11]. The double layer capacitance for edge and basal planes studied on highly oriented pyrolytic graphite (HOPG) differs between 50-100 μF cm^{-2} and 1-3 μF cm^{-2}, respectively [12-14]. The edge plane has a much higher DLC compared to the basal plane, possibly due to a larger surface area resulting from micro fissures [11, 14]. The low DLC of graphite basal plane in contact with electrolyte is due to the space charge capacity (C_{sc}) being smaller than the Helmholtz layer capacity (C_h)[15]. Overall, a distinct correlation exists between the DLC and the electrochemically active surface area [11]. The change in DLC values as an effect of thermal oxidation is shown in Table 4.7.

Table 4.7 Gravimetric double layer capacitance, BET surface area and the specific double layer capacitance (normalized by the BET surface area) for the GF and thermally oxidized samples.

Sample	DLC (μF mg^{-1})	BET(m^2g^{-1})	DLC/BET (μF cm-2)
GF	20.0	0.37	5.4

T400-10h	68.3	0.7	9.76
T400-20h	145.0	1.53	9.47
T400-30h	213.3	3.01	7.08
T500-5h	575.5	15.1	3.07
T550-5h	1090.1	9.22	11.80
T600-5h	909.0	6.46	14.07
T700-5m	819.7	4.61	17.70
T700-10m	642.0	6.07	10.57
T700-15m	309.7	2.82	10.98

The DLC of the GF is the lowest and increases with the T400 series and eventually reaches a maximum at T550-5h, followed by T600-5h and T750-5m. The DLC decreases rapidly beyond T750-5m, which may be due to higher mass loss. The surface area is determined using BET measurements. The BET values from Table 3 show that the oxidation of electrodes leads to a significant increase in surface area and follows almost the same behaviour as that of DLC. The BET value is maximum for T500 sample with an area of 15.1 $m^2 g^{-1}$ compared to GF with an area of 0.37 $m^2 g^{-1}$. Since the DLC value is directly proportional to the area of the electrode surface, normalization is performed using BET surface area and is listed in column 3 of Table 4.7. The normalization data also indicate an increase of area-specific DLC with the oxidation of electrode, which is due to the increase of edge site in graphitic structure [16].

4.3.5 Spectroscopic Measurement

The elemental composition and the nature of the functional groups on the electrode surface were further evaluated by means of X-ray photoelectron spectroscopy (XPS). The acquired C1s and O 1s spectra were deconvoluted in order to gain information about these types of functional groups. The wide overview spectra showed the presence of only carbon and oxygen on the electrode surface as shown in Figure 4.20.

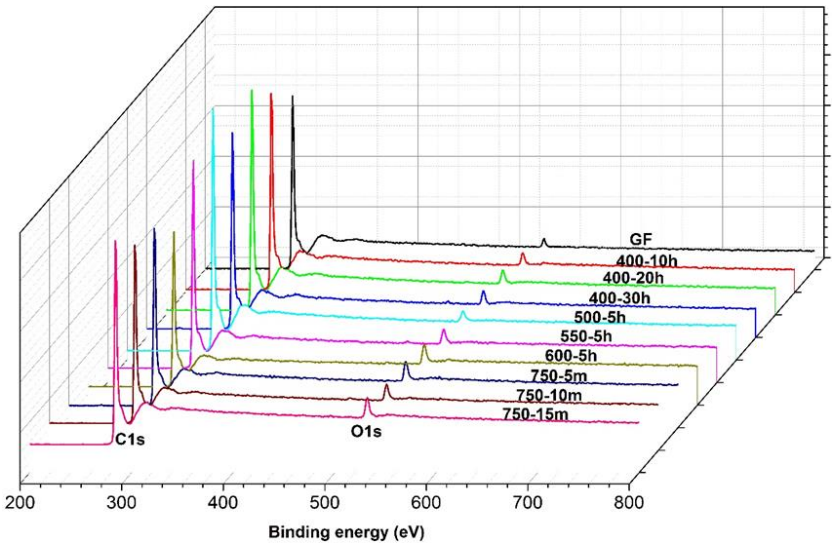

Figure 4.20 XPS wide spectra for the given samples.

The O 1s peak is small on the GF, which becomes significantly larger with respect to the thermal modification. The atomic % of both carbon and oxygen are presented in Table 4.8 An increase in electrode oxidation temperature leads to an increase in oxygen content, particularly for those samples treated above T500, indicating the oxidation of carbon (i.e. increase in sp^3-C content) and formation of oxygen-containing functional groups. Overall, an increasing temperature produces an increased O/C atomic ratio. For quantification, the C 1s spectra are deconvoluted to obtain the various components, graphitic carbon C=C (284.5 eV), hydrocarbons C-C (285 eV), C-O (286.5 eV), C=O (288.3 eV) and π-π* (291 eV) peak of graphite (Figure 4.21) [17]. Not any clear trend of increase or decrease of either C-O or C=O group from C 1s is observed.

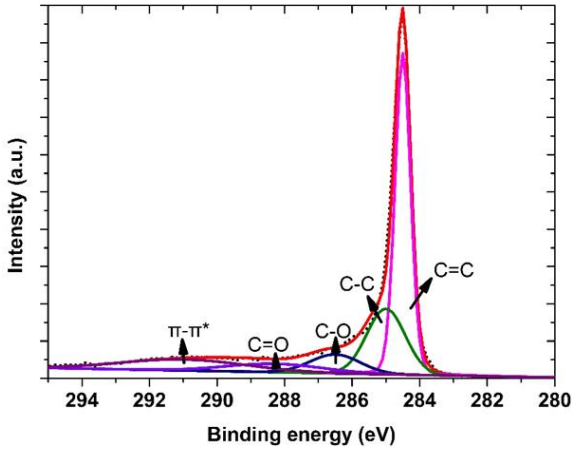

Figure 4.21 The assigned functional group peaks from deconvolution of C 1s.

Table 4.8 Surface composition obtained from XPS (atomic %) and percentage of C-O and C=O group obtained from the deconvolution of O 1s peak.

Sample	Oxygen (%)	Carbon (%)	O/C	C=C	C-O	C=O	BET ($m^2 g^{-1}$)
GF	1.31	98.69	0.013	56.11	75.7	24.2	5.4
T400-10h	2.73	97.21	0.029	55.59	37.5	62.4	9.76
T400-20h	3.23	96.77	0.033	52.22	37.8	62.1	9.47
T400-30h	3.55	96.45	0.037	50.26	45.6	54.3	7.08
T500-5h	3.86	96.14	0.040	48.15	25.3	74.6	-
T550-5h	5.40	96.60	0.057	49.40	19.2	80.6	11.80
T600-5h	6.60	93.40	0.071	45.81	16.4	83.6	14.07
T700-5m	6.00	94.00	0.064	50.10	62.6	37.4	17.70
T700-10m	4.16	95.84	0.043	49.56	78.3	21.7	10.57
T700-15m	5.01	94.99	0.053	47.25	82.0	17.2	10.98

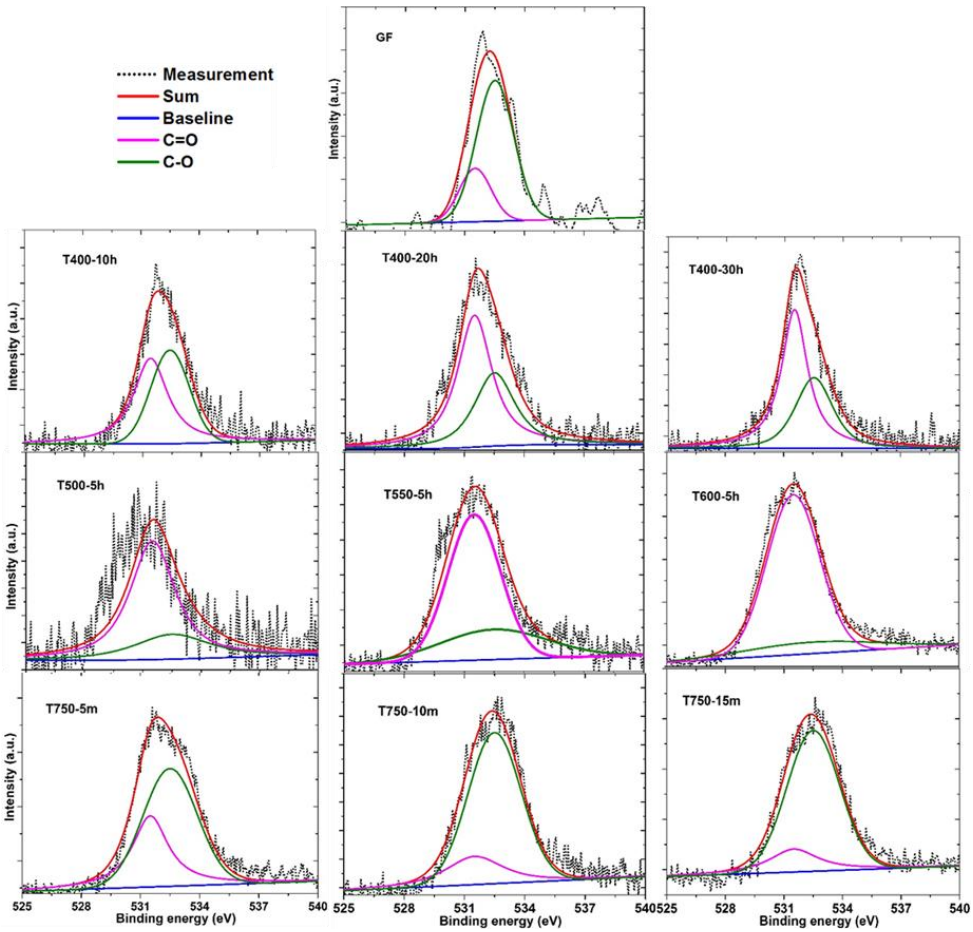

Figure 4.22 The deconvoluted O 1s spectra with their respective oxygen-containing functional groups.

To obtain a better understanding of the oxygen-containing functional groups, the O 1s spectrum is fitted with literature data for C-O group at 532.5 eV and the C=O group at 531.5 eV [18]. The fitting results are listed in Table 4.8. The results show that longer oxidation times for the electrode results in more carbonyl functional groups. By contrast, GF and the electrodes of the T750 series exhibit a higher content of the C-O group. It is well established that the C-O groups are created as a consequence of the breakage of C=C bonds and the longer oxidation times result in the formation of the C=O functional group. Hence, it is very hard to explain that either of the two or only one functional groups is responsible for the performance enhancement. Nevertheless, the overall increase in oxygen-containing functional groups has been reported to catalyze the negative half redox reaction [3, 19].

4.3.6 Flow Cell Performance

For the evaluation of flow cell performance, cell cycling tests have been carried out using each type of electrode at various current densities, ranging from 60 mA cm^{-2} to 100 mA cm^{-2}. Energy efficiency (EE) and voltage efficiency (VE) of a VRFB cell containing different felt at the negative electrodes are shown in Figure 4.23. It can be seen that the lowest values for EE and VE are observed for the GF and T400-10h samples, respectively. The low wettability (oxygen content) of the fibre surface and the low specific area are responsible for the poor performance. Increasing oxidation time significantly increases the EE and VE for the T400-20h and T400-30h samples. At a current density of 100 mA cm^{-2}, a significant increase (~12%) of EE and VE is observed as compared to the GF samples. This is also reflected by an increase in surface area, oxygen-containing functional groups and a decrease in charge transfer resistance. The EE and VE of T500-5h, T750-15m and T750-10m samples are within the 1.5% range, indicating almost the same level of cell performance. Superior performance is shown by the T550-5h, T750-5m and T600-5h, respectively. At 100 mA cm^{-2}, a significant increase of (~17%) in EE as compared to the value for the GF sample is observed.

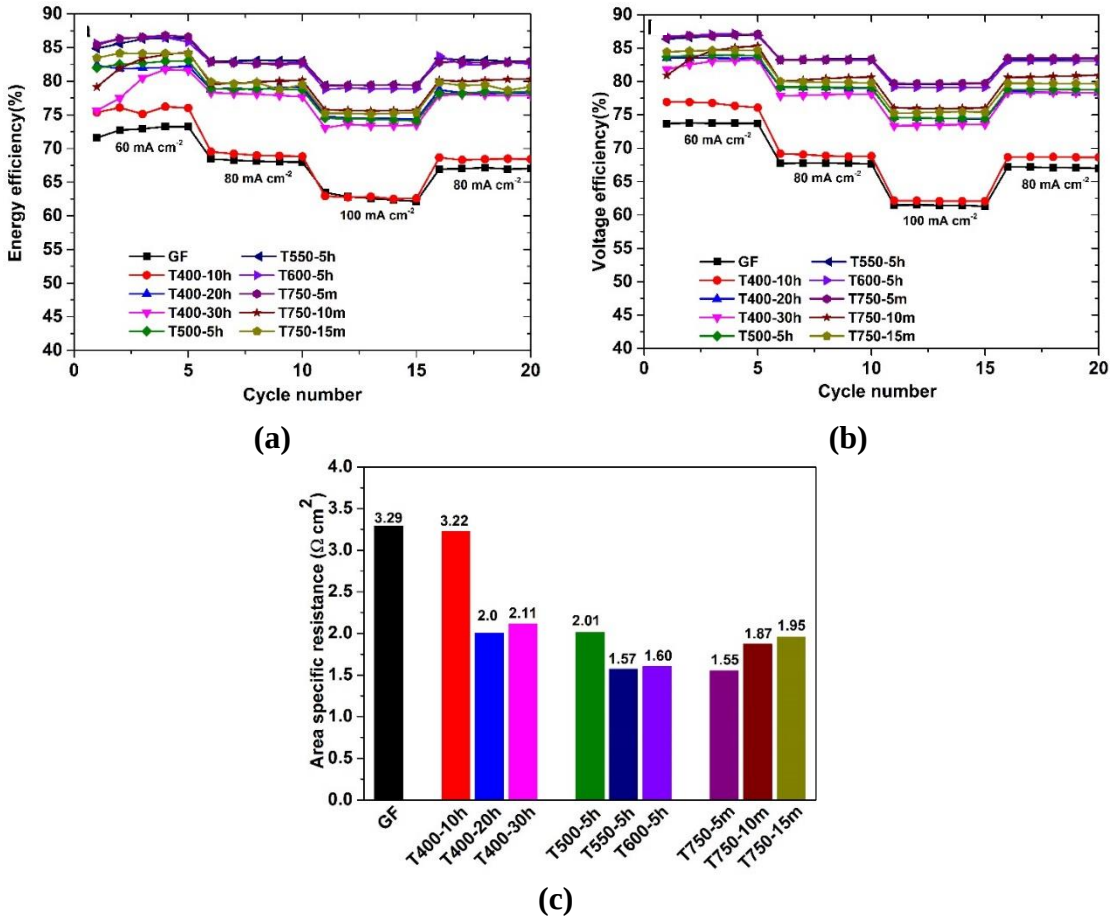

Figure 4.23 Performance of VRFB cell at various current densities (a) energy efficiency (b) voltage efficiency (c) area specific resistance.

The area specific resistance (ASR) represents the average wet cell resistance during cell cycling is a very effective method for comparing different cells. The average ASR (ρ) during the cell charging/discharging is calculated using the formula given below:

$$\rho = \frac{V_o(1 - VE)}{j(1 + VE)} \tag{4.1}$$

Where j_{app}, VE and V_{oc} represent the applied current density, voltage efficiency and average open circuit voltage during charging and discharging, which is the average open-circuit voltage (~ 1.38 V at 25°C) during charging and discharging, respectively. Minimum internal cell resistance is observed for the T750-5m, T550-5h and T600-5h electrodes, whereas the maximum is observed for GF and T400-10h. Since membrane resistance is the

same for the entire cell assembled, the internal change reflects the change in charge transfer resistance, which is perfectly in line with the charge transfer value obtained from EIS. The minimum value of Ra indicates the uniform flow distribution of the electrolyte across the electrode i.e. utilization of electrolyte effectively.

The flow is charged/discharged for 60 cycles at a constant current density of 80 mA cm^{-2} to acquire the information about the stability of the modified electrodes. The coulombic efficiency (CE), VE an EE are shown in Figure 4.24.

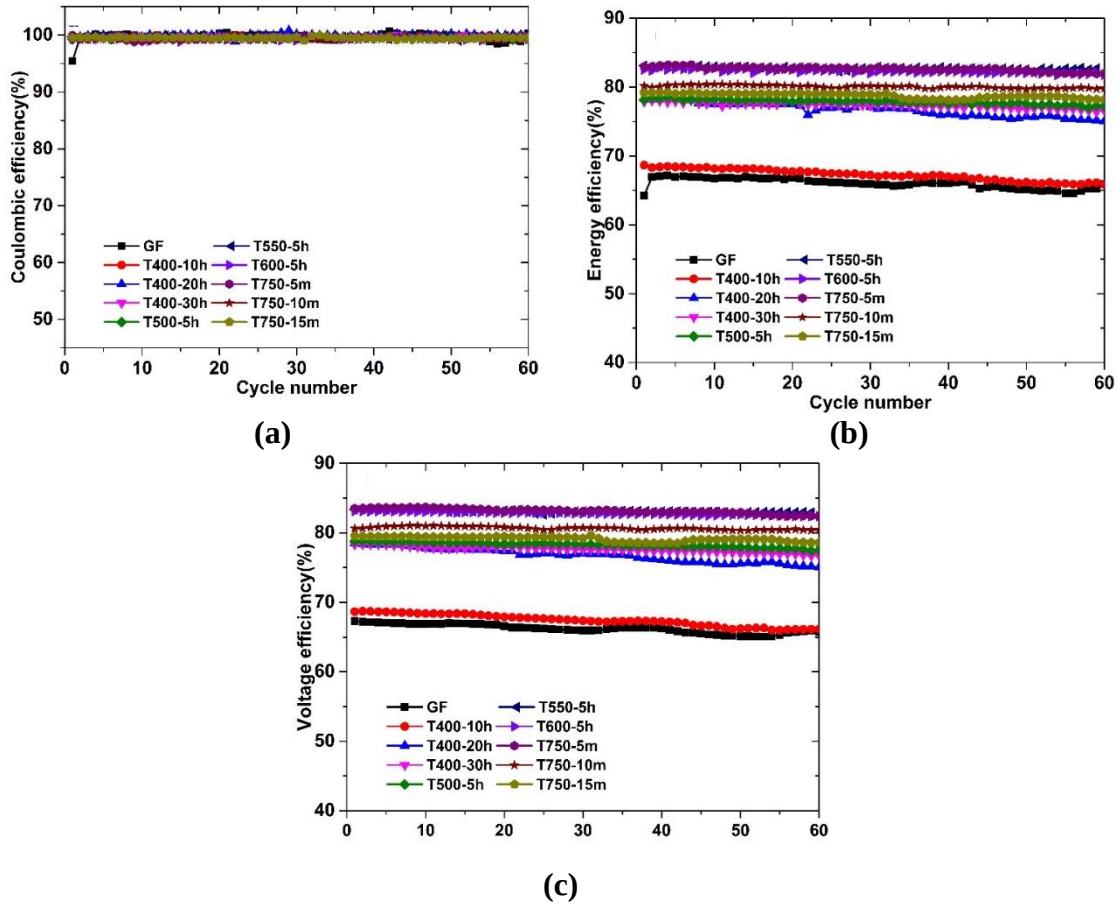

Figure 4.24 Cycling performance of VRB cell at 80 mA cm^{-2} for 60 cycles (a) Coulombic efficiency (b) energy efficiency (c) voltage efficiency.

Long term cycling tests (Figure 4.24) confirm the trends observed in the foregoing screening tests (Figure 4.23). There is no notable reduction in energy efficiency during extended cycling, suggesting that the beneficial effect of thermal treatment is preserved. The minor decrease in efficiency with progressive cycling is due to the crossover of active

species through the membrane and can be easily recovered by electrolyte rebalancing. As shown in Figure 4.25, the cell cycling results are consistent with the results obtained from the single electrode measurement and allow for an unambiguous correlation with the physical characterization.

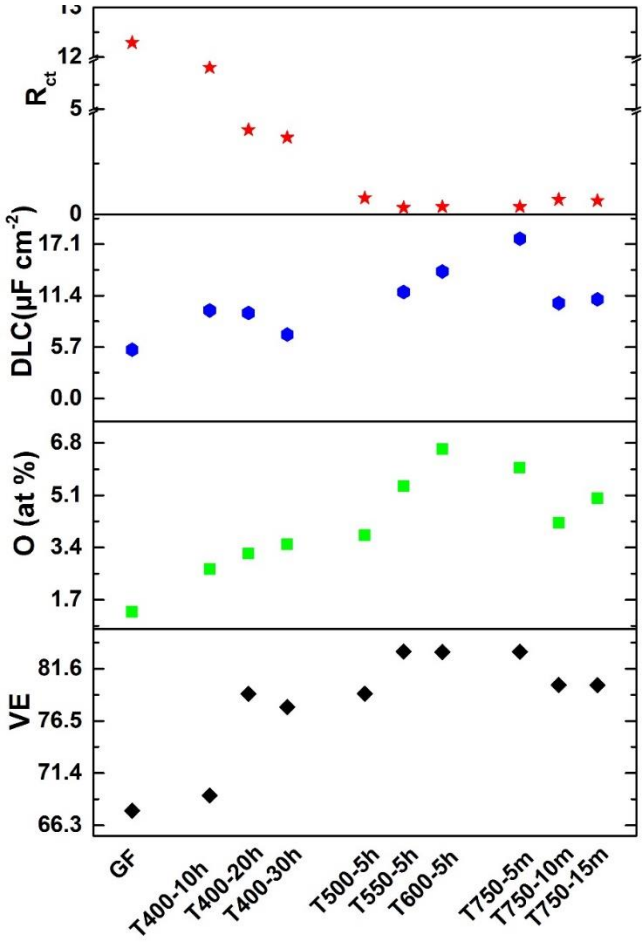

Figure 4.25 A graph showing the correlation between the VE at 80 mA cm^{-2}, oxygen content, DLC and charge transfer resistance.

The highest voltage efficiency is exhibited by T550-5h, T600-5h and T750-5m electrodes, respectively. They consist of a comparatively high amount of oxygen, which varies from 5.5% to 6.6%, although no clear preference for the C=O or C-O functional groups is observed. The defects ratio observed from Raman spectra follows the exact same trend as the ratio of oxygen content. This is relatable as oxidation takes place at the defect site of the graphitic structure [20]. In addition, this reflects the BET surface area value, which also exhibits the same trend. The impact of the defect site on the negative redox couple and the

overall cell performance shows similarity. Samples T550-5h, T600-5h and T750-5m are more electrochemically active as their peak potential difference is very low and their R_{ct} value is also lower compared to other samples investigated. The results from DLC measurements show an increase of defects per surface area for thermally treated electrode and are in good agreement with the cell performance. Hence, cell cycling results are in a good correlation with the results from the single electrode measurement, physical and spectroscopic measurement.

4.4 Titanium Carbide Decoration on the Electrode

An alternative method for improving the charge transfer kinetics is to deposit a catalyst onto the surface of the electrode. Catalyst deposition/doping is performed in order to improve the reactivity towards the redox reactions of the vanadium ions. The catalyst should be stable in acidic ambience, should not be susceptible to hydrogen evolution in the negative half-cell and must bind to fibre surface firmly without the aid of any binding agent. In addition to these properties, the most important parameter is its availability and cost-effectiveness. For these reasons, we select TiC as a catalyst to dope onto a graphite felt electrode.

This section presents a novel method for preparing binder-free, uniformly distributed titanium carbide (TiC) nanoparticles on graphite felt (GF) surfaces for use as a negative electrode in an all VRFB. The formation process of the TiC-particles at the carbon fibre surface involves two major steps: hydrothermal reaction and the formation of uniformly distributed TiO_2 particles on the carbon fibre surface and the subsequent transformation to TiC particles by carbothermal reaction according to Equation 4.2.

$$TiO2 + 3C \rightarrow TiC + 2CO\ (g) \qquad (4.2)$$

The presence of titanium has been confirmed by the EDX measurements (Figure 4.26).

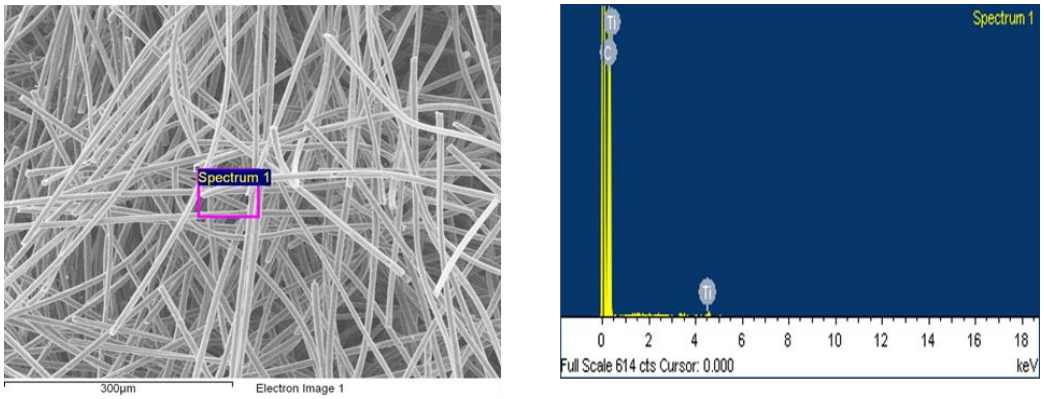

Figure 4.26 FESEM section and a corresponding EDX spectrum.

A schematic diagram representing the overall procedure for the formation of the TiC-GF is illustrated in Figure 4.27.

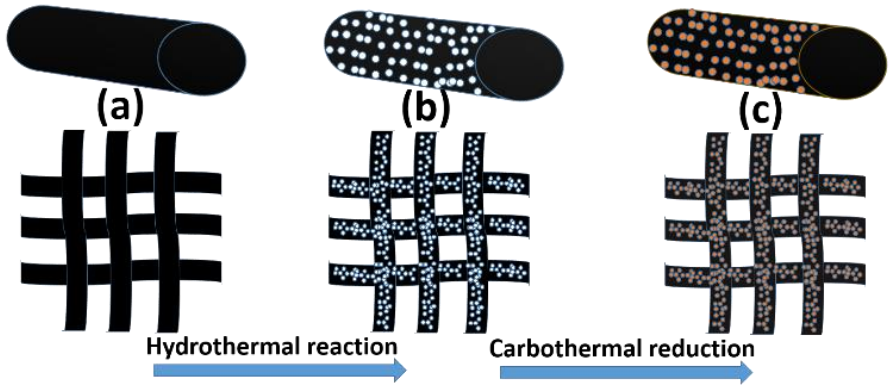

Figure 4.27 Schematic representation of the synthesis of TiC particles on the surface of graphite felt: (a) GF, (b) TiO_2-decorated GF, and (c) TiC-GF.

4.4.1 Morphological Changes After Deposition of Catalyst

The morphology of the pristine graphite felt (GF) and the TiC-modified felt (TiC-GF) are shown in Figure 4.28. As shown in Figure 4.28a and 4.28b, the pristine fibre exhibits a smooth texture typical of PAN-based carbon fibres (average fibre diameter of around 9 µm). Figure 4.28c and 4.28d show the TiC particles on the surface of the TiC-GF. It is observed that the particles are uniformly distributed across the fibre surface. The particle sizes, however, are rather non-uniform. This is most likely caused by the agglomeration of small TiC particles and/or sintering to larger entities. To further examine both the particle

size and crystal structure, HRTEM imaging has been performed and the results are shown in Figure 4.29.

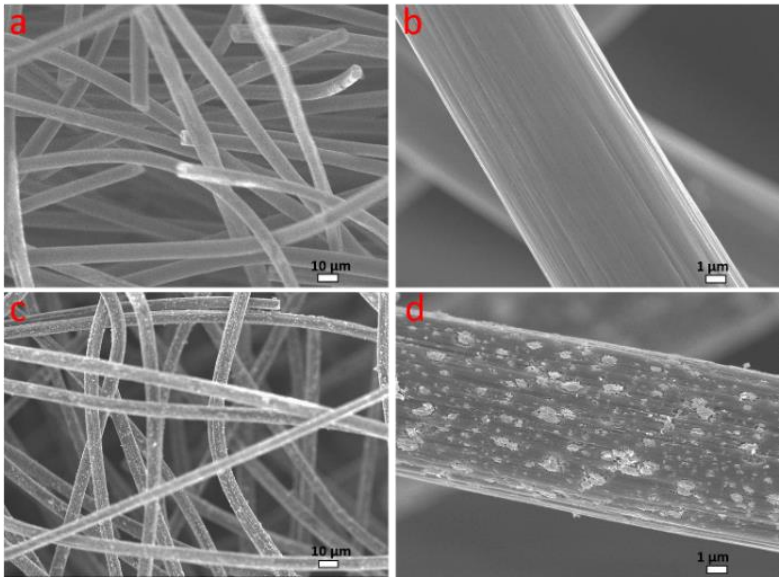

Figure 4.28 SEM image for GF (a-b), TiC-GF (c-d) at different magnifications.

HRTEM characterisation at different magnifications confirms the uniform particle distribution and variations in particles sizes (Figure 4.29a and 4.29b). Diffraction and fast-Fourier transform patterns (FFT) of the TiC particles (Figure 4.29c and 4.29d) reveal that the deposited particles possess a high crystallinity with a lattice fringed d-spacing of around 0.25 nm, corresponding to the (111) plane of the cubic-structured TiC.

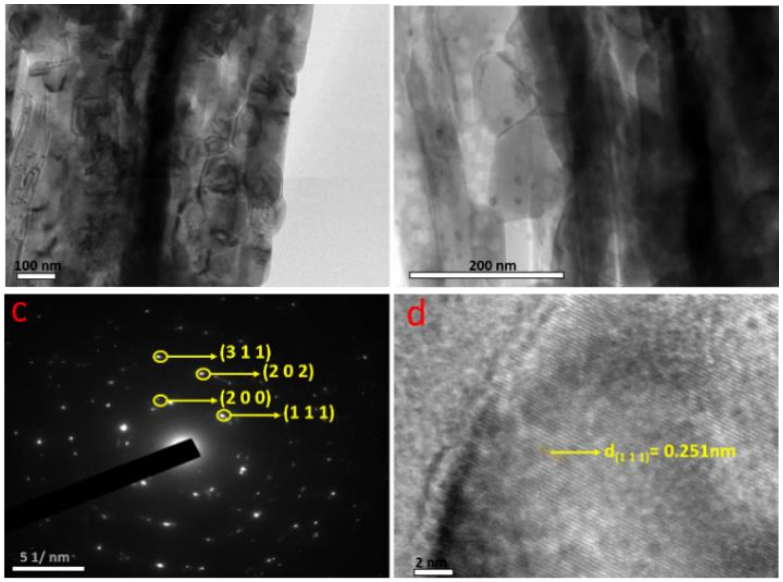

Figure 4.29 Typical HRTEM image (a-b), a diffraction pattern (c) and fast Fourier transform pattern (FFT) (d) of TiC particle at the carbon fibre surface.

4.4.2 Structural and Surface Chemistry Change

For the characterisation of structural and surface properties, analysis of the chemical structure and oxidation state of the TiC-GF, XRD and XPS have been performed. The XRD spectra of GF and Ti-GF are shown in Figure 4.30.

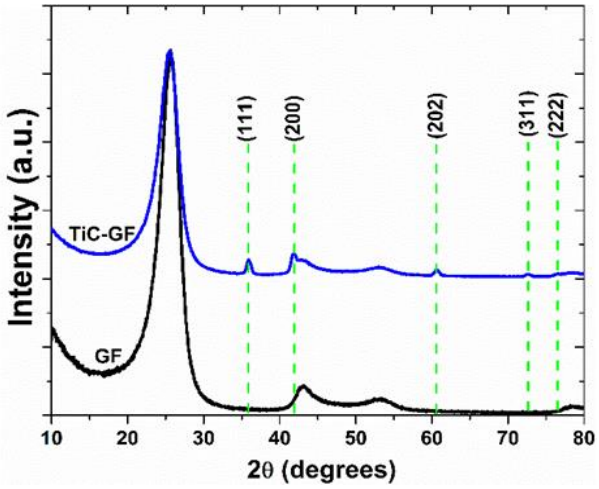

Figure 4.30 XRD spectra of the GF and TiC-GF.

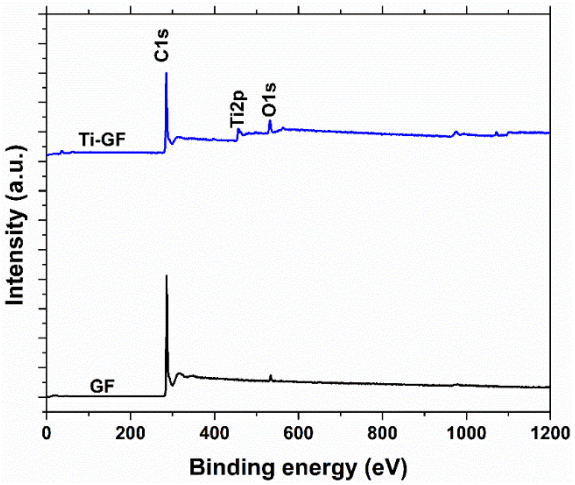

Figure 4.31 XPS survey spectra of pristine graphite felt and TiC decorated graphite felt.

The diffraction peak located at 25.6° and the other two peaks located at 43.2° and 53.3° are attributed to (002), (100) and (004) facets of the graphite. GF shows the three characteristic peaks, whereas TiC-GF exhibited additional diffraction peaks at 35.9°, 41.8°, 60.7°, 72.7°

and 76.7°, corresponding to (111), (200), (202), (311) and (222) planes of the TiC cubic phase (JCPDS:96-9506) respectively. XPS analysis reveals the presence of C, Ti and O for the TiC-GF (Figure 4.31).

High-resolution spectra of Ti and C are deconvoluted using Gaussian-Lorentz fitting to determine the chemical states. Peaks generated by spin-orbital interaction of Ti2p, resulting in the doublet $Ti2p_{3/2}$ and $Ti2p_{1/2}$, can be seen in Figure 4.32a. The multiple peaks obtained after the deconvolution can be assigned to TiC (455.3 eV, $Ti2p_{3/2}$), TiC (461.3 eV, $Ti2p_{1/2}$), TiO (456.6 to 457.5 eV) and TiO_2 (487.5 eV). The presence of TiO and TiO_2 is probably partial oxidation in ambient air exposed during sample handling and residual oxygen/water vapour in the deposition chamber. Similarly, the narrow spectrum of C1s presented in Figure 4.32b shows two peaks, one at 281.9 eV corresponding to the TiC bond and the other at 284.5 eV corresponding to the graphitic carbon [21-23].

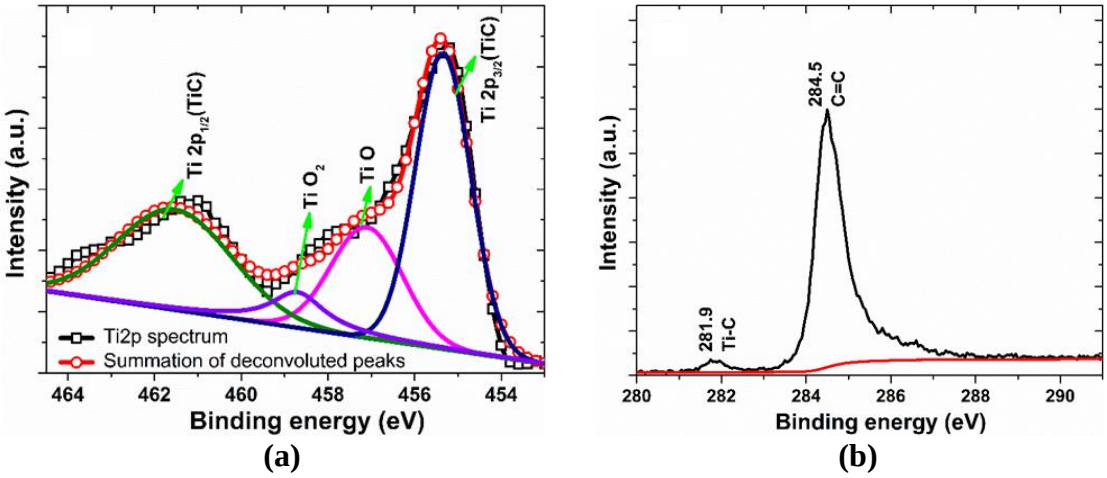

Figure 4.32 XPS spectra of TiC-GF (a) Ti-2p spectrum (b) C1s spectrum.

4.4.3 Electrochemical Properties of TiC Decorated Electrode

Figure 4.33a and 4.33b present the CV curves of the V^{2+}/V^{3+} redox couple on pristine and TiC-decorated electrodes. The electrochemical parameters obtained are summarised in Table 4.9.

The peak potential separation (ΔE_p), peak currents and their ratios (I_a/I_c) were used as figures of merit for the evaluation of the electrocatalytic activity. For the pristine electrode,

low oxidation and reduction currents are observed, which reflect the poor electrode reversibility towards the V^{2+}/V^{3+} redox couple.

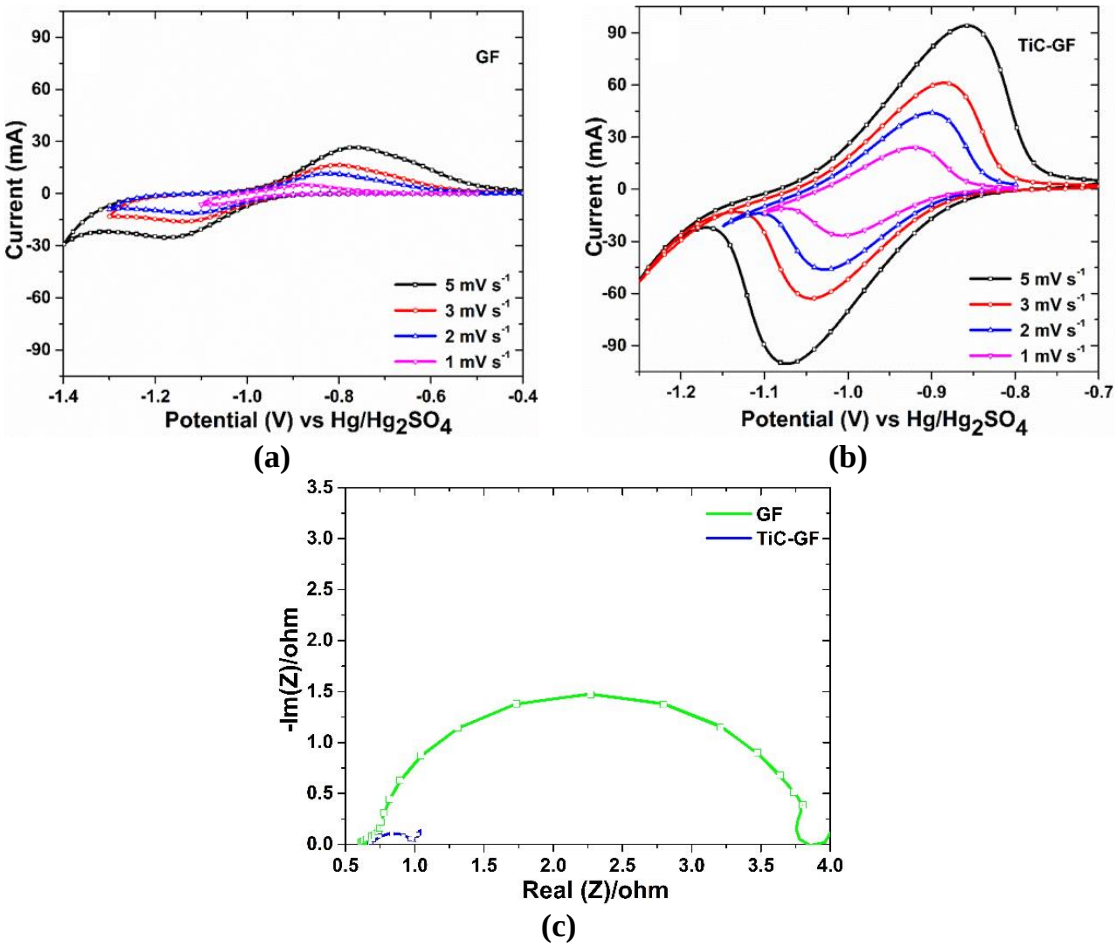

Figure 4.33 (a) CV of GF and (b) TiC-GF at different scan rates, and (c) Nyquist plot.

By contrast, the peak potential difference (ΔE_p) at a scan rate of 1 mV s^{-1} for TiC-GF is only 80 mV, which is substantially lower than for GF (ΔE_p=190 mV). Similarly, the peak current ratio is also lower for TiC-GF (I_a/I_c = 1.03) compared with GF (I_a/I_c = 1.25). The dramatic increase in peak current and a decrease in peak separation both furnish evidence for the substantially higher reversibility of the TiC-decorated electrode.

Figure 4.34 shows a linear relationship between the anodic and cathodic peak current and the square root of the scan rate, indicating that the redox reaction is limited by the diffusion within the given scan rate ranges. The slope for TiC-GF is larger than that of GF, which reflects the presence of a higher number of active sites [24, 25].

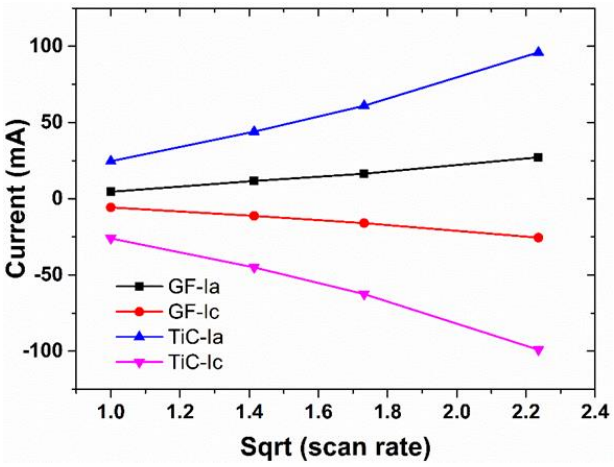

Figure 4.34 Plot of anodic and cathodic current vs square root of scan rate.

Table 4.9 Electrochemical parameter obtained from GF and TiC-GF electrode at different scan rates.

Scan rate (mV s^{-1})	GF		TiC-GF	
	ΔE_p(V)	I_a/I_c	ΔE_p(V)	I_a/I_c
5	0.41	1.06	0.22	1.03
3	0.34	1.03	0.16	1.02
2	0.28	1.04	0.13	1.02
1	0.19	1.25	0.08	1.03

Figure 4.33c shows the results of the EIS (Nyquist plot), carried at open circuit potential. With the introduction of TiC, the charge transfer resistance is decreased to 0.31 Ω. This is significantly lower compared to pristine GF (3.19 Ω) and is highly consistent with the CV results.

4.4.4 Single Cell Performance

Typical charge/discharge tests were performed using VRFB single cells to demonstrate the practical application of TiC-GF. Identical cells with GF and TiC-GF at the negative electrodes were assembled with a felt compression of 25%. The dry cell resistance was the same for both cells (approx. 0.15 Ω cm2), which clearly indicates that the modification has no noticeable effect on the (bulk) electronic conductivity. Stated otherwise, the differences in cell performance would be related to electrode kinetics. Energy efficiency and voltage efficiency from 60 to 100 mA cm^{-2} were plotted in Figure 4.35a and 4.35b.

At a current density of 100 mA cm^{-2}, a gain in the energy efficiency of 13% was observed by using a TiC-GF negative electrode instead of a virgin GF. A comparison of the voltage profile vs specific capacity (Ah L^{-1}) at a current density of 80 mA cm^{-2} is shown in Figure 4.35c. For the TiC-GF, significant shifts in the charge (-100 mV) and discharge (+170 mV) curves as compared to cells containing pristine GF as negative electrodes were observed. Under fixed cut-off voltages between 0.9 V to 1.65 V, the use of pristine GF negative electrode resulted in a relatively poor specific capacity of 4.3 Ah L^{-1}, which reflected the poor utilisation of electrolyte. With the introduction of TiC particles at the negative electrode, the specific capacity increased to 6.4 Ah L^{-1} (48% higher than that of GF). The TiC-GF exhibited a low charging voltage plateau and a high discharging plateau, signifying lower charging and higher discharging voltage. This led to a higher charge/discharge capacity within a given voltage window. It could also be assumed that the faster charge-transfer kinetics of the negative couple was accompanied by the suppression of the hydrogen evolution reaction (HER), which occurred as a parasitic side reaction at the negative electrode.

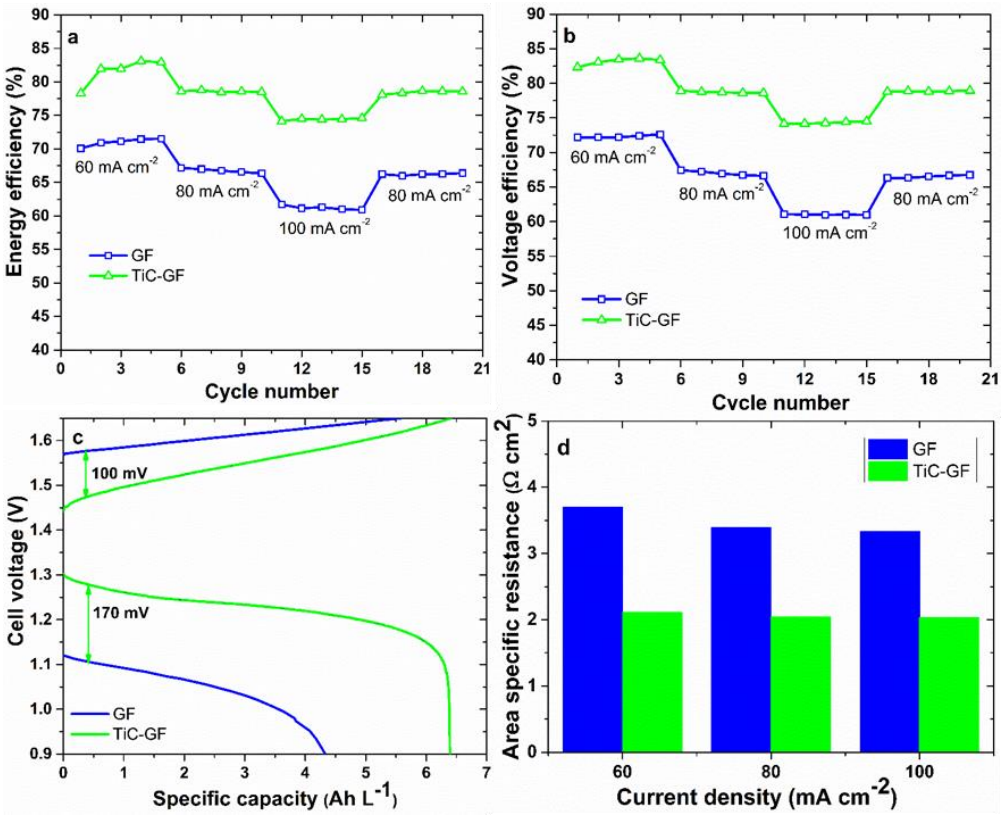

Figure 4.35 Comparison of energy efficiency (a), voltage efficiency (b), specific capacity at 80 mA cm^{-2} (c) and area specific resistance (d) of GF and TiC-GF.

Hence, the improved electrochemical properties of the TiC-GF could be unequivocally attributed to the presence of electronically conductive and catalytically active particles. Moreover, the nanometre-size particles generated a significantly higher surface area. Both effects contributed to the substantially higher reversibility of the V^{2+}/V^{3+} reaction at the TiC-GF electrode.

Figure 4.35d shows the area-specific resistance (ASR) at different current density levels. The ASR represents the average wet cell resistance of the cell during charging and discharging. The use of the TiC-GF as the negative electrode reduces the ASR by about 40%, which contributes to the effective utilisation of the electrolyte capacity.

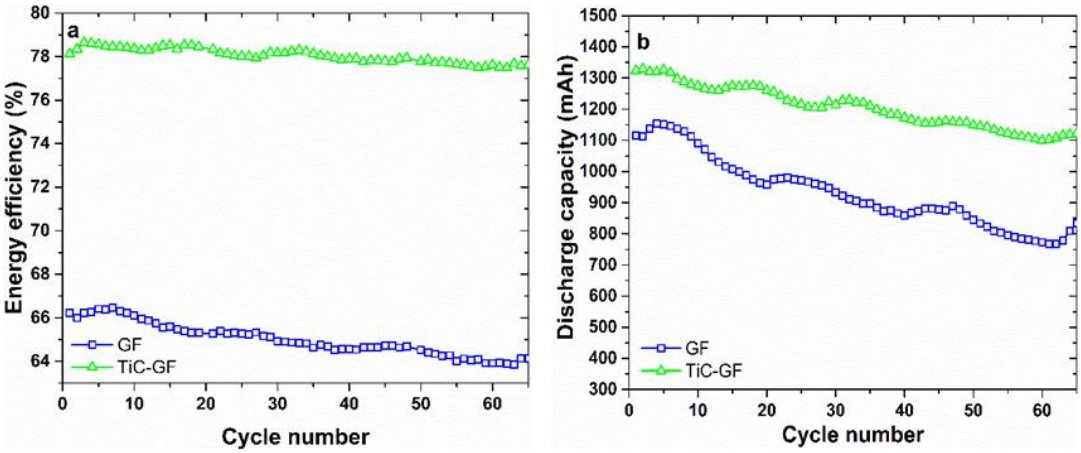

Figure 4.36 Cycling test of VRFBs: energy efficiency (a) and discharge capacity (b), at a current density of 80 mA cm^{-2} with GF and TiC-GF.

Catalyst stability during long-term operation is one of the critical issues for its use in the VRFB, as the catalyst needs to withstand the corrosive environment of the electrolyte and should not be flushed away by the flowing electrolyte. In order to test the stability of the TiC-GF, 65 consecutive charge-discharge cycles have been conducted at a current density of 80 mA cm^{-2}. Figure 4.36a and 4.36b show the corresponding energy efficiency and discharge capacity of the pristine GF and TiC-GF. The TiC-GF adds 13% to the energy efficiency as compared to GF. The small drop in efficiency during cycling is caused by a net electrolyte transfer from the positive to the negative tank, which is commonly observed

when using anion exchange membranes. Similarly, the discharge capacity of the VRFB with a TiC-GF shows 84% of the initial capacity after 65 cycles with a capacity decay of 3.33 mAh per cycle. By contrast, the cell using the pristine GF as the negative electrode maintained only 70% of the initial capacity after 65 cycles and the capacity loss is also significantly higher (around 5.3 mAh per cycle). This once again highlights the excellent stability and electrochemical performance of a TiC-GF negative electrode.

4.4.5 Proposed Mechanism of the Catalytic Effect

The investigations verify that the use of GF containing TiC nanoparticles as the negative electrode in VRFB increases the overall efficiency of the VRFB. This increase in performance is solely attributed to the enhanced reversibility of the TiC-GF negative electrode. A possible mechanism of the catalytic effect of TiC particles is proposed and shown in Figure 4.37, based on the early study conducted by Skyllas-Kazacos et al [19]. Initially, ion exchange occurs between the hydrogen ion of TiC-O-H and a V^{2+} during charging and V^{3+} is absorbed to the Ti-C-O-H layer. Secondly, V^{3+} ions are reduced to V^{2+} as electrons transfer from Ti-C-V(II) complex to Ti-C-V(I). Finally, the V(I) complex turns to V^{2+} (desorption process). During discharge, the reaction occurs in the opposite direction.

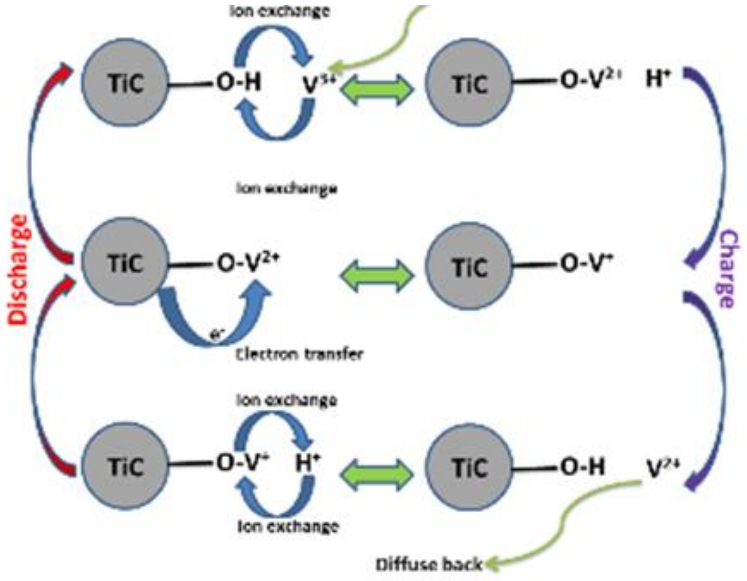

Figure 4.37 Proposed mechanism of V^{2+}/V^{3+} redox reaction in the presence of TiC particles.

4.5 Summary of the Chapter

In this chapter, the physical and electrochemical properties of the graphite felt electrodes used in VRFB have been investigated. The specific problem related to reproducibility of as-received electrodes from different batches, the requirement of electrode activation in each half-cell and the ways to optimally activating the electrodes have been addressed. The major findings are briefly summarized below.

Electrode activation was required to enhance the reaction kinetics of VRFB. Prior to electrode activation study, it was necessary to investigate the reproducibility of the as-received electrodes. It was decided that samples from three different batches should be characterized to observe the physical and electrochemical reproducibility. The results showed the as-received electrodes having the same physical and electrochemical properties.

The electrode performance was investigated with respect to each half-cell. The determination of overpotential at each-half cell was performed through the polarization curve with the aid of a special experimental setup. The study confirmed that thermal activation of the electrode could improve the negative half-cell only. However, for the positive half-cell, thermal activation would impede the reaction mechanism. Subsequently, all of the thermal activation of electrodes was directed towards evaluating its performance with respect to the negative half-cell. A series of temperature and time were chosen based on the thermogravimetric analysis of the electrode material. Various physical and electrochemical characterization techniques along with cell cycling test were employed to identify the crucial electrode properties, such as surface chemistry, specific surface area, surface defects, wetting properties, etc. The benefits with respect to the electrochemical characteristics could not be attributed to the presence of singular surface oxygen complexes. On the contrary, a clear correlation between the double layer capacitance, which measured the density of highly reactive edge planes or defects, and the cell performance could be verified. Out of various samples examined, the sample treated at 750°C for 5 minutes showed the most favourable effect.

As an alternative method to enhance the reaction kinetics and the long-term stability of the electrode, a binder-free TiC decorated electrode was synthesized. TiC particles were

synthesized directly on the surface of the graphite felt by a two-step process. In the first step, TiO_2 particles on the graphite felt surface were prepared using the hydrothermal method. The sample after the hydrothermal method was then transferred to a furnace to undergo carbothermal reaction under an argon atmosphere at 1250°C. Cyclic voltammetry (CV) and electrochemical impedance spectroscopy (EIS) confirmed the catalytic effect of TiC towards the negative redox couple (V^{2+}/V^{3+}). The TiC-decorated electrode, when used in the negative half-cell of a VRFB, enabled high electrolyte utilization resulting in increased energy efficiency. It exhibited a 13.3 % increase in energy efficiency at a current density of 100 mA cm^{-2}, compared to the pristine electrode. Moreover, it showed excellent stability with high capacity retention over repetitive cycling. These results suggested that low-cost binder-free, uniformly distributed TiC particles on the electrode surface could constitute a high-performance negative electrode for VRFBs.

References

[1] T.J. Rabbow, M. Trampert, P. Pokorny, P. Binder, A.H. Whitehead, *Electrochimica Acta*, **2015**, 173, 17-23.

[2] E. Agar, C. Dennison, K. Knehr, E. Kumbur, *Journal of Power Sources*, **2013**, 225, 89-94.

[3] H. Fink, J. Friedl, U. Stimming, *The Journal of Physical Chemistry C*, **2016**, 120, 15893-15901.

[4] R. Schweiss, C. Meiser, F.W.T. Goh, *ChemElectroChem*, **2017**, 4, 1969-1974.

[5] K. Horie, M. Hiromichi, I. Mita, *Fibre Science and Technology*, **1976, 9,** 253-264.

[6] Z. Yue, W. Jiang, L. Wang, S. Gardner, C. Pittman Jr, *Carbon*, **1999**, 37, 1785-1796.

[7] F. Tuinstra, J.L. Koenig, *The Journal of Chemical Physics*, **1970**, 53, 1126-1130.

[8] B. Dippel, H. Jander, J. Heintzenberg, *Physical Chemistry Chemical Physics*, **1999**, 1, 4707-4712.

[9] P. Blake, P. Blake, EW Hill, AH Castro Neto, KS Novoselov, D. Jiang, R. Yang, TJ Booth, and AK Geim, *Applied Physical Letter*, **2007**, 91, 063124.

[10] M. Baldan, E. Almeida, A. Azevedo, E. Goncalves, M. Rezende, N. Ferreira, *Applied Surface Science*, **2007**, 254, 600-603.

[11] T.J. Rabbow, A.H. Whitehead, *Carbon*, **2017**, 111, 782-788.

[12] J.P. Randin, E. Yeager, *Journal of the Electrochemical Society*, **1971**, 118, 711-714.

[13] J.-P. Randin, E. Yeager, *Journal of Electroanalytical Chemistry and Interfacial Electrochemistry*, **1972**, 36, 257-276.

[14] J.-P. Randin, E. Yeager, *Journal of Electroanalytical Chemistry and Interfacial Electrochemistry*, **1975**, 58, 313-322.

[15] H. Gerischer, R. McIntyre, D. Scherson, W. Storck, *Journal of Physical Chemistry*, **1987**, 91, 1930-1935.

[16] B. Rand, R. Robinson, *Carbon*, **1977**, 15, 257-263.

[17] E.H. Lock, D.Y. Petrovykh, P. Mack, T. Carney, R.G. White, S.G. Walton, R.F. Fernsler, *Langmuir*, **2010**, 26, 8857-8868.

[18] E. Desimoni, G. Casella, A. Morone, A. Salvi, *Surface and Interface Analysis*, **1990**, 15, 627-634.

[19] B. Sun, M. Skyllas-Kazacos, *Electrochimica Acta*, **1992**, 37, 2459-2465.

[20] X. Chu, L. Schmidt, *Surface science*, **1992**, 268, 325-332.

[21] L. Ramos-Rivera, D. Escobar, V. Benavides-Palacios, P. Arango, E. Restrepo-Parra, *Condensed Matter*, **2012**, 407,3248-3251.

[22] M.-P. Delplancke-Ogletree, O.R. Monteiro, *Journal of Vacuum Science & Technology A: Vacuum, Surfaces, and Films*, **1997**, 15, 1943-1950.

[23] A.E. Kaloyeros, W.S. Williams, C.M. Allocca, D.M. Pollina, G.S. Girolami, *Advanced Ceramic Materials*, **1987**, 2.

[24] S. Park, H. Kim, *Journal of Materials Chemistry A*, **2015**, 3, 12276-12283.

[25] J.-H. Kim, K.J. Kim, M.-S. Park, N.J. Lee, U. Hwang, H. Kim, Y.-J. Kim, *Electrochemistry Communications*, **2011**, 13, 997-1000.

Chapter 5

In-situ Investigation of the Reactant Conversion and Performance of Each Half-cell

This chapter discusses the techniques to perform the in-situ study of the cell including the study outcomes. The first section introduces the segmented cell approach to predict the flow behaviour and the reactant conversion in a single pass using the local OCV. This is a novel technique to quantify the electrolyte utilization using the difference in experimental and theoretical SOC in VRFB. The segmented cell results are verified by comparing the single cell results at the different compression level of the electrodes. The other section reports the in-situ overpotential measurement at each half of the cell at different operating conditions, such as electrode type, flow rate of electrolyte, flow configuration, electrolyte concentration etc. The chapter also includes the determination of overpotential at each half-cell using the reference electrode at various operating conditions.

A part of the findings in this section was published as an original research paper:

-Ghimire, Purna C., Arjun Bhattarai, Rüdiger Schweiss, Günther G. Scherer, Nyunt Wai, and Qingyu Yan. "A comprehensive study of electrode compression effects in all-vanadium redox flow batteries including locally resolved measurements." Applied Energy 230 (2018): 974-982.

-Ghimire, Purna, Arjun Bhattarai, Rüdiger Schweiss, Günther Scherer, Nyunt Wai, Tuti Lim, and Qingyu Yan. "Investigation of Reactant Conversion in the Vanadium Redox Flow Battery Using Spatially-Resolved State of Charge Mapping." Batteries, no. 1 (2019): 2.

5.1 Spatially Resolved Study for the Investigation of Flow Visualization and Reactant Conversion Using Segmented Cell

The objective of this study is to investigate the method to visualize the flow distribution and amount of reactant conversion across the electrode using local current or voltage distribution. Segmented cell study is very scarce in VRFBs. The approach undertaken and the method of prediction of reactant conversion is new in the area of the flow battery. The configuration, experimental detail and measurement procedure is provided in section 2.6.1 and 3.6. For the ease of understanding and smooth following of subsequent sections, the position and flow direction of the segments are given in Figure 5.1.

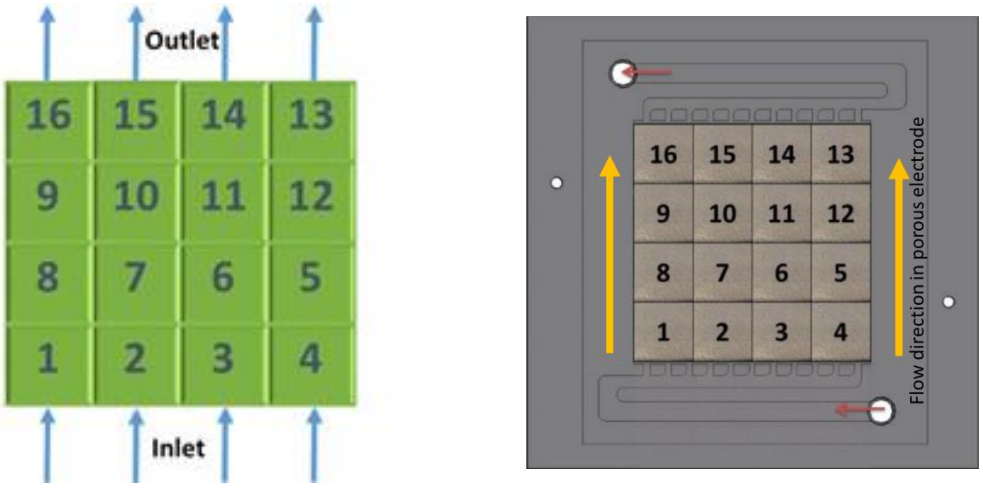

Figure 5.1 Position of 16 segments with the flow direction of the electrolyte.

5.1.1 OCV for the Visualization of the Flow Distribution Across the Electrolyte

Most of the segmentation in batteries/fuel cells have been performed with the divided current collector and/or together with a divided bipolar plate. The porous electrode in most of the study is non- segmented as dividing the porous electrode is extremely difficult and might affect the flow distribution of reactants. In a segmented cell study, there is always a chance that a local segment might see minor current/voltage flowing from the neighbouring segments because of the use of a non-segmented electrode. The lateral flow of current increases once the thickness of the undivided electrode increases. This is because the local current or voltage might equilibrate quickly within the planer surface in a thicker porous

felt as through-plane conductivity of electrode is several times less than the in-plane conductivity. This might be a reason that the segmented cell study is rare in flow batteries, which on the other hand is widely used in the fuel cell.

Figure 5.2a and 5.2b show the contour diagram during the 1-minute discharge at a current density of 160 mA cm^{-2}, which is obtained by averaging the 1 minute discharge data. During the discharge, the electrolyte stoichiometry (λ) was 2.5 and 1, respectively. The separation of the local discharge voltage between flow inlet and the outlet is observed during discharging as shown in Figure 5.2a and 5.2b, respectively. During discharging, the voltage is maximum at the inlet and minimum at the outlet, which is because of the depletion of the charged species towards the flow outlet. Similarly, during charging, the voltage is maximum at the outlet and minimum at the inlet, which is because the concentration of the charged species increases as the electrolyte reaches the outlet. This has been already been thoroughly explained in previous work [1].

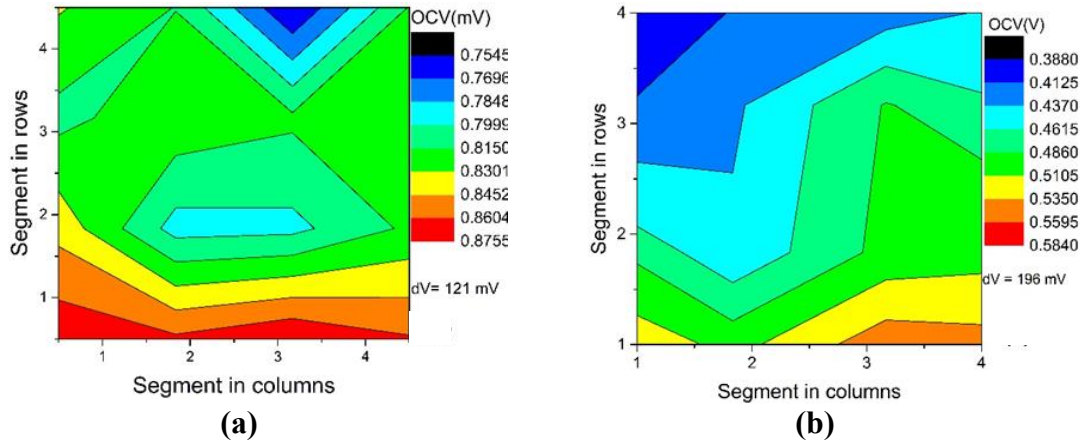

Figure 5.2 Contour diagram of discharge voltage at (a) flow rate = 60 mL min^{-1}, j = 160 mA cm^{-2} and (b) flow rate = 20 mL min^{-1}, j = 160 mA cm^{-2} [1].

The lateral flow of current can mislead the information gained locally. As a thicker non-segmented electrode is used, it is expected that the resolution of the local effect will be further low. For example, in Figure 5.2, although we see the difference voltage between inlet and outlet segments, the resolution is not clear enough to draw any conclusion. Therefore, to overcome this problem, a method to study the flow distribution by analyzing the open circuit voltage (OCV) immediately after the terminating the charge or discharge

process is very useful. The OCV sooner after the termination of charge or discharge can be used to predict the in-situ behaviour during current flow.

Figure 5.3a shows an OCV profile of sixteen segments against time after the termination of discharge at the current density of 80 mA cm^{-2}. Wide separation of OCV is obtained due to the segmentation, which equilibrates eventually. The equilibration time is a function of the flow rate and current density.

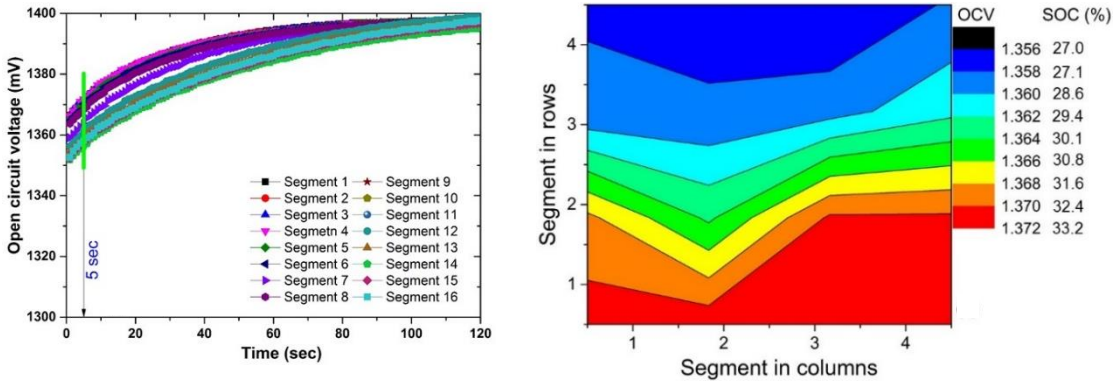

Figure 5.3 (a) OCV vs time curve after terminating the discharge at 80 mA cm^{-2} and (b) the corresponding contour diagram at 5 s in OCV after termination. The flow rate was 42 mL min^{-1}.

In a conventional design of flow cells employing a thick porous electrode, the voltage contour is often distorted by lateral flow of current. Hence, it is difficult to capture any clear pattern even at very high current densities. By investigating OCV contours immediately after termination of discharge (shown in Figure 5.3b), a clear voltage separation between inlet and outlet is obtained even at a low current density of 80 mA cm^{-2}. We attribute this to the absence of current flow in OCV.

5.1.2 Prediction of Reactants Conversion by Changing OCV to Corresponding SOC Values

As shown in Figure 5.3b, the corresponding SOC is calculated from the OCV, which is also indicated in the contour diagram. The OCV data at 5 s after the termination of discharge provide the best resolution in avoiding noise from the battery tester (temporal resolution of the tester was 1s). The stoichiometry is calculated from Faraday's law:

$$\lambda = \frac{Q_{app}}{Q_{st}} = Q_{app} \cdot \frac{nF \cdot c_V \cdot SoC}{I} \quad (5.1)$$

Where Q_{app} is the applied flow rate, Q_{st} is the stoichiometric flow rate at specific current density, I is the total current, SOC is the state of charge (0.5), c_v is the total concentration of the vanadium ions, n is the number of electrons involved in the redox reaction (here n = 1) and F is Faraday's constant (96485 As mol^{-1}).

In order to investigate the utilization of the electrolyte during discharge at high current density, the ΔSOC obtained experimentally (ΔSOC_{exp}) is compared with the theoretically expected change in SOC (ΔSOC_{th}) during a single pass of the electrolyte. ΔSOC_{th} corresponds to for full conversion during a single pass and is calculated using Faraday's law:

$$\Delta SOC_{th} = \frac{I}{Q_{app} c_v F} \quad (5.2)$$

ΔSOC_{exp} is determined by taking the difference between the electrolyte SOC at the inlet to the cell (i.e. SOC of the electrolyte in the tank) and at the outlet segments (i.e. SOC at outlet segments – 13, 14, 15 and 16). As shown in Table 5.1, the difference ΔSOC_{th} and ΔSOC_{exp} reflects different situations with respect to the conversion efficiency.

Table 5.1 Different performance characteristics described by the SOC changes (ΔSOC_{th} and ΔSOC_{exp}).

Case		Interpretation
(i)	$\Delta SOC_{exp} \approx \Delta SOC_{th}$	Optimum utilization of electrolyte and excellent flow distribution
(ii)	$\Delta SOC_{exp} >> \Delta SOC_{th}$	Poor utilization (higher overpotential either due to over-discharge at the retarded/stagnant zone or higher contact resistance)
(iii)	$\Delta SOC_{exp} << \Delta SOC_{th}$	Insufficient availability of redox species to sustain the applied current

5.1.3 Validation of the Reactant Conversion with the Aid of Compression Study of the Cell

For the experimental verification of the three different cases presented in subsection 5.1.2, the study of electrode compression has been performed. The cell cycling at six different compression levels of the porous electrode (15%, 20%, 25%, 30% 35% and 40%) have been investigated. The optimized electrode compression level is determined considering

all the factors like efficiencies and pressure drop. Only three compression levels of the electrode (15%, 25% and 40%) are undertaken for the segmented study due to the limitation of the cell design. Nevertheless, the three variations of electrode compression are sufficient to distinguish the different reactant conversion scenarios, as it consists of low, medium and high electrode compression in conventional VRFBs.

5.1.3.1 Spatially Resolved Study at Different Electrode Compression Levels

Figure 5.4 shows the OCV contours at 5s after the termination of discharge at the current density of 150 mA cm^{-2} for three electrode compressions. The plots from top to bottom represent the contour with an increase in electrode compression, whereas the left and right contours are plotted for measurements at the flow rates of 25 and 60 mL min^{-1}, respectively.

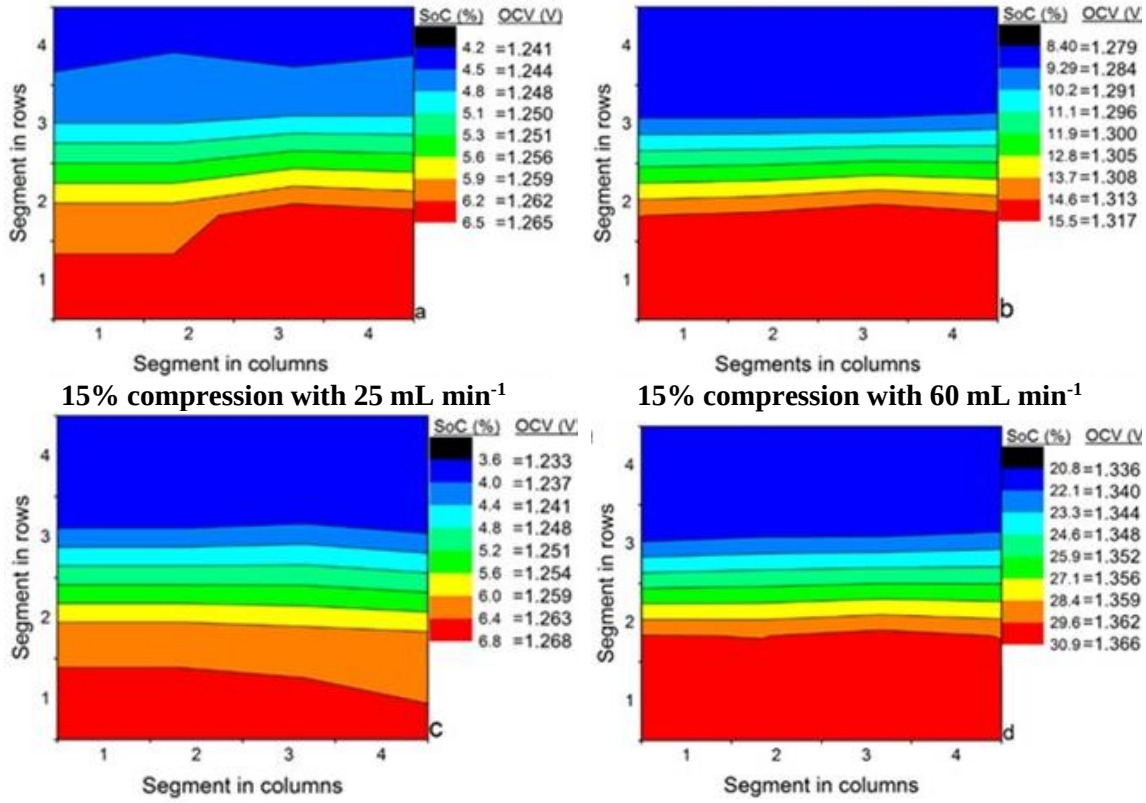

15% compression with 25 mL min^{-1} **15% compression with 60 mL min^{-1}**

25% compression with 25 mL min^{-1} **25% compression with 60 mL min^{-1}**

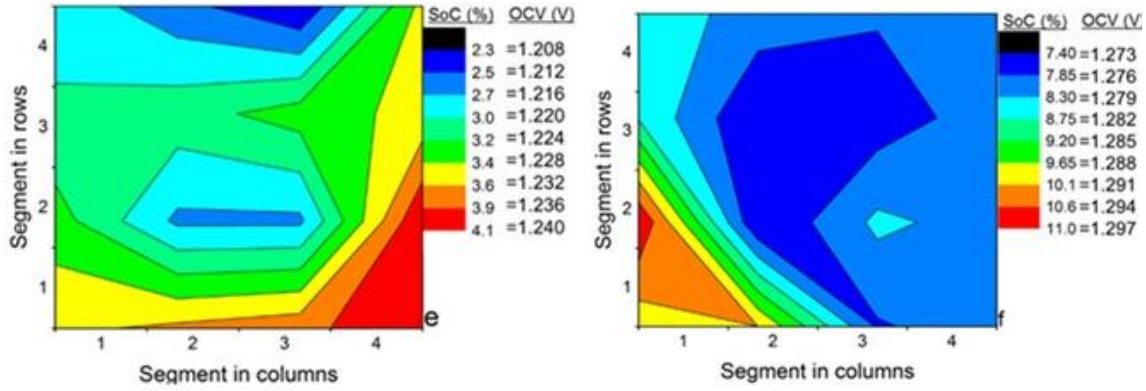

40% compression with 25 mL min^{-1} **40% compression with 60 mL min^{-1}**

Figure 5.4 SOC with the corresponding OCV on the legend contours. All the contours were measured 5s after the termination of discharge at 150 mA cm^{-2}.

If the OCV is measured immediately after terminating the discharge process, a higher voltage at the inlet segment and a lower voltage at the outlet segment is expected, as the charged species are depleted in the direction of flow. For a uniform flow distribution, a flat (band-like) distribution of the voltage along the cross-section of the flow can be assumed. The width of each contour diagram in Figure 5.4 is created using the contour profile function in the Origin pro software. It shows that the voltage gradient rather than single segment colour is the best to visualize the flow distribution profile. The raw voltage for the plot of Figure 5.4a is provided in Table 5.2. As revealed in Figure 5.4a-d, a uniform band of SOC (or OCV) along the cross section of the electrode is observed for the compression of 15% (a and b) and 25% (c and d) at both flow rates of 25 mL min^{-1} (a and c) and 60 mL min^{-1} (b and d). However, when the electrode compression is increased to 40%, the SOC patterns indicate a non-uniform flow distribution. Again, this reflects the fact that a higher electrode compression decreases the porosity (probably non-uniform change in porosity in a thick felt of large area), resulting in the flow of electrolyte through a particular section of the electrode or even short-circuiting of the electrolyte. Therefore, a high voltage (or SOC) band appears in the area with access to electrolyte flow, whereas a low voltage band appears in the area with depleted reactants. The SOC contour also depicts the utilization of electrolyte along the flow path. In other words, the distribution of the electrolyte through the porous electrode can be quantified by monitoring the ΔSOC.

Table 5.2 shows a comparison of the theoretical and experimentally determined ΔSOC during a single pass at stoichiometry values of λ=1 and λ=2.5, respectively.

Table 5.2 Theoretical and experimental conversion (SOC change) for different electrode compressions for cases shown in Figure 5.4.

Electrode compression	ΔSOC (60 mL min^{-1}, λ=2.5)	ΔSOC (25 mL min^{-1}, λ=1.0)
Theoretical	*19.43%*	*46.66%*
15%	30.09%	38. 93%
25%	20.9%	38.55%
40%	37.82%	40.98%

At a low flow rate of 25 mL min^{-1}, the experimental ΔSOC (ΔSOC_{exp}) value is found to be lower than the theoretical ΔSOC (ΔSOC_{th}). This is an indication that the segments near the outlet cannot sustain the current for a long period during discharge. At a high flow rate (60 mL min^{-1}), the experimental and theoretical ΔSOC match closely for 25% compression. This indicates that the electrolyte conversion in a single pass occurred at the predicted rate. At a value of 15% compression, the contact resistance is higher compared to other compression values, resulting in a higher SOC difference between the inlet the outlet. Therefore, the value of the ΔSOC_{exp} is much higher than the value of the ΔSOC_{th}. At 40% compression, the electrolyte fully discharges at the location where the electrolyte is trapped or stagnant or retarded flow occurred within the porous electrode. This again resulted in a higher ΔSOC value measured than the theoretical value. From the segmented cell approach, it becomes clear that a value of 25% electrode compression is an optimal trade-off between minimizing the contact resistance and maximizing the flow distribution.

5.1.3.2 Optimum Electrode Compression for the Non-segmented Cell

For verification of the results obtained from the segmented cell, the non-segmented cell cycling experiment has been carried out to obtain the optimum electrode compression. Figures 5.5a-d compare the coulombic efficiency (CE), energy efficiency (EE), voltage efficiency (VE) and discharge capacity (in mAh) at six different levels of electrode compression, respectively.

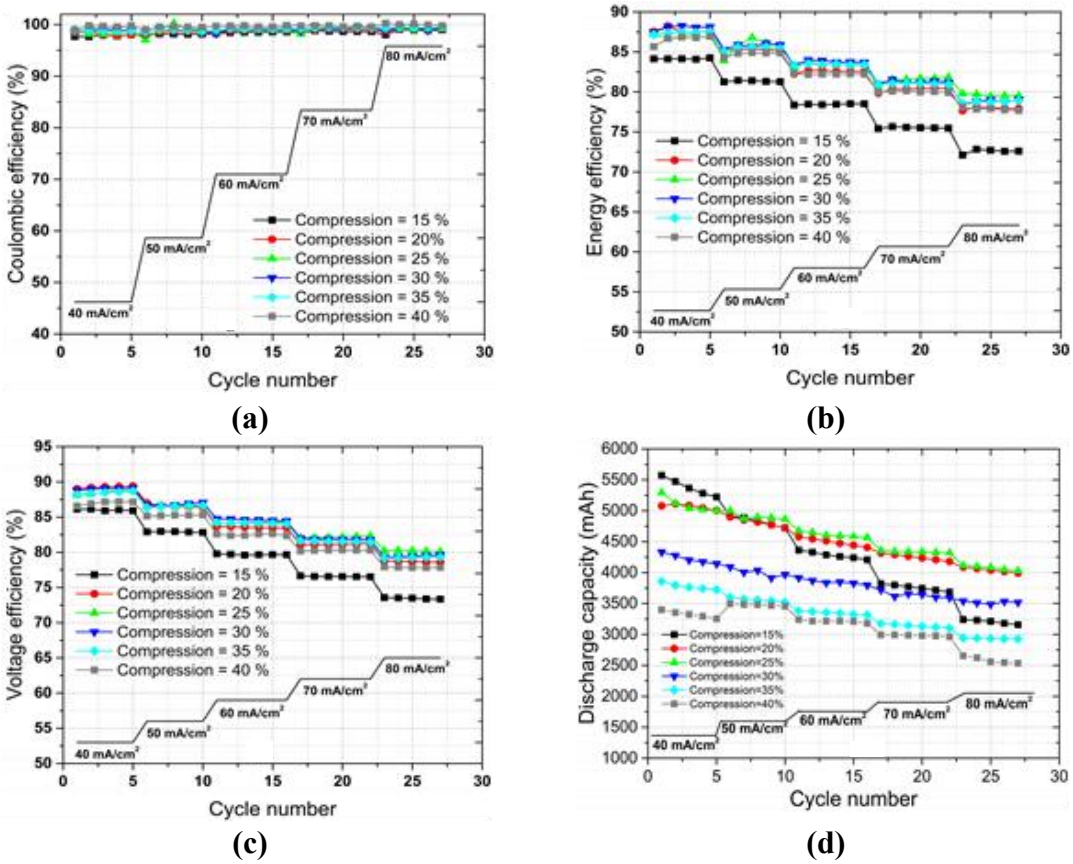

Figure 5.5 Comparision of: (a) coulombic efficiency, (b) energy efficiency, (c) voltage efficiency and (d) discharge capacity for different electrode compression levels.

The value of the CE is almost the same for all of the compression levels. This is expected, as CE is not influenced by the electrode, rather it is the properties of the membrane. The electrode with 15% compression of the electrode exhibits the least VE and EE due to high contact resistance. To get the reflectance of the contact resistance, the dry cell resistance for the various electrode compression is measured.

Table 5.3 Electronic resistance of 'dry' cells (w/o membrane) at various electrode compressions.

Electrode compression (%)	**15**	**20**	**25**	**30**	**35**	**40**
Electronic resistance (Ω cm^2)	1.1	0.78	0.75	0.72	0.61	0.58

As expected, the increase in the compression of the electrode results in a decrease in Ohmic resistance. A closer look at the six different compression values reveals a sharp drop of the electronic resistance between 15% and 20%, followed by a slight reduction in contact

resistance with a further increase in electrode compression. The trend observed is highly consistent with a previous study [3]. Hence, the poor energy and voltage efficiency at a value of 15% electrode compression are predominantly caused by poor interfacial contact between the felt and the BP. The highest EE and VE are found for an electrode compression of between 25% and 30%. This could be an indication that the cell performance cannot be improved by reducing contact resistance alone. At higher current densities, the effects of mass transport need to be considered.

Figure 5.5d shows the discharge capacity during cycling from 40 to 80 mA cm^{-2} at different electrode compression levels. The results show that capacity drops continuously as the cycling progresses, which is mainly due to the evolving electrolyte imbalance. The drop is pronounced with increasing current density due to the increased iR drop.

To scrutinize the effects on long-term cell performance, fifty cycles are run at a current density of 40 mA cm^{-2}. The completion of 50 cycles took almost 60 hours with the given volume of electrolyte, which is why it is referred to as long term cycling. The energy efficiency (EE) and discharge energy (DE) at various electrode compressions are compared and shown in Figure 5.6a and 5.6b, respectively.

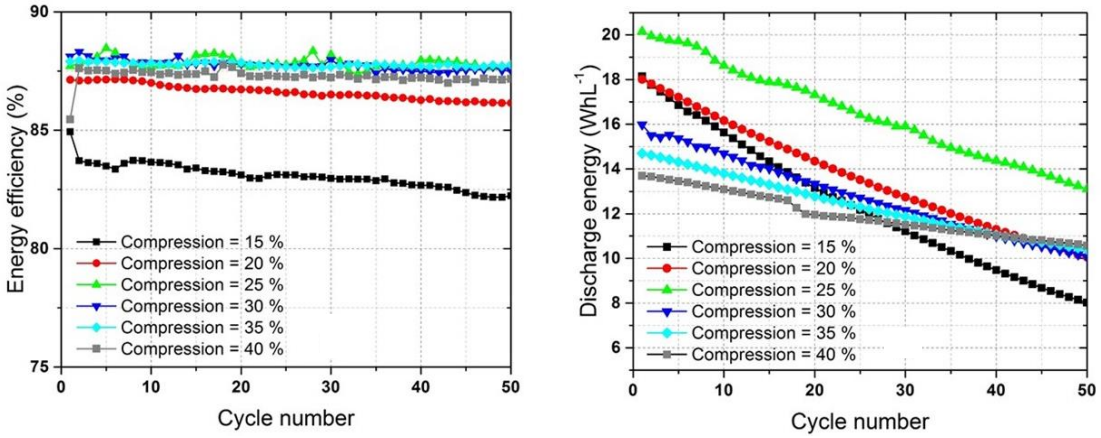

(a) **(b)**

Figure 5.6 (a) Energy efficiency and (b) discharge energy during 50 cycles at 40 mA cm^{-2}.

A nearly stable EE was observed at all compressions during long-term testing. The small decrease in EE is attributed to the well-known electrolyte imbalance, which evolves over time. The maximum EE is obtained with cells employing an electrode compression of

between 25% and 30%. By contrast, the highest drop in EE and capacity of 4% over 50 cycles are observed for the cell with an electrode compression value of 15%. Since the cells are operated at constant voltage cut-off mode, the discharge capacity (Ah) and discharge energy (Wh) show a very similar pattern. Interestingly, the decay rate of discharge energy (Wh) and discharge capacity (Ah) is a function of electrode compression. The discharge capacity decay over 50 cycles is shown in Table 5.4.

Table 5.4 Discharge capacity decay (%) for different electrode compressions over 50 cycles.

Compression (%)	**15**	**20**	**25**	**30**	**35**	**40**
Discharge capacity decay (%)	55	44	36	35	29	23

As shown in Figure 5.6b, an electrode compression of 25% exhibits the best initial DE and the highest retention over 50 cycles. This reflects the optimum trade-off between contact resistance and electrolyte utilization. The capacity fade (Figure 5.5d) is reversible since the capacity drop and the EE recover after rebalancing of the electrolyte. This indicates that the capacity fade is solely due to electrolyte crossover. As is evident from Table 5.4, the discharge capacity is reduced when the electrode compression is increased. This could be due to the presence of a larger number of dead zones on the electrode and membrane, which increases with electrode compression. This results in a lower electrolyte crossover through the reduced active membrane area. A similar trend has been also observed in a previous study [3].

The internal resistance (ρ) is a parameter that can be used to compare the different cell designs. Figure 5.7a summarizes the internal resistance at different current densities for cells assembled with different electrode compression levels. The internal resistance decreases up to a value of 25% and increases slightly with further compression. This behaviour points to a loss of elasticity of the felt, caused by over-compression. A similar trend is observed during long-term cycling at 40 mA cm^{-2}, as shown in Figure 5.7b. A small increment in internal resistance with cycling is due to a decrease in EE as an effect of electrolyte crossover.

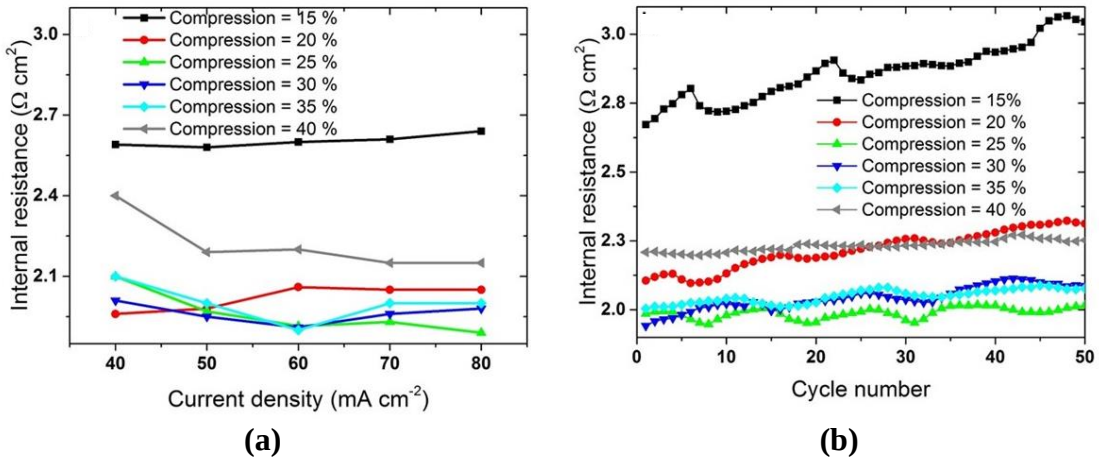

Figure 5.7 Internal resistance for various compressed electrodes (a) at different current densities and (b) at 40 mA cm^{-2} for 50 cycles.

The combined membrane and charge transfer resistances, as well as concentration change in a cell, can be estimated by subtracting the value of the dry cell resistance from the value of the wet cell resistance. The values obtained at 80 mA cm^{-2} for 15%, 20%, 25%, 20%, 35% and 40% of electrode compression are 1.54, 1.27, 1.14, 1.25, 1.39 and 1.56 Ohm cm^2, respectively. This indicates that cells with uniform flow distribution utilize the electrode and membrane area more effectively. This results in less of a difference between dry/wet resistances, as observed for the electrode compressed at 25% and 30%. The value for the membrane resistance alone is around 0.7 Ohm.cm^2, as stated in the corresponding data sheet of the manufacturer [4].

The value of the pressure drops ΔP for both the positive and the negative half-cell, for the first five cycles are compared in Fig 5.8a and 5.8b. Initially, the positive and negative electrolyte containers are filled with the electrolyte containing the same composition of vanadium species ($V^{+3.5}$). A sinusoidal oscillation in pressure drop in both the half-cells occurs during cell cycling because of the continuous change in the viscosity of the electrolyte. The viscosity is highest on the negative side during discharge and the lowest in a fully charged condition. In comparison to the negative half-cell, the change in ΔP on the positive half-cell is not significant, since the variation in viscosity during charging/discharging is low.

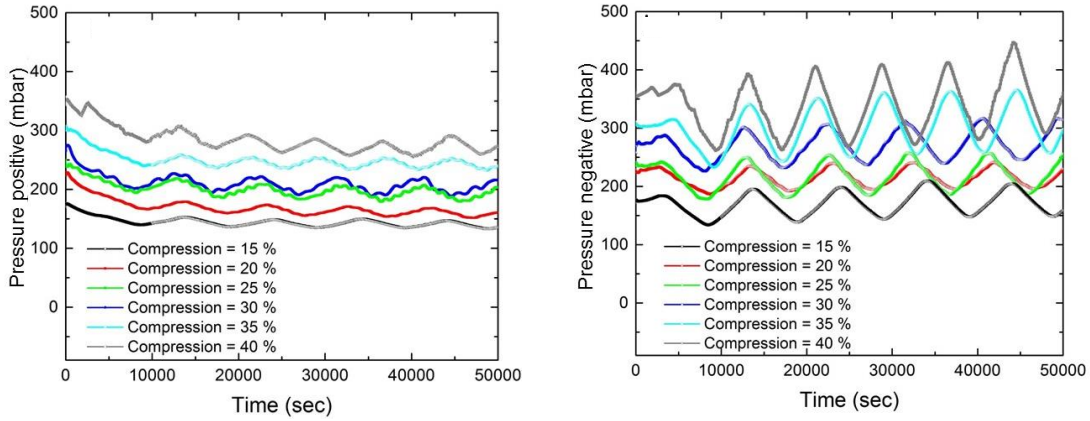

Figure 5.8 Pressure drop in (a) positive half- cell and (b) negative half-cell.

A significant increase in pressure drop (ΔP) is recorded when the electrode compression is increased. The increase in pressure drop increases the parasitic loss associated with pumping since the pumping energy is directly proportional to ΔP. During complete charging and discharging, the full change in ΔP in the negative half-cell is 187 mbar for a value of 40% electrode compression, whereas it is only 73 mbar for a value of 25% compression. Moreover, the difference in pressure between the two half-cells at 40% electrode compression is around 107 mbar, while it is reduced to 43 mbar at 25% of compression. Such reduced pressure difference between the two half-cells also lowers the convective drag. This results in a lower electrolyte crossover [5].

Assuming a pump efficiency of 0.7, the required pump power for a specific (volumetric) flow rate (Q) was estimated to

$$P_p = 2.\frac{\Delta P.Q}{0.7} \tag{5.3}$$

where P_p is the pump power (Watt) and ΔP is the pressure drop (Pa).

The power consumption was calculated for the two pumps. The pressure drop caused by bends, manifolds and pipes was deemed negligible as compared to the Δp across the porous electrode. For simplification and comparison purposes, an average pressure drop from the two half-cells was used as shown in. Figure 5.9.

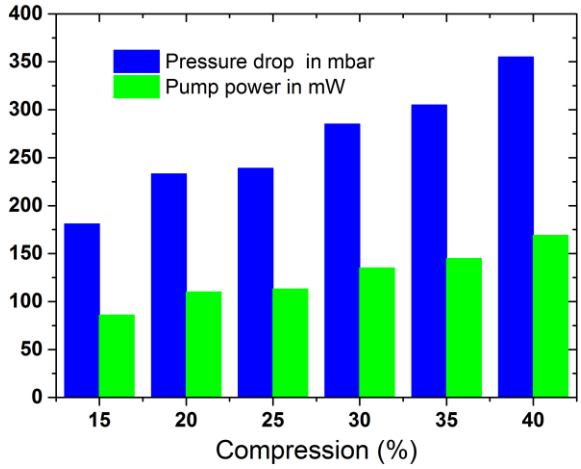

Figure 5.9 Pumping power consumption and pressure drop at different electrode compressions.

Figure 5.10 shows the overall EE with (a) and without taking into account pumping losses (b) for different compression levels.

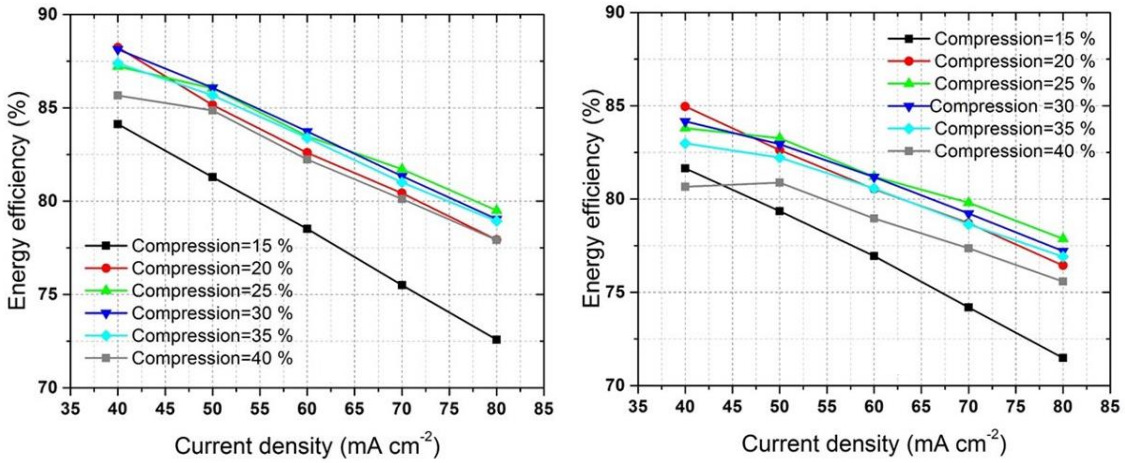

Figure 5.10 Energy efficiency (a: Net EE excluding pump power consumption and b: EE including pump power consumption) of VRFB cells at different current densities and compression levels.

Taking the total pump energy consumption into consideration (Figure 5.10b), the highest efficiency is achieved for an electrode having compression of 25%. For instance, comparing 25% compression against 15% compression, the maximum improvement in EE at 25% compression is 2.4% and 6.4% at 40 and 80 mA cm^{-2}, respectively. Similarly, comparing 25% compression against 40% compression, an improvement of 3.1% and 2.3%

in EE at 25% compression is obtained at 40 and 80 mA cm^{-2}, respectively. The effect of pumping losses on the EE at 25% compression, which is found to be optimal among all compression levels, is calculated to be 3.4% at 40 mA cm^{-2} and 1.6% at 80 mA cm^{-2}.

From the single cell results, it is clear that the electrode compressed at 25% (with respect to its original thickness) constitute the optimum level, ensuring the low contact resistance, moderate pressure drops, and highest efficiency. The spatially resolved study also shows the uniform flow distribution of electrolyte across the electrode at 25% electrode compression with the highest percentage of the reactant conversion. Thus, both segmented and non-segmented studies are in total agreement and also completely validates the proposed hypothesis of the electrolyte utilization as stated in Table 5.1.

5.1.4 Variation in the Operational Parameters to Observe the Change in Reactant Conversion

In previous subsections, we proposed and validated the use of local mapping of OCV and SOC to study flow behaviour in a flow cell and electrolyte utilization. The use of OCV contours instead of voltage contours under load allowed for a precise prediction of the flow streamlines through the porous electrode. In this study, we extended our approach to study the electrolyte utilization and flow distribution within VRFB cells using differently modified electrodes, flow rates, current densities and variable flow directions.

5.1.4.1 Effect of Electrode Modification

The porous electrodes used in VRFB are generally subjected to thermal or chemical pretreatment to improve the kinetics and wettability. We compared as-received, thermally modified (600°C for 5 hours in air) and chemically treated electrodes (immersion for 8 hours in mixed acid H_2SO_4: HNO_3 ratio 3:1) electrodes to observe the difference in flow distribution and electrode utilization. The OCV contours and corresponding SOC are depicted as shown in Figure 5.11.

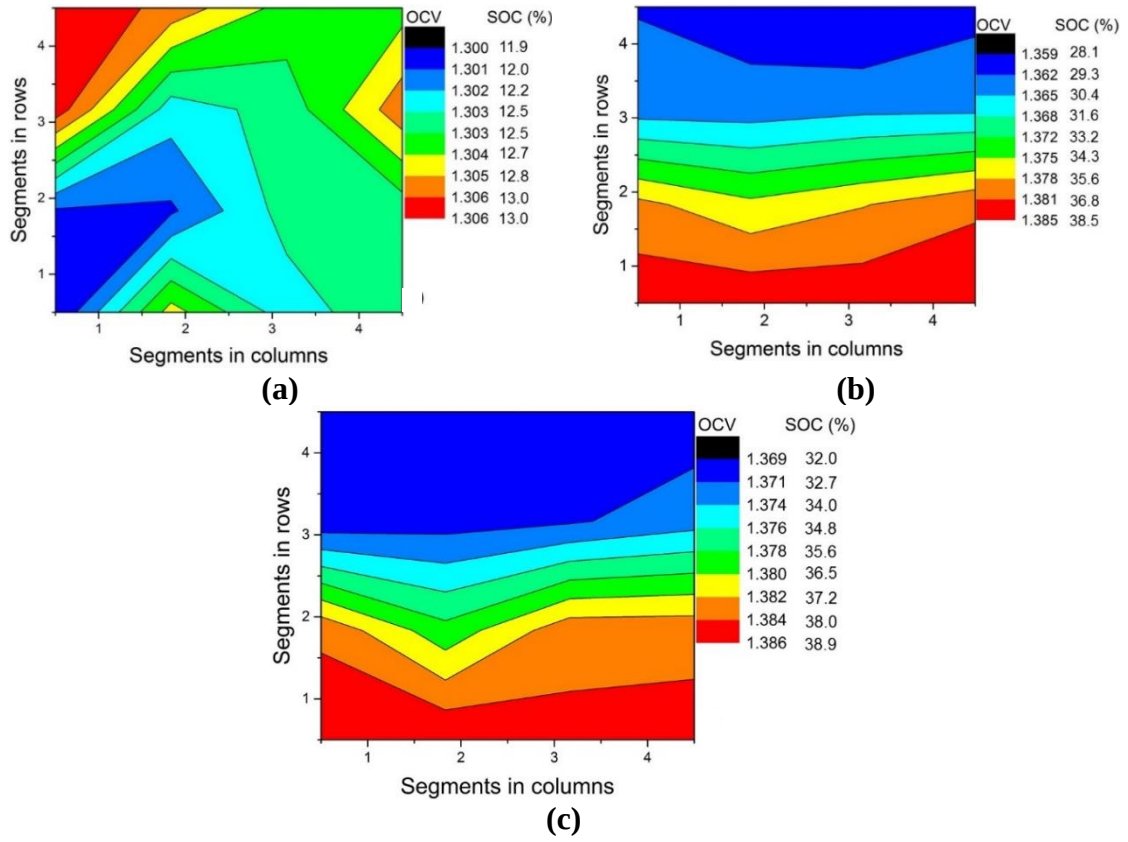

Figure 5.11 OCV contours at 5 s after termination of discharge at 80 mA cm^{-2} for (a) pristine, (b) chemically modified and (c) thermally modified electrodes. The flow of electrolyte was 42 mL min^{-1}.

A nearly flat band-type distribution of the OCV along the cross-section of the electrode is observed for the modified electrodes (Figure 5.11b and 5.11c). The distribution of the OCV/SOC contour, however, is random for the pristine electrode, as shown in Figure 5.11a. This is expected as wetting of the pristine electrode is poor and non-uniform and, hence, results in poor kinetics. The modified electrodes exhibit increased performance in comparison to pristine electrodes [6-8]. Their better wettability produces a uniform electrolyte distribution. Ideally, flat band-type voltage distribution along the cross-section is expected for highly homogeneous flow distribution. The small variations in voltage along the cross-section might be caused by minor variations in electrode compression in the large active cell area, non-uniform activation of the electrode and non-uniformity in felt thickness. Nevertheless, the variation along the cross-section is negligible and it can be concluded that the flow distribution improved substantially with the activation of the felt.

Monitoring the OCV at the inlet segments in each contour (Figure 3), it can be observed that the OCV reached its minimum (of 1.306 V) after terminating the discharge in the case of the pristine electrode. This again reflects the higher Ohmic drop for the cell assembled with the pristine electrode. Table 5.5 compares ΔSOC_{th} and ΔSOC_{exp}.

Table 5.5 Theoretical and experimental Δ SOC for the pristine and modified electrode

Electrode type		ΔSOC (42 mL min^{-1}, λ=3.4)
Theoretical		14.8%
Experimental	**Pristine**	33.8%
	Thermally treated	13.5%
	Chemically treated	15.2%

The minimal deviation between ΔSOC_{exp} and ΔSOC_{th} observed for the modified electrode indicates that the electrolyte conversion in a single pass occurs at a nearly optimum rate. This is obviously due to improved wettability, better kinetics and the larger active surface area. For pristine electrodes, retarded flow possibly occurred at different locations due to the hydrophobic nature of the electrode, which results in higher overpotential. Comparing these results with the three cases described in Table 1, the behaviour of pristine electrode matches with case (ii) (i.e. $\Delta SOC_{exp} >> \Delta SOC_{th}$), indicating poor utilization of electrolyte. By contrast, pre-treated electrodes show type (i) pattern having the highest electrolyte utilization.

5.1.4.2 Effect of Flow Rate

Limitations of mass transport are mainly dependent on flow rate and current density. Herein, ΔSOC_{exp} and ΔSOC_{th} are compared for different flow rates while keeping the current density constant at 80 mA cm^{-2}. Figure 5.12 shows the OCV contours at 5 s after the termination of discharge at 80 mA cm^{-2}. Three flow rates, 16 mL^{-1} min^{-1} (λ= 1.3), 32 mL min^{-1} (λ= 2.6) and 42 mL min^{-1}(λ= 3.4) have been used and evaluated for thermally activated electrode (600°C for 5 hours in air).

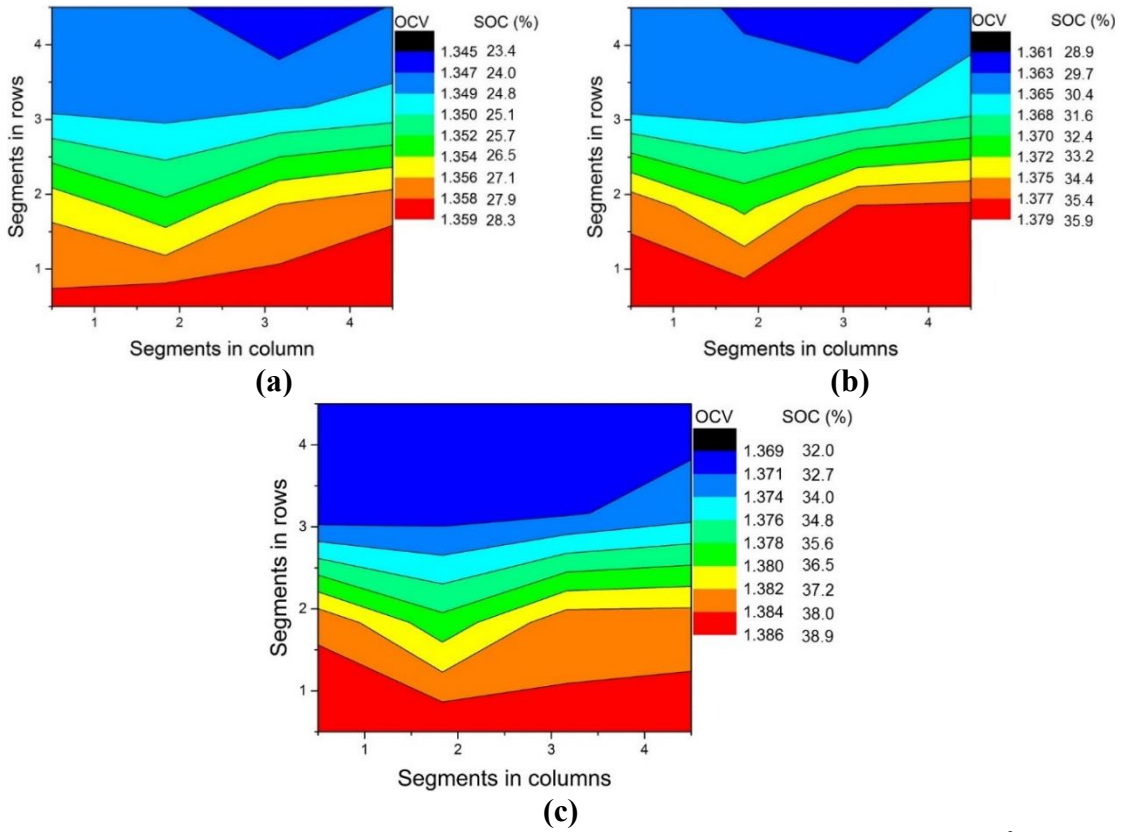

Figure 5.12 OCV/SOC contours at 5 s after termination of discharge at 80 mA cm^{-2}. The flow rate of electrolyte [was] (a) 16 mL min^{-1}, λ= 1.3 (b) 32 mL min^{-1}, λ= 2.6 and (c) 42 mL min^{-1}, λ= 3.4.

The OCV value at the inlet was minimum for the flow rate 16 mL min^{-1} (1.359 V) as compared to higher flow rates (1.379 V @ 32 mL min^{-1} and 1.386 V @ 42 mL min^{-1}) because the supply of charged species was low and thus even the inlet segments suffered from mass transport polarization. The discrepancy in OCV/SOC between the inlet segments and outlet segments increased with decreasing flow rate whereas the flow distribution along the cross-section of the electrode remained unaffected. A different picture was observed in terms of utilization.

Table 5.6 Theoretical and experimental ΔSOC conversion for the contour shown in Figure 5.11.

Flow rate	ΔSOC_{th}	ΔSOC_{exp}
16 mL min-1 (λ = 1.3)	38.8%	20.3%
32 mL min^{-1} (λ= 2.6)	19.4%	17.4%
42 mL min^{-1} (λ= 3.4)	14.8%	13.5%

Table 5.6 shows the deviation between ΔSOC_{exp} and ΔSOC_{th}. At a low flow rate of 16 mL min^{-1}, the ΔSOC_{exp} is significantly smaller than the ΔSOC_{th}. This follows the case (iii) in

Table 1 indicating that there is an insufficient amount of charged species to sustain the applied current.

This is obvious since the stoichiometry was only 1.3, where mass transport is expected to be dominant. The increase in flow rate results in a close agreement between the theoretical and experimental ΔSOC, which suggest that the stoichiometry of 2.6 (and above) is sufficient for the size of the cell under study. An excellent utilization is obtained at a flow rate of 32 and 42 mL min^{-1}.

5.1.4.3 Effect of Variation of the Current Density

Next, we varied the stoichiometry by applying different current densities while keeping the flow rate constant at 16 mL min^{-1}. The cell was discharged at three current densities of 150 mA cm^{-2} (λ= 0.7), 120 mA cm^{-2} (λ= 0.85) and 80 mA cm^{-2} (λ= 1.3), and respective OCV contours were examined, as shown in Figure 5.13. Again, a thermally activated electrode (600°C for 5 hours in the air) was used for these tests. The three contour diagrams revealed that there was no major change in flow uniformity when operating at different current densities. A similar observation was also made when the stoichiometry was varied by varying the flow rates.

Comparing the OCV values at the inlet in the three contour diagrams in Figure 5.13, it is observed that a higher OCV appears at the inlet at high stoichiometry (i.e. at low current density). At a current density of 150 mA cm^{-2} (Figure 5.13a), the cell suffers from high Ohmic and mass transport losses.

During discharge at 150 and 120 mA cm^{-2}, the stoichiometry is virtually less than 1. In other words, the charged species in the upstream segments are completely depleted, and therefore the set current can no longer be sustained within these areas. In such a situation, the current drawn from the upstream segments in row 2, 3 and 4 suddenly drops from the set current before the end of the discharge period (1 min). This is the reason that the ΔSOC_{th} is near twice the ΔSOC_{exp}.

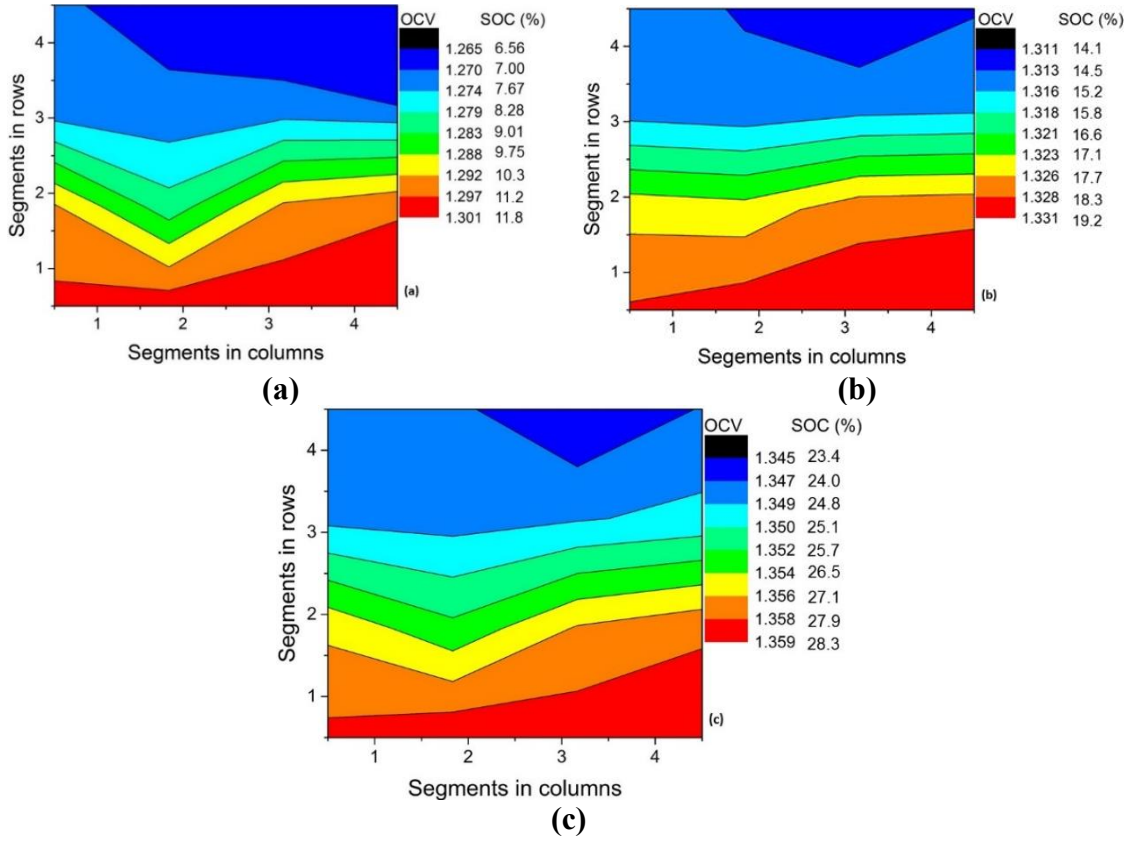

Figure 5.13 OCV/SOC contours at 5 s after termination of discharge at current densities of (a) 150 mA cm^{-2}, λ= 0.7 (b) 120 mA cm^{-2}, λ= 0.85 and (c) 80 mA cm^{-2}, λ= 1.3. The flow rate was kept constant at 16 mL min^{-1}.

At 80 mA cm^{-2}, the ΔSOC_{th} is still higher than ΔSOC_{exp}, which signifies that only insufficient quantities of charged species are available for continuous discharge at the set current. These three contours reflect case (iii) given in Table 5.7.

Table 5.7 ΔSOC_{exp} and ΔSOC_{th} for the contour diagram shown in Figure 5.12.

Current density	ΔSOC_{th}	ΔSOC_{exp}
150 mA cm^{-2}	72.8%	36.3%
120 mA cm^{-2}	58.2%	29.3%
80 mA cm^{-2}	38.8%	20.3%

5.1.4.4 Flow Configuration

Figure 5.14a and 5.14b compares the OCV/SOC distribution for normal and reverse flow, respectively. Clearly, the OCV bands appear almost mirror-inverted for both settings. This supports our claim that OCV or SOC contour closely mirrors the flow distribution across

the electrode.

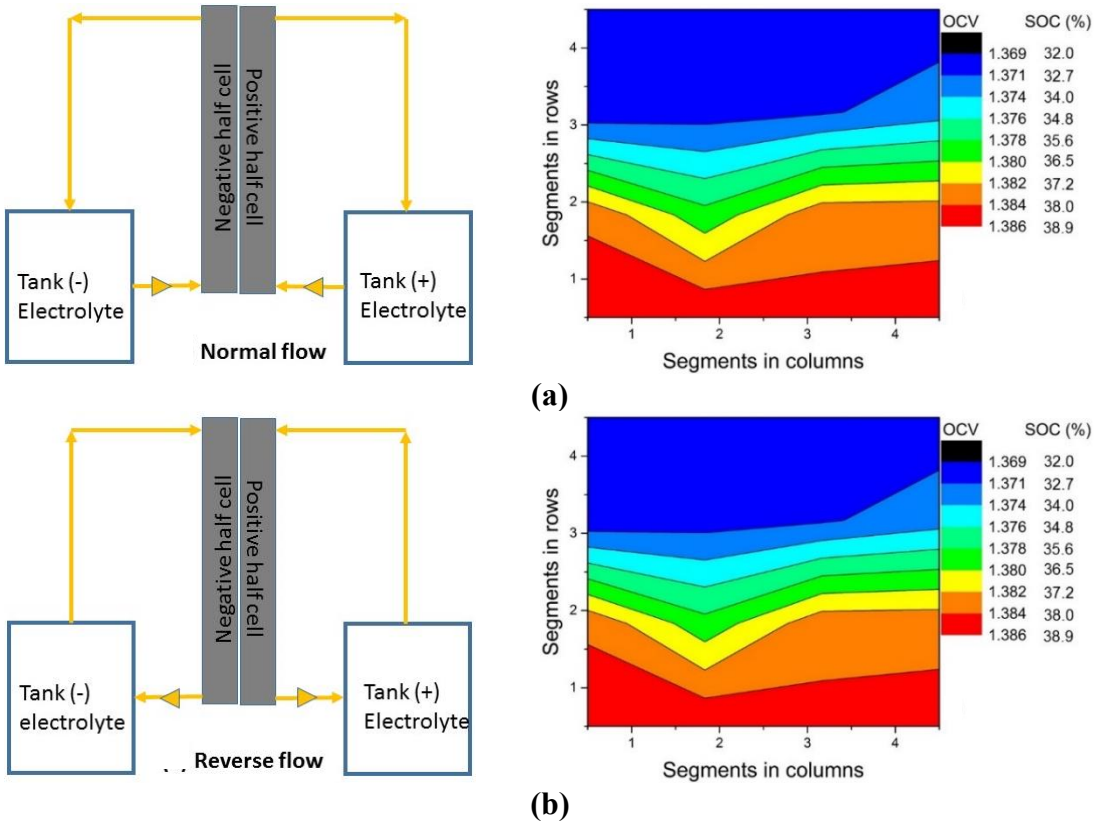

Figure 5.14 OCV contours at 5 s after termination of discharge at flow rate of 42 mL min^{-1} at current density of 80 mA cm^2 at (a) normal flow and (b) reverse flow.

As seen from the SOC contours for normal and reverse flow, the conversion efficiency is almost identical. This means that the flow direction does not have a perceptible influence on the electrode utilization. However, in a real application, upward flow is preferred to avoid any gas being trapped inside the voids during long charging and discharging cycles.

5.2 Investigation of In-situ Performance in Each Half of the Cell

This study presents a detailed study of an alternative method of inserting a reference electrode at the outlet tube for measuring individual half-cell potential. The description of the half-cell configuration for the measurement of potential in each half-cell is explained in subsection 2.6.2. However, to make easier to follow the next sections, it is worth to note two important points, namely: (i) the reference electrodes were inserted in the outlet tube

with the special holder and (ii) for investigation, the polarization study was undertaken (i.e. current density was varied).

5.2.1 Description and Validation of the Setup

The full cell voltage across two terminals was continuously recorded by the battery tester. At the same time, half-cell potentials across each terminal and reference electrode were continuously measured by the potentiostat. Theoretically, the following relations hold between the full cell voltage and half-cell potentials:

Full cell voltage – (Negative half-cell potential - Positive half-cell potential) = voltage drop across ion exchange membrane + iR loss due to the positioning of the reference electrode

For the estimation of the iR loss due to the positioning of the reference electrode, three reference electrodes were placed in the negative half-cell at the outlet at a distance of 8, 14 and 24 cm, respectively from the porous electrode (Figure 5.14a). The three terminals of the potentiostat were connected to the negative terminal of a battery and the respective reference electrodes. The difference in the potential with the change in the positioning of the reference electrode at different current densities measurement was estimated and depicted in Figure 5.15b.

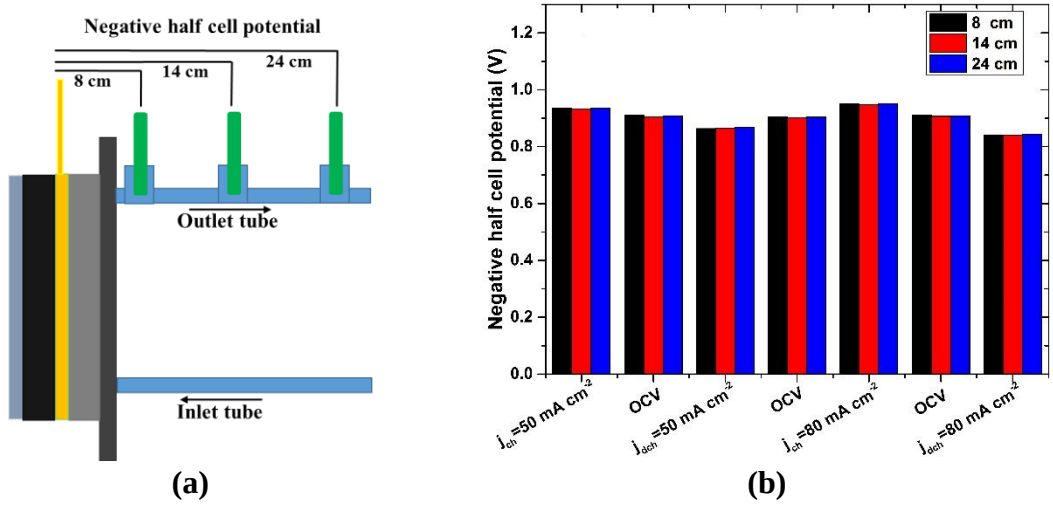

Figure 5.15 Schematic diagram of the placement of the reference electrodes to measure the negative half-cell potential at different lengths (a) and change in potential at various current densities (b).

Figure 5.15b confirms that the potential remains the same, irrespective of the reference electrodes placement. This clearly signifies that iR loss due to the positioning of the electrode is insignificant. Thus, the difference between the full cell voltage and half-cell potential is due to membrane resistance.

With the given experimental setup, it is possible to vary the different operating parameters while the cell is in operation. Therefore, this technique can be used for the optimization of the operating parameters.

5.2.2 Overpotential with a Change in Electrode Types

The electrochemical performance of the as-received and thermally treated graphite felts was tested with single-cell measurements by E-I curve, as shown in Figure 5.16.

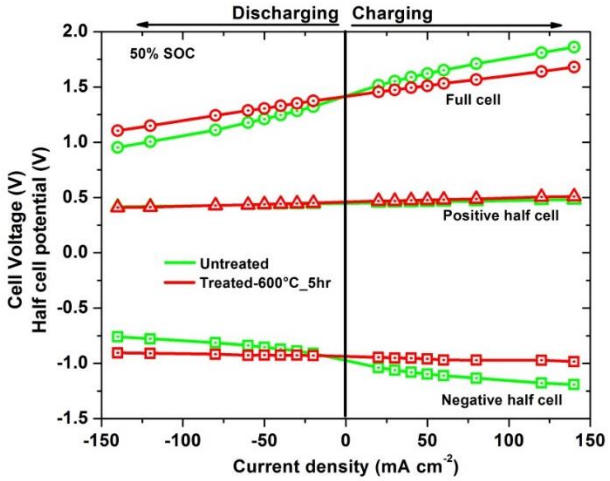

Figure 5.16 E-I curve for as-received and thermally treated graphite felt at 50% SOC and flow rate of 60 mL min^{-1}.

As observed in Figure 5.16, the overpotential in the negative half-cell reduces significantly after the use of thermally oxidized graphite felt. However, the positive half-cell does not show any change in potential with the type of electrodes used in the experiment. Thus, to obtain a clear overview of the change in overpotential with different electrode types, negative and positive half-cell potential is plotted separately as shown in Figure 5.17.

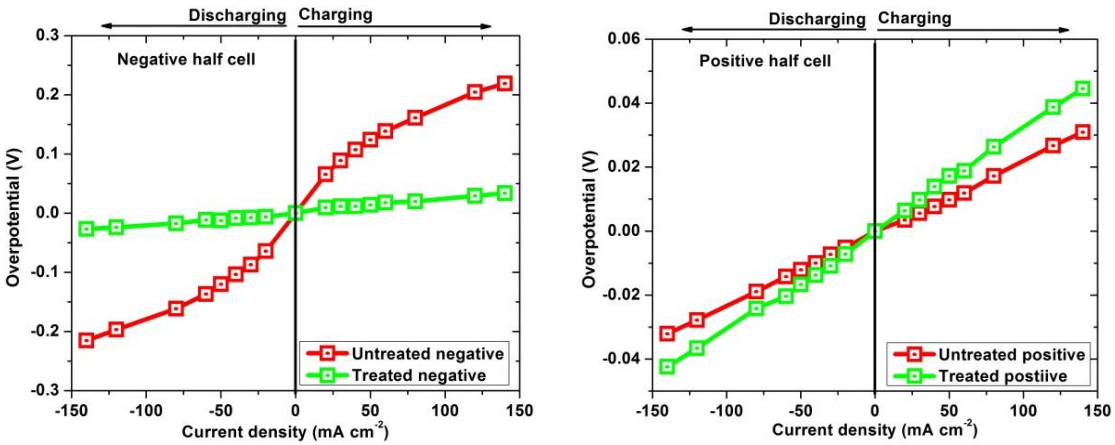

Figure 5.17 Negative half (a) and positive half (b) overpotential at 50% SOC of electrolyte and flow rate of 60 mL min^{-1}.

A maximum overpotential of 180 mV is reduced in the negative half-cell at 150 mA cm^{-2} due to the use of a thermally treated electrode. This improvement of negative half-cell performance is due to the physical and surface chemical properties improvement after the electrode modification. The thermal oxidation generates the oxygen-containing functional groups, increases the defects on the surface of the fibres and increases the wetted surface area. These changes in fibres catalyze the V^{2+}/V^{3+} redox reaction (i.e. increase in reaction rate constant, thereby resulting in small overpotential in negative half-cell after pre-treatment of the electrode. On the contrary, the use of the pre-treated electrode in the positive side results in a slight increase of overpotential (~ 14 mV). For VO^{2+}/VO_2^{+} redox reaction on the positive side, the increase in surface functional groups, such as hydroxyl, carbonyl, and carboxyl impede the reaction [9]. The thermal oxidation decreases the sp^2 carbon content and low sp^2 carbon content decreases the conductivity within the electrode [10]. However, the difference in overpotential with the use of pre-treated electrode is significant in negative half-cell only. Thus, it can be concluded that negative redox reaction is limiting reaction in VRFB.

5.2.3 Flow Rate of Electrolyte

To study the effect of flow rate in the potential of each half-cell, the experiment was performed from 10 mL min^{-1} to 50 mL min^{-1}. For all of the cases, the state of charge of the electrolyte was 50%.

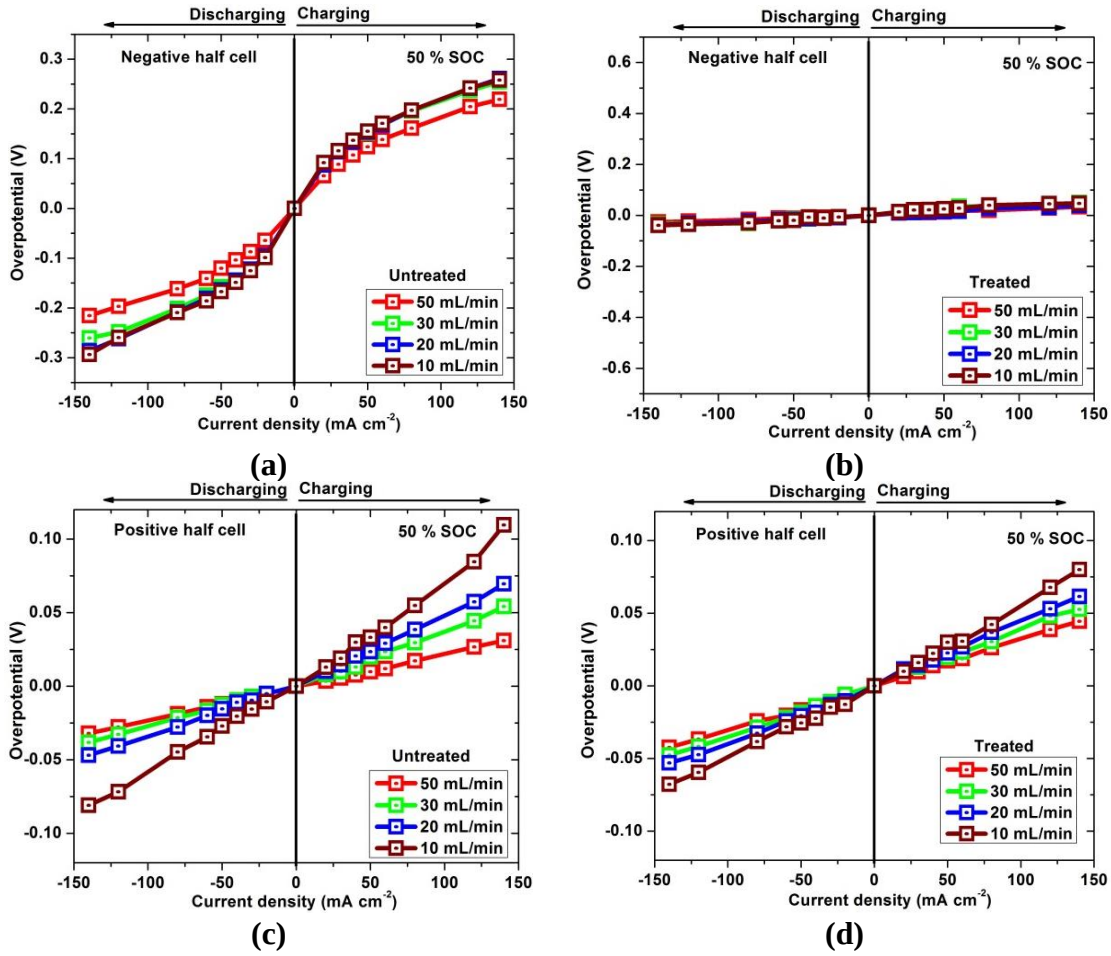

Figure 5.18 Change in overpotential due to the electrolyte flow rate (a) negative half overpotential for the untreated electrode, (b) positive half overpotential for the untreated electrode, (c) negative half overpotential for treated electrode and (d) positive half overpotential for the treated electrode.

From Figure 5.18a, it is observed that the overpotential of the cell increases as the flow rate is lowered in negative half-cell of the untreated electrode. This increase in overpotential is due to the contribution from the poor wettability of electrode and low flow rate (i.e. low stoichiometry). For untreated electrode, the change is stoichiometry is proportional to overpotential of the negative half-cell, as mass transport loss occurs despite being not dominant. After the thermal treatment of the electrode as shown in 5.18b, it is observed that the cell potential remains the same in negative half irrespective of the flow rate. This signifies that wettability is the crucial factor in negative half-cell, due to which electrolyte is uniformly distributed across even in low flow rate.

From the result of positive half-cell, as shown in Figure 5.17c and 5.17d, the cell potential remains almost similar irrespective of change in flow rate. This resembles with the result from the study of electrode type, which shows no improvement in positive half after the use of the thermally modified electrode.

5.2.4 Concentration of Electrolyte:

The polarization measurement was performed at the 1.6 mol L^{-1}, 0.8 mol L^{-1} and 0.4 mol L^{-1} concentration of vanadium electrolyte at 50% of SOC to observe the change in half-cell potential with vanadium concentration change.

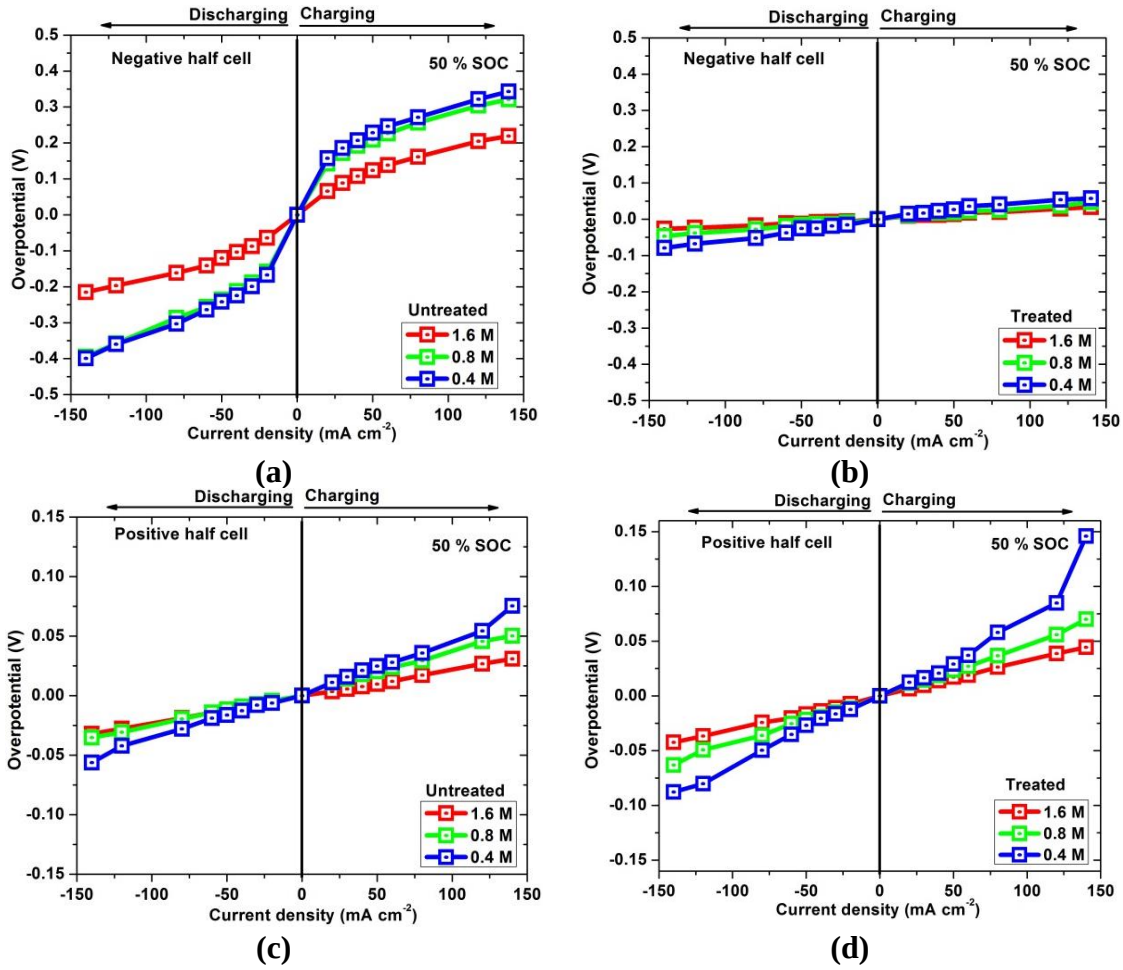

Figure 5.19 Change in overpotential due to the concentration of electrolyte (a) negative half overpotential for the untreated electrode, (b) positive half overpotential for the untreated electrode, (c) negative half overpotential for treated electrode and (d) positive half overpotential for the treated electrode.

The negative side of both untreated and treated electrode as shown in Figure 5.19a and 5.19b show the trend of an increase in overpotential with a decrease in the concentration of vanadium. This increase in overpotential is due to the change in stoichiometry. For example, calculation of stoichiometry is performed for untreated negative half-cell at a current density of 140 mA cm^{-2} at the flow rate of 50 mL min^{-1}.

Table 5.8 Variation of stoichiometry with the concentration of the electrolyte.

Concentration (mol L^{-1})	Stoichiometry (λ)
0.4	5.7
0.8	11.5
1.6	23

For untreated felt, the change in stoichiometry plays a dominant role. The electron transfer rate for the untreated electrode is low, thereby increasing the potential of the negative half-cell. Treated electrode exhibits the same behaviour as that of the untreated electrode, but the magnitude is low, which is due to the fast electron transfer in treated felt. Due to this, even in the less concentrated electrolyte (i.e. low stoichiometry), the change in cell potential is very less in the treated electrode compared to the untreated electrode.

5.3 Summary of the Chapter

The flow distribution, electrolyte utilization and overpotential in each half-cell of VRFB were studied using the two novel approaches namely, segmented cell study and reference electrode insertion method.

A segmented cell was developed to study the spatial voltage distribution and acquire information related to flow distribution and electrolyte utilization. With this view, a new approach of segmenting a flow cell with the segmentation of a BP and CC was demonstrated. The OCV of the sixteen segments were used for generating the voltage contours. The OCV distribution obtained directly after the cessation of the current replicated the status of the charged species in the electrode. The obtained counters were unaffected by the variation in contact and electronic resistance among the segments. The OCV distribution was used to predict the flow distribution of electrolyte across the electrode and can exactly image the pattern of the flow in the porous electrode. The obtained OCV values from each segment were converted to respective SOC of the

electrolyte. The relationship was established between the theoretical change in SOC obtained from Faraday's law and experimental change in SOC to predict the utilization of electrolyte across the porous electrode. A hypothesis was proposed based on the three different scenarios of the difference in theoretical and experimental change of SOC. For verification of the hypothesis, the compression of the electrode was varied at the different levels for both segmented and non-segmented cell. The results from both cells showed 25% as the optimized compression level of the electrode, thus validating the proposed hypothesis. The segmented study was further used to investigate the electrolyte distribution and utilization for differently treated electrodes, at various stoichiometry and different flow configurations.

A redox-flow experimental setup, into which two reference electrodes at the outlet pipe were inserted. This setup allows measuring the individual potential in each half-cell. With the aid of the polarization study, the overpotential in each half-cell was calculated. The polarization curves were used to record the overpotential for the differently activated electrode, at various flow rates and with different concentration of electrolytes. These measurements confirmed the negative side as the reaction rate-limiting half-cell and could calculate the performance gain due to the thermally oxidized electrode in the negative half-cell.

References

[1] A. Bhattarai, N. Wai, R. Schweiss, A. Whitehead, G.G. Scherer, P.C. Ghimire, T.D. Nguyen, H.H. Hng, *Journal of Power Sources*, **2017**, 360, 443-452.

[2] J.T. Clement, D.S. Aaron, M.M. Mench, *Journal of The Electrochemical Society*, **2016**, 163, A5220-A5228.

[3] S.-K. Park, J. Shim, J.H. Yang, C.-S. Jin, B.S. Lee, Y.-S. Lee, K.-H. Shin, J.-D. Jeon, *Electrochimica Acta*, **2014**, 116, 447-452.

[4] Redox-Flow-Batteries - Fumasep membrane types - Datasheet in, Fumatech GmbH, pp. 4.

[5] K. Knehr, E. Kumbur, *Electrochemistry Communications*, **2012**, 23, 76-79.

[6] A.M. Pezeshki, J.T. Clement, G.M. Veith, T.A. Zawodzinski, M.M. Mench, *Journal of Power Sources*, **2015**, 294, 333-338.

[7] K.J. Kim, Y.-J. Kim, J.-H. Kim, M.-S. Park, *Materials chemistry and physics*, **2011**, 131 547-553.

[8] B. Sun, M. Skyllas-Kazacos, *Electrochimica Acta*, **1992**, 37, 1253-1260.

[9] J. Friedl, C.M. Bauer, A. Rinaldi, U. Stimming, *Carbon*, **2013**, 63, 228-239.

[10] R. Schweiss, C. Meiser, F.W.T. Goh, *ChemElectroChem*, **2017**, 4, 1969-1974.

Chapter 6

Conclusions and Future Works

This chapter concludes the overall results obtained from the comprehensive studies discussed in chapters 5 and 6. It reflects the extent to which the targeted objectives are met as set at the inception of this thesis. This PhD research firstly evaluated the properties of the pristine and modified electrodes as part of investigation towards gaining a better understanding the relationship between thermal oxidation and/or metal doping treatment on a pristine electrode and its effect on the VRFB's negative half-cell redox reactions. Optimization of the thermal oxidation of electrode in negative half-cell and titanium carbide doping onto a negative electrode were also carried out to improve VRFB performance and stability. The other focus of this thesis was on the spatially resolved analysis of a redox flow cell. The local OCV distribution could predicate flow behaviour and electrolyte utilization across the electrode precisely. The electrode compression of 25% was found to be optimum based on both segmented and non-segmented cell studies. From the half-cell potential results, the modified electrode could clearly reduce the overpotential significantly in the negative half-cell of VRFB. The approaches developed in this research would help to improve the performance of the existing VRFB technology.

6.1 Conclusions

A series of experiments have been carried out to elucidate the aims and the conclusions extracted from this study are summarized below.

- **Synthesis of TiC catalyst on the carbon fibre to enhance the performance in negative half-cell of VRFB**

  A novel method for the preparation of TiC nanoparticles supported on graphite felts for use in VRFB has been and successfully demonstrated. The approach involved the hydrothermal conversion of a TiF_4 precursor adsorbed onto carbon fibre surfaces to TiO_2, followed by a carbothermal reduction of TiO_2 particles to TiC. Electrochemical tests of the materials as negative electrodes showed significant gains in the overall VRFB cell performance, which were attributed to the catalytic effects of TiC particles on the surface of the graphite felt. Energy efficiency and electrolyte utilization increased considerably as compared to a cell using pristine felt electrodes. The TiC-decorated electrode exhibited excellent stability and capacity retention over repetitive cycling. These findings suggest that this approach constitutes a viable concept for high-performance negative electrodes for VRFBs.

- **Systematic investigation and optimization of electrode oxidation duration and temperature**

  Thermal oxidation of graphite felts electrode alters the physical and electrochemical properties, thereby enhancing the performance of the negative half-cell of VRFBs. To gain a better understanding of the effect of thermal oxidation treatment, various temperature and time were selected based on the thermogravimetric curve of an electrode. Various physical and electrochemical characterization techniques along with cell cycling test were employed to identify the crucial electrode properties, such as surface chemistry, specific surface area, surface defects, wetting properties, etc. The outcomes of these characterizations revealed that the increase in thermally oxidized electrode wettability was mainly due to the considerable increase in oxygen-containing functional groups resulting from the thermal oxidation. Similarly, the oxidation also induced more defects (edge) in carbon surface resulting in an increase of sp^3-C content. Both oxygen

content and defects ratio followed the same trend as that of mass loss. Higher defect density was related to the higher surface area as revealed by BET measurement and double layer capacitance. From electrochemical characterization (CV and EIS), the electron transfer rate is higher in samples T550-5h, T600-5h and T750-5m, respectively. The cell cycling test results were in close agreement with the results from the surface and electrochemical characterization. Overall, the findings showed that the enhanced electrode performance by thermal oxidation might not be due to singular property but rather were attributed to a combination of different material parameters. Out of various samples examined, the sample treated at 750°C for 5 minutes i.e. the conditions that have never been reported to date showed the most favourable effect. The most practical outcome of this study is the understanding that short treatment intervals at harsh oxidation conditions constitute a viable option to reproducibly produce well-performing materials in a very cost-effective manner.

- **Material properties and reproducibility**

  From the study of the material obtained from different manufacturing batches, it can be concluded that the samples under investigation exhibited similar physical, electrochemical and cell performance results. The electrodes exhibited similar surface morphology with the same bulk properties. Similarly, the number of defects ratio, content and type of oxygen-containing functional groups was also found almost similar for all of the electrodes investigated. The electrochemistry of the single electrode showed similar charge transfer resistance and electrochemical activity with similar DLC and HER onset potential values. Finally, the results from cell cycling are also in good agreement with the physical and electrochemical results.

  This study indicates that the manufacturing process is highly reproducible and hence there should not have any changes in physical and electrochemical properties among the batches.

- **Locally resolved electrolyte distribution and utilization study with the aid of segmented cell**

  An approach of segmentation was introduced for local voltage mapping. The use of OCV contours instead of voltage contours under current flow allowed for a

precise prediction of the flow streamlines through the porous electrode. A new strategy for mapping and quantification of the conversion efficiency (or reactant utilization) in redox flow batteries using segmented cells was presented. The OCV contours immediately after cessation of the discharge current were used for visualization and quantification of flow distribution and reactant conversion across the electrodes at different operating parameters included a modified electrode, flow rate/direction and current density. A rationale based on the deviation of (experimentally determined) local reactant conversion and the theoretical change in SOC (assuming full conversion of redox species) was developed. It allows for simple discrimination of different operational states, such as poor reactant utilization, reactant depletion or optimum conversion. This approach could, therefore, be very valuable in practice to optimize flow battery performance with commercial size cells.

- **Optimization of electrode compression employing both segmented and non-segmented cells**

  A systematic study of the effects of electrode compression on all relevant performance parameters of VRFB has been carried out. The compression of the graphite-felt electrodes was varied between 15% and 40% in VRFB cells having an active area of 100 cm^2. In addition to conventional figures of merit, such as efficiencies and resistances, the effects of compression on pressure drop and flow distribution were investigated. The latter was visualized by means of locally resolved measurements using the segmented cell approach. All the experiments exhibited that the utilized carbon felt electrodes compressed at 25% (with respect to the original thickness) gave the optimum level, ensuring low contact resistances, moderate pressure drops, homogeneous flow distribution across the porous electrode and maximum electrolyte utilization.

- **In-situ performance investigation of each half-cell**

  An experimental setup was developed by inserting the reference electrode at the outlet tube of VRFB to independently study both half-cells. The result for the performance measurement indicated that the thermal modification of graphite felt resulted in a reduction of overpotential only on the negative side of the cell. The

positive half-cell remained completely unaffected by the electrode thermal modification. Thus, it was concluded that the negative redox reaction was the rate determining reaction in VRFB. By using the same setup, the stoichiometry of electrolyte was varied for both treated and untreated electrodes. For untreated electrode, the change in flow was proportional to overpotential of the negative half-cell, as mass transport loss occurred despite not being dominant. For thermally treated electrodes, the cell potential remained the same in negative half even at a very low flow rate. For positive half-cell, the increase in overpotential remained almost similar for both types of electrodes.

6.2 Future Works

In this project, electrode properties, its reproducibility, modification/activation method to enhance the performance and the optimization of the activation method were investigated. In addition, a diagnostic tool was developed to investigate the real-time behaviour of the cell at different operating conditions. Based on these findings, there are some remaining challenges that warrant further researcher in future.

- This project was mainly focused on the material properties and the ways to enhance and optimize it without investigating the degradation of the electrode and the corresponding long-term chemical stability. The degradation of the electrode depends upon the cycling conditions. A constant cut-off voltage of 1.65 V was used throughout the study, thus the cut-off voltages should be extended to acquire information about the effect of upper cut-off voltage on electrode properties at both the negative and positive half-cells. Further, the effect of chemical ageing of the electrode with respect to the initial condition should also be investigated as it will help to prevent and/or minimize electrochemical degradation of electrodes by fixing the appropriate cut-off voltage and initial operating parameter conditions.
- Accelerated degradation testing and post-mortem study could be performed in order to obtain information about the electrodes in each half-cell. Since long term cycling test may take months, degradation by stress testing may be the appropriate method. For example, applying the potential stress in electrode using the three-electrode setup i.e. applying constant higher potential on the electrode can be carried for a

few hours. Alternatively, operating the cell at higher SOC for a longer duration can be performed to observe deviation from the initial results. Similarly, operating cell at lower stoichiometry will also aid in knowing the criticality of flow rate and current density on the properties of the electrode.

- The negative half-cell electrode was modified with TiC particle to enhance the VRFB performance. The result revealed excellent stability and capacity retention. Therefore, the study can be extended for the larger active area and should include long-term stability (several hundred cycles). The investigation of the electrode properties after several hundred cycles with respect to a non-decorated electrode can provide information about the difference in chemical ageing and distinguish the effect of the modification.
- The segmented cell study was found to be suitable to quantify flow distribution and predict electrolyte utilization during battery operation. The study was conducted only on 100 cm^2 cell due to the limitation of the time, however, this study can be easily extended to large size cell to optimize the cell operating parameters, such as flow rate, electrode modification, degradation etc. The study can be implemented in a commercial size stack to enable optimal battery operation strategies and cells designs.